entropy

MDPI

Article

Geosystemics View of Earthquakes

Angelo De Santis [1,2,*], Cristoforo Abbattista [3], Lucilla Alfonsi [1], Leonardo Amoruso [3], Saioa A. Campuzano [1], Marianna Carbone [3], Claudio Cesaroni [1], Gianfranco Cianchini [1], Giorgiana De Franceschi [1], Anna De Santis [1], Rita Di Giovambattista [1], Dedalo Marchetti [1], Luca Martino [2], Loredana Perrone [1], Alessandro Piscini [1], Mario Luigi Rainone [2], Maurizio Soldani [1], Luca Spogli [1,4] and Francesca Santoro [3,*]

1 Istituto Nazionale di Geofisica e Vulcanologia – Sez. Roma 2, 00143 Rome, Italy; lucilla.alfonsi@ingv.it (L.A.); saioa.arquerocampuzano@ingv.it (S.A.C.); claudio.cesaroni@ingv.it (C.C.); gianfranco.cianchini@ingv.it (G.C.); giorgiana.defranceschi@ingv.it (G.D.F.); anna.desantis@ingv.it (A.D.S.); rita.digiovambattista@ingv.it (R.D.G.); dedalo.marchetti@ingv.it (D.M.); loredana.perrone@ingv.it (L.P.); alessandro.piscini@ingv.it (A.P.); maurizio.soldani@ingv.it (M.S.); luca.spogli@ingv.it (L.S.)

2 INGEO Department, Università G. D'Annunzio, 66100 Chieti, Italy; martinoluca@hotmail.it (L.M.); rainone@unich.it (M.L.R.)

3 Planetek Italia srl, via Massaua 12, 70132 Bari, Italy; abbattista@planetek.it (C.A.); amoruso@planetek.it (L.A.); carbone@planetek.it (M.C)

4 SpaceEarth Technology, 00143 Rome, Italy

* Correspondence: angelo.desantis@ingv.it (A.D.S.); santoro@planetek.it (F.S.)

Received: 20 March 2019; Accepted: 12 April 2019; Published: 18 April 2019

check for updates

Abstract: Earthquakes are the most energetic phenomena in the lithosphere: their study and comprehension are greatly worth doing because of the obvious importance for society. Geosystemics intends to study the Earth system as a whole, looking at the possible couplings among the different geo-layers, i.e., from the earth's interior to the above atmosphere. It uses specific universal tools to integrate different methods that can be applied to multi-parameter data, often taken on different platforms (e.g., ground, marine or satellite observations). Its main objective is to understand the particular phenomenon of interest from a holistic point of view. Central is the use of entropy, together with other physical quantities that will be introduced case by case. In this paper, we will deal with earthquakes, as final part of a long-term chain of processes involving, not only the interaction between different components of the Earth's interior but also the coupling of the solid earth with the above neutral or ionized atmosphere, and finally culminating with the main rupture along the fault of concern. Particular emphasis will be given to some Italian seismic sequences.

Keywords: earthquakes; entropy; criticality; seismic precursors; Benioff strain; accelerated moment release

1. Introduction

Society advancement usually moves toward progress and modernization. However, the latter does not bring only positive things but they may also involve some vulnerability against natural hazards, much higher than in the past (e.g., [1]). Hurricanes, earthquakes (EQs), floods, tsunamis, and other kinds of catastrophes, are often out of human control and the consequences are unpredictable. They happen as extreme events on the planet causing destruction and deaths [2], and the occurrence of most of them looks as increasing dramatically in the last century [3]. Unfortunately, no strong remedy and rapid resilience are yet fully possible [4].

Among the possible solutions, one is to study and then understand how our planet works and what possible future sceneries are. To do this, we cannot limit our approach to a reductionist one, but we also need to study the Earth as a whole system, where all parts are nonlinearly interconnected and functional for the system to its evolution (e.g., [5]). The reductionist approach looks at Earth as a precise clock system where all components have their distinct own purpose (often called as the Laplacian point of view). With geosystemics [6,7], we can consider the planet as an ensemble of cross-interacting parts put together in order to reach the same ambitious goal that, at the present knowledge, seems to be rare in the Universe: to maintain life [8]. Earth system is both composed of living organisms and soft and hard engines, in a continuous balance and competition between life and death, heat and cold, complexity and simplicity, chaos and non-chaos.

In this paper, we will remind the concepts of geosystemics and then apply them to EQs, through, among others, the Benioff strain, Entropy, temperature, etc., in the frame of a Lithosphere-Atmosphere-Ionosphere (LAI) coupling model, i.e., some quantities that are related to macroscopic features of the system under study.

Although many efforts have been made towards a deeper knowledge of EQs, in terms of experimental, theoretical and numerical models (e.g., [9–11]), the evolution phases of an earthquake are not exhaustively explained yet. A possible explanation of this uncertainty is the lack of knowledge regarding the source initiation, the fracture mechanisms and dynamics of the crust (e.g., [12]). Moreover, each EQ initiates and develops in its proper geodynamical and lithological settings, thus giving an almost unique character to each event. Thus, to reach the knowledge necessary to recognize in advance the eventual rupture (failure) of the fault, which causes the occurrence of the EQ, is a greatly difficult task itself. Difficult as well, it is the possible explanation of the various and often weak phenomena affecting the above atmosphere and ionosphere, where even many external causes act to mix together signals, which are different in spectral content and amplitudes.

Despite all these difficulties, the eminent seismologist, [13], pointed out that some common physical mechanisms beneath the generation processes may act, although controlled by the local geodynamic forces and heterogeneities of the lithology [14]: this thought encourages the efforts towards a deeper knowledge of the physics behind such a complex phenomenon as the EQ.

If the process of rupture that causes the EQ is still plenty of open issues and unanswered questions (e.g., [15]), even more difficult is the understanding of the process of EQ preparation, although some efforts have been performed (e.g., [16–18]). It is thought that it may be accompanied by some exchanges of mass and energy, which can change the energy budget in the earth-atmosphere system over the seismogenic zone. In fact, scientific literature reports a wide variety of phenomena preceding EQs which have been studied extensively with the aim of finding some recurrent and recognizable patterns: induced electric and magnetic fields, groundwater level changes, gas and infrared (IR) electromagnetic emissions, local temperature changes, surface deformations, ionospheric instabilities (see [19,20] for more exhaustive reviews).

With geosystemics introduced by the first author of this work, a great part of the paper is based on own contributions from mostly already published material. However, we attempted to give new insights on the idea of geosystemics, with also some unpublished own material or other researchers' contributions.

At first, we place the present view of geosystemics and show the application to some case studies. We then describe a possible physical model that attempts to explain the found results. We finally conclude with some feasible future directions and conclusions.

2. Geosystemics

Geosystemics looks at the Earth system in its whole focusing on self-regulation phenomena and interrelations among the parts composing our planet, possibly searching for the trends of change or persistence of the specific system or sub-system under study [6,7,21]. To this objective, geosystemics applies mainly the concepts of entropy and information content to the time series that characterize the phenomenon under study: as said by [22], to measure and understand the physical world, not only energy and matter are important, but also information. Interesting features of the complex system of interest to investigate are nonlinear coupling and new emergent behavior, self-regulation, and irreversibility as important constituents of the Earth planet. Entropy and information are very representative of the state and the possible evolution of the system under study [6].

No layer of the Earth system is really isolated, rather it interacts, in terms of transfer of energy or particles, with the other ones. This concept is more strengthened in the case of very powerful phenomena that release large energy in a short time, such as the earthquakes in the lithosphere (for an M7 earthquake, around 10^{15} Joule is released in some seconds), lightning strikes in the atmosphere (around 10^9 J in microseconds), etcetera. For instance, the information exchanged between contiguous parts of the Earth system producing increased entropy would allow us to better recognize and understand those irreversible processes occurring in the Earth's interior. As said by [21], "geosystemics has the objective to observe, study, represent and interpret those aspects of geophysics that determine the structural characteristics and dynamics of our planet and the complex interactions of the elements that compose it" by means of some entropic measures.

Together with this, the approach will be based on multi-scale/parameter/platform observations in order to better scrutinize the particular sub-systems of Earth under study as much as possible. This is a fundamental issue of geosystemics because there is no better way to understand the behavior of a complex system than looking at it from as many perspectives and points of view as possible. Recent advanced examples to observe the planet are from satellites (e.g., [23]) and seafloors [24].

Geosystemics differs from the standard Earth System Science (e.g., [5,25–27]): for instance, in the way it is applied by means of entropic measures to different physical quantities, this because entropy is the only entity that can be used to have some clues on the next future. Please remind the second law of thermodynamics for which the entropy cannot decrease with time (e.g., [28]). This is related to the fact that a change of dynamical state requires some transfer of energy and some involved dispersal of it, mostly in terms of heat. The great advantage of this approach is that "the emergent dynamics may be extremely complex in detail, but the overall behavior of the system becomes simple as it is dominated by the overall constraints imposed by the thermodynamics of the system" [29] (p. 11).

In this paper, we will concentrate the attention to the application to EQ physics study and the possibility for intermediate and/or short-term prediction. Here, with the term "prediction", we mean the possibility to make a prediction about EQ occurrence, magnitude and location, with small uncertainty, i.e., in a deterministic way, in contrast with the probabilistic approach used in EQ forecast (please see also in the next section for other details on this question). In particular, we will explore the present state-of-the-art of the seismological diagnostic tools based on a macroscopic point of view. As an EQ is the manifestation of a dramatic change of state of the lithosphere, geosystemics and entropy are powerful tools to study this kind of energetic phenomenon. Particular emphasis will be dedicated to the Shannon entropy [30]. Later on, we also see another one that quantifies the sense of the flow of information, the transfer entropy [31].

3. Main Seismological Diagnostic Tools

The Holy Grail in seismology is to reach the capability of giving a short-term prediction of large EQs thus eventually saving lives. Unfortunately, it is not an easy task as testified by the great all-out and full-scale effort made with this aim in many fields of research (even far from the traditional field of seismology) and the corresponding huge amount of scientific papers claiming or denying success or simply attempting some important steps forward towards the goal. However, despite many attempts, no significant success has been clearly counted [32].

Regarding the methods to make EQ "predictions", we can classify them in (mainly) deterministic and (mainly) stochastic methods. The bracketed term "mainly" is placed because, actually, no method is only deterministic or stochastic. To be operative, we can define the latter methods as those that provide a forecast with some level of probability, for which the probability of no EQ is always different than zero, while the deterministic methods attempt to indicate the approaching of a large EQ with some level of confidence, i.e., with small uncertainty in space and time of occurrence, and magnitude.

Several statistical methods have been applied in the last decades to seismological data (mainly catalogs) with the aim of improving the knowledge on seismic phenomena. At present, the scientific community is involved in global projects to test and evaluate the performances of some well-established algorithms in different tectonic environments (see [33,34]). According to CSEP (collaboratory for the study of earthquake predictability), the most important steps of an earthquake prediction protocol are the following ones:

1 Present a physical model that can explain the proposed precursor anomaly.
2 Exactly define the anomaly and describe how it can be observed.
3 Explain how precursory information can be translated into a forecast and specify such a forecast in terms of probabilities for given space/time/magnitude windows.
4 Perform a test over some time that allows us to evaluate the proposed precursor and its forecasting power.
5 Report on successful prediction, missed earthquakes, and false predictions.

All these points are sequential, i.e., any mature precursor must sequentially satisfy them. However, if a precursor is at an initial stage of maturity, for instance, it has been just discovered in some case studies, it can satisfy only some of the first points, lacking the following ones. An early stage of the work on some novel precursors cannot exclude the publication of initial investigations. This is the case of most recent found precursors (e.g., entropy) that we will show below.

In the present paper, we surely meet the first two points, leaving the other three points to other papers where a deeper and extended study is performed on a few but different precursors (e.g., [35,36]). We will mention something more about those works in a subsequent section.

In this part, we will focus our attention on the deterministic methods, which are essentially grounded on a systematic catalog-based recognition of some peculiar seismicity patterns in the given area of interest. A wide review of this topic is presented by [37]. In the following, we will describe *M8*, *RTP* (reverse tracing of precursors), *PI* (pattern informatics) and *R-AMR* (revised accelerating moment release). The latter method is the most recent and is the one we know much better because some of the present co-authors have introduced the corresponding technique [38]. For this reason, we will dedicate a specific section to it.

3.1. M8

*M*8 owes its name to the fact that it was designed as a retroactive analysis of the seismicity preceding the greatest (M8+) EQs worldwide (e.g., [39,40]). Some spatio-temporal functions are introduced in order to describe the seismic flow in a target area (wider than the earthquake source). The M8 takes into account only mainshocks, which are described by a 6-component vector, i.e., time (t), latitude, longitude, depth(h), magnitude (M), and the function B(*e*) that corresponds to the number of aftershocks that occurred after the first *e* days after the mainshock. The function N(t) is the intensity of the earthquake flow and it represents the current state of seismic activity. L(t) is the deviation of N(t) from the long term trend. As the earthquake occurrence rate depends on the zone, the method normalizes the magnitude of the event and the earthquake flow becomes constant, usually 10/year and 20/year, so it takes into account 6 years of the time interval. The algorithm then recognizes a well-established criterion, defined by extreme values of the phase space coordinates, as a vicinity of the system singularity. When a trajectory enters the criterion, the probability of an extreme event increases to the level sufficient for its effective provision, so an alarm or a TIP, "time of increased probability", is declared. This algorithm can be modified for lower magnitudes and particular regions (e.g., CN8).

3.2. The Reverse Tracing of Precursors (RTP)

The RTP is a method for medium-term (some months in advance) EQ prediction [41], which is based on a hierarchical ensemble of premonitory seismicity patterns. These patterns are: (1) "precursory chains" that are related to the correlation length (e.g., [42,43]), (2) "intermediate-term patterns" that could be related to some accelerating seismicity (e.g., [44]) and (3) "pattern recognition of infrequent events" that take into account several "opinions" to decide the validity of the calculated chain of events. If a sufficient number of "votes" is accumulated, then the chain is considered precursory [41]. Some past EQs seem to have been predicted 6 to 7 months in advance, although few false alarms also happened. Critical aspects are related to the predicted "area of alarm" that seems very large for a realistic application. RTP has already evaluated by the gambling score, showing apparently only marginal or no significance in predicting earthquakes [45]. However, [46] criticized this conclusion, affirming that: "The statistical analysis of any prediction method with few target events and a short monitoring period is premature (this is the case of RTP)".

3.3. Pattern Informatics (PI)

The *PI* is a technique for quantifying the spatio-temporal seismicity rate changes in past seismicity (e.g., [47,48]). In [49] the authors derive a relationship between the "PI index" and stress change (e.g., [50]), based upon the crack propagation theory. In practice, the PI method measures the change in seismicity rate at each box of a pre-defined grid, relative to the background seismicity rate, through the division of the average rate by the spatial variance over all boxes. Then it identifies the characteristic patterns associated with the shifting of small EQs from one location to another through time prior to the occurrence of large EQs [49]. Results are given in terms of mapping the "PI anomalies" which are located where a new large EQ can be expected. [51] proposed a modification of PI by using complex eigenfactors, explaining the EQ stress field as obeying a wave-like equation.

4. Shannon Entropy and Shannon Information

The Shannon Entropy h(t) [30] is an important tool for the space-time characterization of a dynamical system. In general, for a system characterized by K possible independent states, this entropy is defined in a certain time t as follows:

$$h(t) = -\sum_{i=1}^{K} p_i(t) \cdot \log p_i(t) \tag{1}$$

where $p_i(t)$ is the probability of the system to be at the i-th state. For convenience, we impose $\sum_i p_i = 1$ and $\log p_i = 0$ if $p_i = 0$ to remove the corresponding singularity. Although the base of the logarithm could be any, we will use later on the decimal one for the logarithm.

In literature, we can find a large number of physical interpretations of the Shannon entropy. We consider here what we think it is the simplest one: it is a non-negative measure of our ignorance about the state of the system of concern. The Shannon entropy has great importance in evaluating and interpreting the behavior of complex systems like the Earth, in general, and EQs, in particular. On the other hand, we find in literature also the Shannon Information, $I(t)$, which is simply related to $h(t)$ by the simple relation $I(t) = -h(t)$. Consequently, the Shannon information is a negative quantity that measures our knowledge on the state of the system when we know only the distribution of probability $p(t)$ [52]. Thus, this quantity measures our decreasing ability to predict the future evolution of the system under study.

5. Gutenberg-Richter Law and *b*-Value

The Gutenberg-Richter (GR) law has a central role in seismology [53]. It expresses the logarithm of the cumulative number n of EQs with magnitude m equal to or larger than a magnitude M:

$$\log_{10} n(m \geq M) = a - b \cdot M \tag{2}$$

as a simple linear function of the magnitude M; a and b are two constant parameters for a certain region and time interval, characterizing the associated seismicity; in particular, b is the negative slope of the above cumulative distribution and typically $b \approx 1$. Very soon it was recognized the importance of estimating the b-value as an indicator of the level of stress in a rock from laboratory experiments [54], and only later the relationship was confirmed for EQs [55].

Ref. [56] was the first to provide a simple expression to estimate b by means of the maximum likelihood criterion (with a correction proposed by [57]:

$$b = \frac{\log e}{\overline{M} - M_{min} + \cdot/2} \tag{3}$$

whose uncertainty is: $\pm b/\sqrt{N}$.

N is the total number of analyzed EQs; e = 2,71828 ... is the Euler number, while $\overline{M}$ is the mean value of the magnitudes of all considered EQs; M_{min} is the minimum magnitude used in the b-value evaluation; Δ is the resolution involved in the magnitude estimation, normally $\Delta = 0.1$. Usually, the M_{min} is the magnitude of completeness of a seismic catalog, i.e., the magnitude threshold at which or above the corresponding seismic catalog includes all occurred EQs in the region.

6. Entropy and EQs

Now we apply the concept of Shannon entropy to EQs. Most of this section is based on [58], with some extension in order to clarify some concepts.

Given a sequence of EQs (in the form of a seismic catalog or a seismic sequence within a certain region) with non-negative (and normalized) probability P_i to have activated a certain i-th class of seismicity characterized by some range of magnitudes, the associated non-negative Shannon entropy h can be defined as [58]:

$$h = -\sum_{i=1}^{K} P_i \cdot \log P_i \geq 0. \tag{4a}$$

Since Equation (4a) is applied to a discrete number of states, h is also called *discrete Shannon entropy*. It can be considered a reliable measure of uncertainty and missing information about the system under study.

Actually, the values of magnitude can assume a continuous range (in theory from M_{min} to infinity) then the discrete definition (4a) becomes an integral definition [30,59]:

$$H = -\int_{M_{min}}^{\infty} p(M) \cdot \log p(M) dM \tag{4b}$$

where H is now called *continuous* (or *differential*) *Shannon entropy* to be distinguished from h, and $p(M)$ is the probability density function (*pdf*) of the magnitudes M, such as $p(M) = \frac{d}{dm} \sum_{i,m \leq M} P_i(m)$ and $\int_{M_{min}}^{\infty} p(M)dM = 1$.

It is worth noticing that moving from the discrete definition (4a) to the continuous (4b), H loses the property of non-negative owned by h; thus H can assume also negative values (e.g., [59]). Since this is not evident from the work by [58], we will spend here some words about it.

The two definitions of the Shannon entropy are related by the following equation:

$$H = h + \log \delta \tag{5}$$

where δ is the sampling step of the continuous *pdf* in order to let it discrete in h (e.g., [60]). It is evident from (5) that when δ tends to zero, H will diverge to $-\infty$. Thus, the continuous entropy H is not a limit for $\delta \to 0$ of the discrete Shannon entropy h and, consequently, it is not a measure of uncertainty and information. Nonetheless, the continuous Shannon entropy can be used to measure differences in information [59].

However, when the classes of magnitude are loose, e.g., for $\delta \approx 1$ we will have $H \approx h$: [58] considered $\delta = 0.5$ so the difference between discrete and continuous entropies was only 0.3.

Ref. [58] have shown that if the $p(M)$ is the GR probability distribution, then H can be expressed in terms of the b-value:

$$H \approx 0.072 - \log b \tag{6}$$

The derivation of (6) follows from the probability density function corresponding to the Gutenberg-Richter law

$$p(M) \;=\; \frac{b{\cdot}10^{-b(M-M_{min})}}{\log e} \text{ with } M \geq M_{min}. \tag{7}$$

Hence, by imposing $M_{min} \;=\; M_c$, we get

$$\begin{aligned} H \;&=\; -\int_{M_c}^{\infty} p(M){\cdot}\log p(M)dM \;=\; -\int_{M_c}^{\infty} \tfrac{b\cdot 10^{-b(M-M_c)}}{\log e}\cdot\log\left(\tfrac{b\cdot 10^{-b(M-M_c)}}{\log e}\right)dM = \\ &= -\tfrac{b}{\log e}\int_{M_c}^{\infty} 10^{-b(M-M_c)}[\log b - b(M-M_c) - \log(\log e)]dM = \\ &= -\tfrac{b}{\log e}\left\{[\log b - \log(\log e)]\int_{M_c}^{\infty} 10^{-b(M-M_c)}dM - b\int_{M_c}^{\infty}(M-M_c)10^{-b(M-M_c)}dM\right\} = \\ &= -\tfrac{b}{\log e}\left\{[\log b - \log(\log e)]\tfrac{\log e}{b} - b\tfrac{(\log e)^2}{b^2}\right\} \;=\; -\log b + \log(\log e) + \log e, \end{aligned} \tag{8}$$

i.e., Equation (6). It provides an alternative explanation of the typical decrease of b-value as seismic precursor (e.g., [61,62], for the case of 6 April 2009 M6.3 L'Aquila earthquake in Central Italy) as an increase of entropy culminating almost at the mainshock [58].

7. Entropy and Critical Point Theory

An ergodic dissipative system can have a critical point where the system undergoes through a transition. The ergodic property means that the system averages in real 3D space are equivalent to averages in the ideal reconstructed phase space (e.g., [63,64]). As an example, we can remind the behavior of the specific heat around a critical point occurring at temperature T_λ degree, when the system approaches the critical temperature as a power law. In addition, if the system changes its temperature linearly in time, the same plot is expected versus time [65].

More generally, if we replace the increasing temperature with the system entropy, then the system reaches its critical point (vertical red line in Figure 1) at the largest entropy and approaches it with an accelerating power law in its cumulative of punctuated events (we intend here for an "event" as an anomalous behavior of the system evolution, e.g., when its signal level is larger than a certain number of standard deviation, σ, e.g., 2.5 σ).

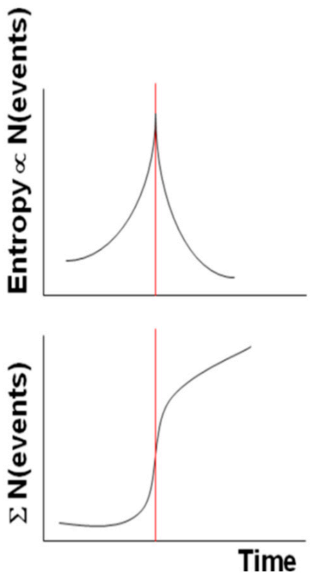

Figure 1. Idealized Shannon entropy (above diagram) and a cumulative number of events (bottom diagram) for a dissipative system around its critical point, indicated by the vertical red line.

After the critical point, the curve behaves as a decelerating power law. Figure 1 depicts both the idealized behaviors for the entropy and the cumulative number of events.

We will see in the following how these patterns are reproduced in the case studies of some Italian seismic sequences.

In seismology, the occurrence of an EQ can be considered as a phase transition, for example in the natural time domain the variance k_1 is taken as an order parameter (e.g., [66]). As we defined (and applied) the Shannon entropy, we will show that it is a reliable parameter to characterize the critical point in both the two Italian case studies. It can be considered a parameter similar to other order parameters, with the difference the latter are usually approaching a minimum value while the Shannon entropy gets the largest one.

8. Entropy Studies of Two Italian Seismic Sequences

In this part, we show two case studies in Italy: the 2009 L'Aquila and the 2012 Emilia seismic sequences, both producing a main-shock of around M6 (precisely local and moment magnitudes, ML5.9 and Mw6.2 for L'Aquila and local magnitude ML5.9 for Emilia). Main characteristics of the two seismic sequences are given in Table 1. The first case was already analyzed and discussed by [58]. However, we will make here some alternative/complementary analyses, with respect to those already published. The second case study is original and never published so far.

Table 1. Main data related to the two Italian seismic sequences under study: (from left to right) the label, the main-shock source parameters, the number of data points (foreshocks) used in the fitting stage; the maximum distance from the main-shock epicenter defining the selection area and the minimum threshold magnitude of the selected events there considered. We provide also a rough estimation of the predicted magnitude (within brackets) of the impending main-shock (see text). N and R in the Fault style column stand for Normal, and Reverse focal mechanism, respectively. R_{max} and M_{min} are the largest area and minimum magnitude, respectively, considered in the analyses of R-AMR, while for the entropy analyses we considered always the completeness magnitude (M1.4 and M2 for L'Aquila and Emilia Earthquakes).

	Sequence ID	L'Aquila	Emilia
Main-shock Parameters	Coordinate *(lat lon, in degree)*	42.34N 13.38E	44.89N 11.23E
	Depth (*km*)	8.3	6.3
	Date	6 Apr 2009	20 May 2012
	t_f (in *days* from 1 May 2005) (predicted)	1436.06 (1437.4)	2576.09 (2577.7)
	Fault style	N	R
	Magnitude (predicted) *	5.9 (5.3 ± 0.5)	5.9 (5.7 ± 0.5)
	# data (foreshocks)	17	38
	R_{max} (km)	300	300
	M_{min} (*)	4.0	4.0

* normally deduced from Equation (2a) or (2b).

In both cases we considered all earthquakes with a minimum magnitude equal to (for entropy analysis) or well above (for R-AMR; see Section 9) the completeness magnitude of the earthquake catalogs, that was found of M1.4+ and M2+ for L'Aquila and Emilia earthquake sequences, respectively.

8.1. The 2009 L'Aquila Seismic Sequence

As mentioned in [58], Shannon entropy can be estimated in three different ways: cumulative, moving overlapping or distinctively temporal windows. For the first case study, i.e., the 2009 L'Aquila (Central Italy) seismic sequence, we will consider adjacent non-overlapping moving windows. In Figure 2 we show the estimation of the Shannon entropy based on non-overlapping windows of 30 M1.4+ seismic events occurred in a circular area of 80 km around the main-shock epicenter. The low number of events used for the analysis in each window was chosen to better follow even shorter fluctuations of entropy, especially for the foreshocks. It is interesting that two distinct entropy values before the main-shock occurrence are larger than the threshold $H_t = 2.5\ \sigma$ (the mean value of entropy, $<H>$, is practically zero). To better visualize the mean behavior of entropy, the gray curve defines a reasonable smoothing of the entropy values: 15-point FFT before the main-shock and 50-point FFT smoothing after the main-shock. The different kind of smoothing is related to the different rate of seismicity before and after the main-shock. It is interesting to notice that the smoothed gray curve of the Shannon entropy reproduces the expected behavior of a critical system around its critical point, with the main-shock as a critical point.

We can even analyze in more detail the same curve but expanded in the period before the main-shock (Figure 3). We confirm that, around 6 days before the main-shock, there is the persistence of two consecutive values of entropy greater than 2.5σ (the larger value is even greater than 10σ). An interesting question to better investigate in more case studies will be: could this persistence of larger values of entropy be considered a reliable precursor of the imminent main-shock?

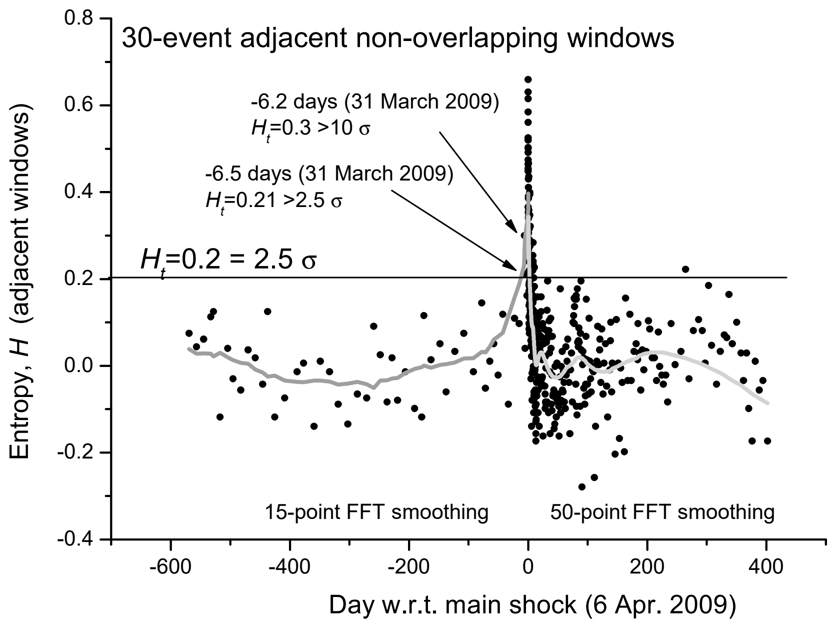

Figure 2. Shannon entropy for L'Aquila seismic sequence from around 1.5 years before the main-shock to around 1 year after, calculated for a circular area of 80 km around the main-shock epicenter. Each point is the entropy analysis based on non-overlapping windows, each composed by 30 foreshocks. The gray curve defines a reasonable smoothing of the entropy values: 15-point FFT before the main-shock and 50-point FFT smoothing after the main-shock. The different kind of smoothing is related to the different rate of seismicity before and after the main-shock. It is interesting how the smoothed curve reproduces the expected behavior of a critical system around its critical point. (Adapted from [67]).

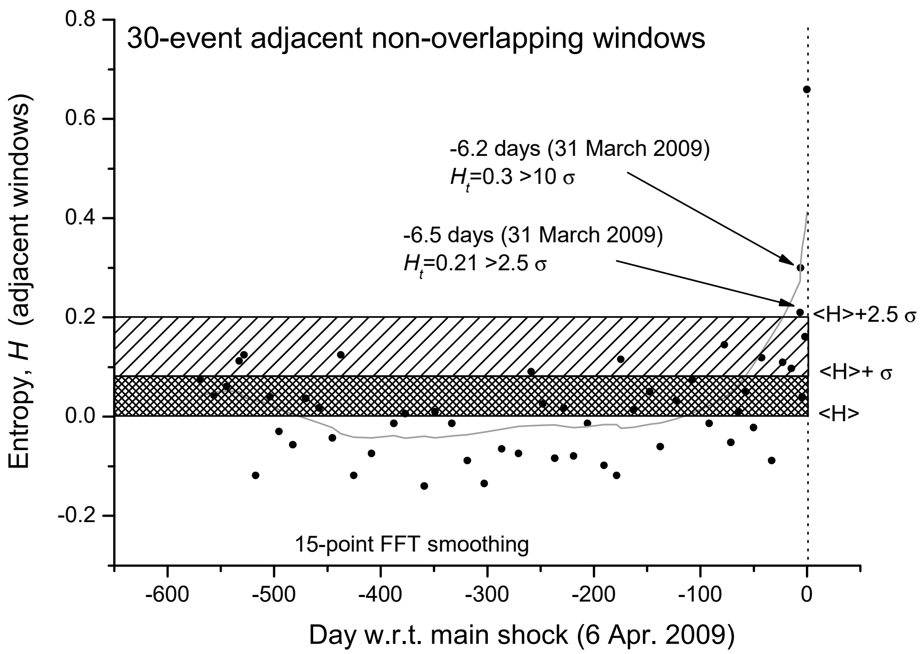

Figure 3. Details of the Shannon entropy for L'Aquila seismic sequence from around 1.5 years before the main-shock to the main-shock occurrence. Each point is the entropy analysis based on non-overlapping windows, each composed by 30 foreshocks. The mean value of the entropy, <H>, which is almost zero, and one and two standard deviations are also shown. The gray curve defines a reasonable smoothing of the entropy values with 15-point FFT.

8.2. The 2012 Emilia Seismic Sequence

In this specific case study, we will consider moving and partially overlapping windows, each composed of around 200 seismic events and overlapping of 20 events. This kind of analysis allows us to have directly a smoother curve of entropy, without resorting to a subsequent smoothing operation as done instead in the previous case.

In Figure 4 we plot the Shannon entropy for the Emilia seismic sequence from 2000 to 2014, as estimated overall M2+ EQs occurred around 150 km from the first major EQ. The significant increase starting around 2010 is probably real and related to the preparation phase of the two major EQs occurred on 20 and 29 May, 2012 with local magnitudes 5.9 and 5.8, respectively, where the entropy reaches the maximum value (in this case around 0.3). The gray area defines the estimated error in computing the entropy.

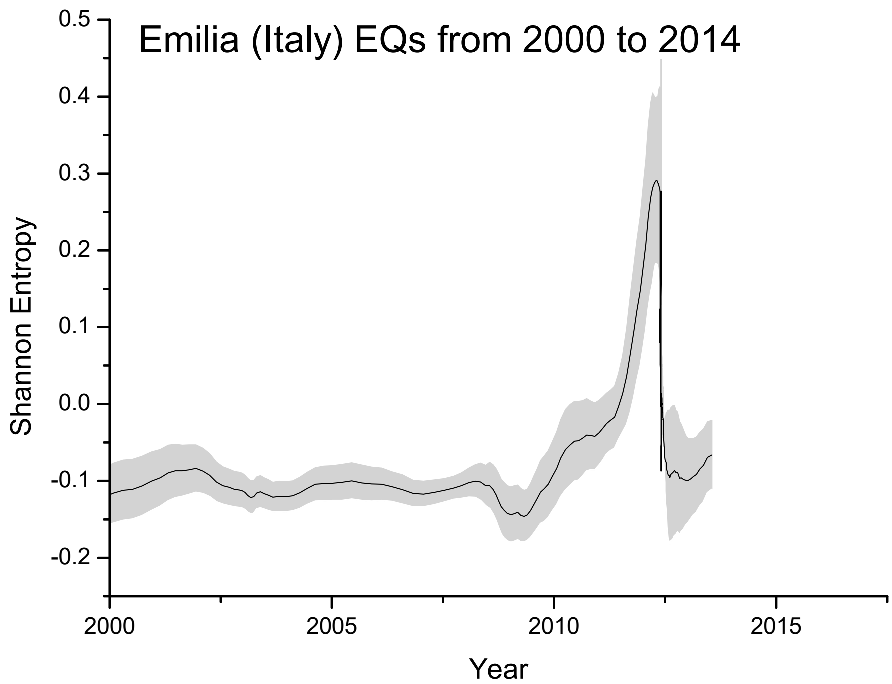

Figure 4. Shannon entropy for the Emilia seismic sequence from 2000 to 2014. The significant increase from around 2010, with the maximum at around the main-shock occurrence, is expected to be real. The gray area defines the statistically estimated (one standard deviation) error in computing the entropy.

As a general remark of this section, it is true that we have applied the entropy analysis to two case studies only, but in most occasions, we could extend the found results by analyzing *b*-value to the entropy, via Equation (6). The introduction of the Shannon entropy in the analysis of a seismic sequence provides a more physical and statistical meaning to the potential precursory decrease of the *b*-value in terms of an increasing entropy of the underlying physical system.

Precursory entropy changes have been also observed when analyzing the seismic data in natural time [66] and using for the computation a sliding window comprising a number of events that occur within a few months or so, which is the lead time of the precursory seismic electric signal activities [68] detected before major earthquakes. For example, almost three months before the 2011 M9 Tohoku earthquake in Japan it was recently found [69] that the entropy change under time reversal exhibited an unprecedented minimum. Such a minimum has been also observed before the M8.2 Mexico earthquake that occurred on 7 September 2017 [70].

9. Accelerated Moment Release Revisited: The Case of L'Aquila and Emilia EQs

Reference [71] proposed a simple way to estimate the strain-rebound increment, $\varepsilon_{i:}$

$$s_i = \sqrt{E_i} = k_i \cdot \varepsilon_i \tag{9}$$

where E_i is the energy released by the EQ, i.e., $10^{\alpha M + \beta}$ ($\alpha = 1.5$, $\beta = 4.8$ for energy expressed in Joule, although Benioff used slightly different values), and $k_i = (\mu P V_i/2)^{0.5}$ (μ = shear or rigidity modulus, V_i = volume of the i-th fault rocks, P is the fraction of energy transmitted in terms of seismic waves; usually it is considered $P \approx 1$). This theory is based on [72] arguments of the elastic rebound.

To take account the cumulative effect of a series of N EQs at the time t of the last N-th EQ, Benioff introduced therefore what is now called the cumulative Benioff strain:

$$s(t) = \sum_{i=1}^{N(t)} s_i = \sum_{i=1}^{N(t)} \sqrt{E_i} = 10^{\beta'} \sum_{i=1}^{N(t)} 10^{0.75 M_i} \tag{10}$$

with $\beta' = \beta/2 = 2.4$. It is important to notice that, according to [71], the cumulative strain (8) is that accumulated on the fault under study.

Extending the meaning of (10) to the strain accumulated over a larger area around the epicenter, [73] obtained interesting results with the so-called accelerating moment release (*AMR*) approach that consists in fitting the cumulative value $s(t)$ expressed as in Equation (8), with a power law in the time to failure t_f, i.e., the theoretic time of occurrence of the main shock: $s(t) = A + B(t_f - t)^m$, where A, B and m are appropriate empirical constants (m is expected between 0 and 1: typical value is 0.3; [37]). The fitting process gives as an outcome the time t_f together with the expected magnitude, which is related to either A or B:

$$M_p(A) = \frac{\log(\Delta s_{last}) - \beta'}{0.75} \tag{11a}$$

where $\Delta s_{last} = A - s_{last}$ and s_{last} are the cumulative Benioff strain at the last precursory event considered (namely the N-th EQ). In this expression, one speculates that the main-shock will be the next EQ striking after the N-th, but the occurrence of many smaller EQs after the last analyzed shock and before the predicted time t_f cannot be excluded.

An alternative formulation, based on the parameter B, has been given by [74]:

$$M_p(B) = \frac{\log|B| - \beta' - 0.14}{0.738}. \tag{11b}$$

Criticism to this method came from [75] who pointed out the arbitrariness in the critical choice of the temporal and spatial criteria for data selection, i.e., the initial precursory event of the *AMR* curve and the extension of the inspected region. On the other hand, [76] explained the AMR phenomenon under the view of complexity principles.

To circumvent this criticism, [38] introduced what they called R-AMR, i.e., the revised accelerating moment release (R-AMR), as a better way of applying the AMR by weighting the EQs magnitudes in a certain area, according to an appropriate attenuation function $G = G(R)$, where R is the distance of a given EQ epicenter with respect to the impending slipping fault. In particular, the Benioff Strain produced at the fault level is expressed by a reduced Benioff strain $\hat{s}(t) = s{\cdot}G$ called "reduced" because the action of the function G, which is normally less than unity (i.e., $G \le 1$), is to diminish the value of the typical Benioff strain, normally according to the distance R from the center of the region of study. As an area of interest, a circle is taken with the corresponding Dobrovolsky radius, $r(km) = 10^{0.43M}$ with M = EQ magnitude [16].

Thus, the expression for the cumulative reduced strain becomes:

$$\widetilde{s}(t) = \sum_{i=1}^{N(t)} \widetilde{s_i} = \sum_{i=1}^{N(t_i)} \sqrt{E_i} \cdot G(R_i) = 10^{\beta'} \sum_{i=1}^{N(t_i)} 10^{0.75M_i} G(R_i). \quad (12)$$

Ref. [38] applied with success their revisited method to the three most important seismic sequences occurred in Italy in the previous ten years with respect that publication. In addition, they also showed that, for a particular seismic swarm (i.e., with no mainshock), R-AMR performs better than AMR, not providing a false alarm.

R-AMR for the 2009 L'Aquila and 2012 Emilia Seismic Sequences

We show here two case studies, L'Aquila and Emilia seismic sequences, where the application of R-AMR is made much simpler than the one firstly proposed in [38]. Although that way of applying of R-AMR is more rigorous because all EQs above the minimum magnitude of completeness are considered, we show here that a simpler application is also possible, where considering a very simple attenuation function of the form $G(R_i) = d/R_i^{\gamma}$, with d (normally 1km), R_i in km and with $\gamma \approx 1$, at the cost of considering a larger minimum magnitude threshold of around M4. Figures 5 and 6 show the results for the cases of L'Aquila and Emilia sequences, respectively, where we apply to all shallow (depth $h \leq 40$ and $h \leq 80$ km, respectively) M4+ EQs both AMR and R-AMR analyses (top and bottom of each figure, respectively). Then, we consider a 300 km size for the regions where we applied R-AMR analysis. This size is comparable with the corresponding Dobrovolsky's radius. Both the analyses stop well before the main-shocks that are not considered in the calculations. We notice that the time of preparation is rather long for both sequences, i.e., practically starting at the beginning of the whole period of investigation (May 2005). This fact could be simply interpreted as the larger foreshocks anticipate the beginning of the seismic acceleration with respect to the smaller ones, which were the most in the previous analyses in [38].

The goodness of the power law fit with respect to the linear regression can be quantified by the C-factor which is the square root of the ratio between the RMS of the power law and the RMS of the best linear fit [77]: the lower the C-factor than 1, the better the power law fit is with respect to the line.

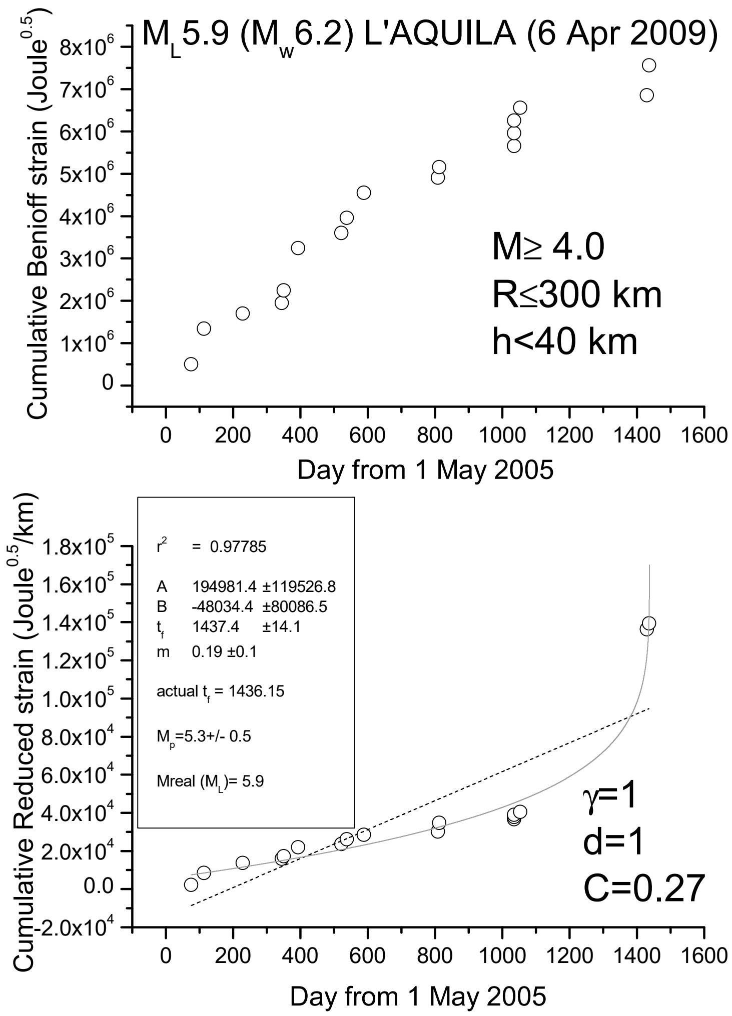

Figure 5. Analyses of L'Aquila seismic sequence $M \geq 4$ EQs (main-shock not shown and not used in the analysis): (top) ordinary AMR method; (bottom) R-AMR method. The dashed line represents the best linear fit, while solid gray curve is the best power law fit. Results of the fit are shown in the frame inside the graph at the bottom; r^2 is the coefficient of determination, providing a measure of the quality of the fit (the closer to 1, the better the fit).

We find a clear seismic acceleration for both seismic sequences, quantified by a low value of C (0.27 for L'Aquila sequence and 0.46 for Emilia sequence) and a great determination coefficient ($r^2 > 0.95$ in both cases). In addition, the predicted magnitudes are comparable with (although lower than) the real ones. In both cases, the beginning of clear acceleration starts around 1.5 years before the main-shock.

The above cases represent two of the four seismic sequences happened in Italy in the last 15 years. Another seismic sequence, occurred in south Italy in 2010 and culminated with an M5 in the Pollino area, shows an analogous acceleration before the mainshock [38]. Only the most recent seismic sequence of the Amatrice-Norcia (Central Italy) earthquakes in 2017 had neither acceleration nor foreshocks before the first major earthquake (24 August 2016 M6 Amatrice earthquake). Therefore, the two case studies shown here are very representative of the most recent seismicity in Italy that has expressed in terms of a series of earthquakes culminating with a mainshock.

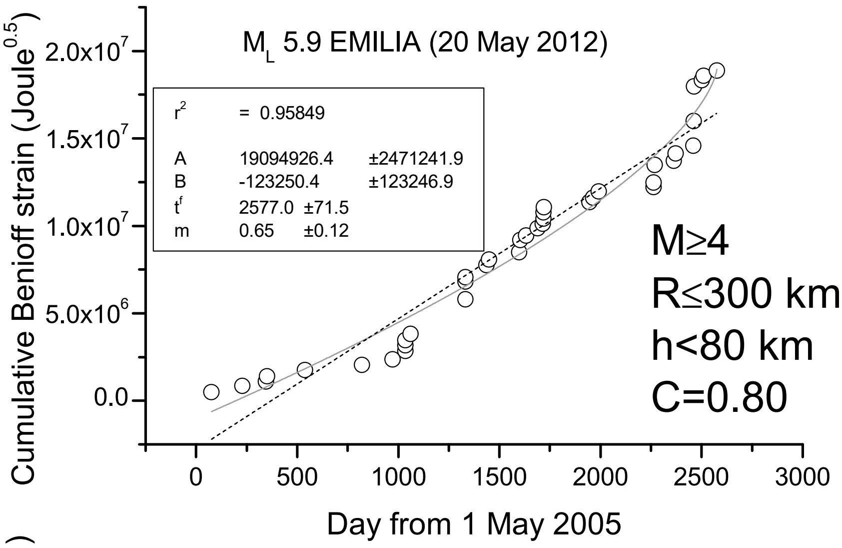

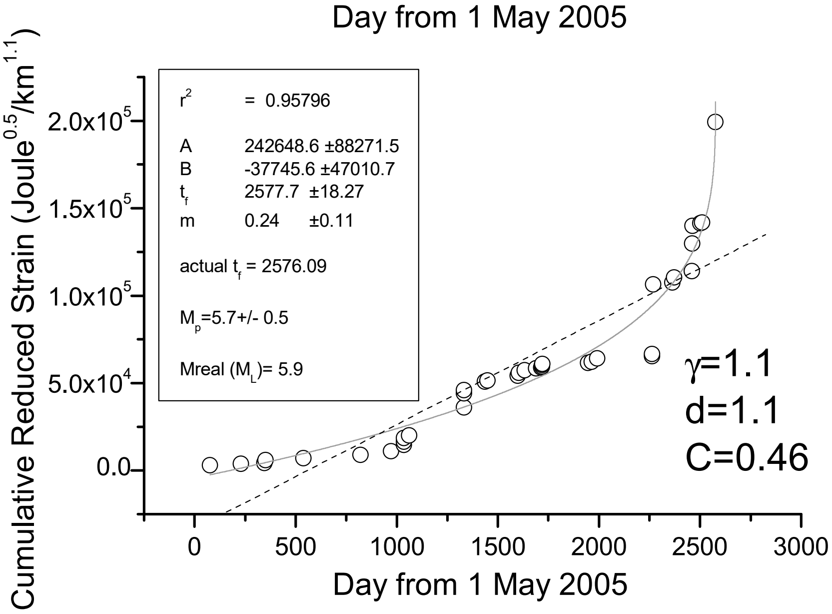

Figure 6. Analyses of Emilia seismic sequence $M \geq 4$ EQs (main-shock not shown and not used in the analysis): (top) ordinary AMR method; (bottom) R-AMR method. Here the ordinary AMR also showed a little acceleration (*C*-factor = 0.80) but the R-AMR version is much better (*C*-factor = 0.46). The dashed line represents the best linear fit, while the solid gray curve is the best power law fit. Results of the fit are shown in the frames inside the graphs; r^2 is the coefficient of determination, providing a measure of the quality of the fit (the closer to 1, the better the fit).

10. Lithosphere-Atmosphere-Ionosphere Coupling (LAIC)

Geosystemics [6,7] sees the planet in its entireness, where all geo-layers "communicate" each other, in terms of exchange of matter and/or energy, i.e., what [22] called with the more generic term of "information". In the last two decades, an important model, so-called lithosphere-atmosphere-ionosphere coupling (LAIC) proposes that some precursory anomalies can appear in the atmosphere and/or ionosphere before a large EQ, during its preparation phase (e.g., [78]).

The state of the ionosphere is particularly sensitive to the LAIC. Its presence as an ionized layer at 50–1000 km altitude above the Earth's surface is important to detect any electromagnetic change in the circumterrestrial environment [79]. Comprehensive reviews of the papers that describe the measurements of the seismo-ionospheric signals are reported in [20] and [80]. In addition, [81] made a discussion on the temporal and spatial variability of the ionospheric precursor summarizing the results obtained by a large number of authors so far. In particular, they describe in detail what is the role of the global electric circuit in transferring information from the Earth's surface up to the ionosphere.

The finding of atmospheric anomalies prior to large EQs is more recent and widely debated as well.

In this section, we remind some of those phenomena, the nature and characteristics of which are more directly of interest for the understanding of LAIC.

10.1. Pre-EQ Ionospheric Evidences from Ground-Based Observations

A coupling (post-seismic) effect of an EQ to the above atmosphere is already well known: it can appear just after the occurrence of a sufficiently large event, and it is related to the possibility of observing the effect of the propagation of acoustic-gravity waves in the ionosphere (e.g., [82]). Ref. [83] reported one of the first reports of total electron content (TEC) anomalies due to coseismic gravity waves. They found an anomaly in vTEC that propagated from near field to around 1000 km just after the M7.9 12 May 2008 Wenchuan earthquake. Recently, this effect has been clearly detected as wave-like fluctuations of the TEC in ionosphere 21 min after the April 25, 2015, M7.8 Nepal EQ ([84]; last access on 17 November 2018).

Important precursory effects of LAIC before large EQs can be detected in the ionosphere from ground-based observational systems like ionosondes and GPS (global positioning system)/GNSS (global navigation satellite system) receivers.

A large number of papers report some variations of ionospheric parameters before many large EQs, such as the F2-layer critical frequency (foF2) [36,85–89] and the sporadic E layer (Es) [90–92].

The study of foF2 alone is a very "inconvenient" ionospheric parameter for the role of EQ precursor, because, besides the geomagnetic activity effects, there would be many other reasons for non-EQ related foF2 variations. Therefore, in order to achieve a more robust result, a multi-parameter analysis is preferable and some works have analyzed more ionospheric parameters at the same time. For instance, in the periods of time preceding all crustal EQs in Central Italy with magnitudes $M > 5.0$ and the epicenter depth < 50 km, [88] considered the ionospheric sporadic E layer (Es) together with the blanketing frequency of Es layer (fbEs) and foF2, by analyzing data from the ionospheric observatory inside the preparation zone. According to these authors, the found deviations of ionospheric parameters from the background level can be related to the magnitude and the epicenter distance of the corresponding EQ. Very recently, the same procedure has been systematically applied for the first time to Greek earthquakes in the frame of the SAFE project [36]. Table 2 shows the confusion matrix of the statistics from which we can estimate the overall accuracy, A = 69%, hit rate of success, H = 50% and the false alarm rate, F = 26% (for their definition, please see, e.g., [93]). These values are encouraging because confirm the robustness of the technique and statistically prove the validity of the method, quantifying the higher significance of the found results with respect to casual events.

Table 2. Confusion matrix for pre-earthquake anomaly detection obtained from ionospheric anomalies analysis in Greece from 2003 to 2015 (adapted from [36]).

Ionospheric Anomaly	Seismicity	
	Yes	No
Yes	5	9
No	5	26

There is significant literature related to the analysis of the ionospheric effects before and during an EQ revealed by GPS/GNSS ground-based measurements, in terms of TEC fluctuations and scintillation anomalies that have been claimed to be detected some days before the EQs. Just to mention the more recent works, [94] analyzed 5 years of GNSS-based ionospheric TEC data by producing maps over an area surrounding the epicenter of the 2009 L'Aquila EQ. In the night of 16 March 2009, an interesting ionospheric anomaly was found, anticipating the main shock by 3 weeks, which could be connected with it. [95] reported on the analysis of the TEC from eight GPS stations of the EUREF network by using discrete Fourier to investigate the TEC variations over the Mediterranean region before and during the 12 October 2013 Crete, Greece EQ. Over an area of several hundred kilometers from the EQ epicenter, all stations used in this study observed an increase of 2-6 TECU from 10 October to 15 October 2013, likely related to the EQ. [96] applied a complex algorithm, the Firefly Algorithm (FA), as a robust predictor to detect the TEC seismo-ionospheric anomalies around the time of the some powerful EQs (27 February 2010 M8.8 Chile, 11 August 2012 M6.4 Varzeghan and 16 April 2013 M7.7 Saravan). Significant anomalies were observed 3–8 days before the EQs.

A recent paper by [97] presented the application of the LAIC model to compute the TEC variations and compare the simulation results with TEC observations for the Tohoku-Oki EQ (Japan, 11 March 2011, Mw 9.0). In the simulations, these authors assumed that the stress-associated current starts ~40 min before the EQ, and then linearly increases reaching its maximum magnitude at the time of the EQ main-shock. Comparisons with experimental values suggest that a dynamo current density of ~25 nA m^{-2} is required to produce the observed variation of ~3 TECU.

However, it is worth noting that the relationship between ionospheric anomalies and electromagnetic signals generated by the EQ preparation is still controversial and highly debated, as demonstrated by the high number of papers reporting a re-analysis of data and comments aiming to refute evidence of this correlation. For example, [98] commented on the findings of [99]. After a re-analysis of the data, used by Heki (2011) to demonstrate the existence of a TEC anomaly 40 min before the 2011 Tohoku-Oki EQ and other M > 8 EQs, [100] concluded that this anomaly was due to an artefact introduced by the choice of the definition of the reference line adopted in analyzing TEC variations. However, more recently [101] came back again to the question with a deeper and more convincing analysis that the change of TEC was real and not an artefact because for the 2011 Tohoku-Oki EQ the TEC change was simultaneous all over the globe.

10.2. Pre-EQ Ionospheric Evidence from In-Situ Measurements

Although many works on the possible pre-EQ effects in the ionosphere were performed with the early advent of satellites, it was with the DEMETER (Detection of Electro-Magnetic Emissions Transmitted from EQ Regions; 2004–2010) and CHAMP (CHAllenging Minisatellite Payload; 2000–2010) missions that most of the striking results were obtained.

DEMETER was a French micro-satellite operated by CNES and specifically designed to the investigation of the Earth ionospheric disturbances due to seismic and volcanic activities. It operated for more than 6.5 years of the scientific mission (2004–2010). The results from the analyses of this satellite dataset seem to have statistically proved definitively the existence of the LAIC, however, it is still needed to understand the deterministic details. Using the complete DEMETER data set [102], careful statistical studies were performed on the influence of seismic activity on the intensity of low-frequency EM waves in the ionosphere. The seismic database used for these analyses was constituted by several thousands of magnitude M5 + EQs occurred the satellite lifetime. In particular, the normalized probabilistic intensity obtained from the night-time electric field data was below the "normal" level, shortly (0–4 h) before the shallow (depth < 40 km) M5+ EQs at 1–2 kHz. Clear perturbations were observed a few hours before the EQs, as another example of "imminent" forecast: they are real, although they are weak and so far only statistically revealed. No similar effects were observed during the diurnal hours and for deeper EQs. It is interesting also to note that the spatial scale R of the affected area is approximately 350 km confirming relatively well the size of the EQ preparation zone estimated using the [16] formula. The main statistical decrease is observed at about 1.7 kHz, corresponding approximately to the cut-off frequency of the first transverse magnetic (TM) mode of the Earth–ionosphere waveguide during the night-time. An increase of this cut-off frequency effect would therefore necessarily lead to the decrease of the power spectral density of electric field fluctuations observed by DEMETER in the appropriate frequency range, meaning a lower height of the ionosphere above the epicenter of the imminent EQ. As the EM waves propagating in the Earth-ionosphere wave-guide are mainly whistlers, this means that their propagation is disturbed above the epicenters of future EQs, instead of a change of their intensities.

Refs. [103,104] took advantage of the simultaneous measurements of these two satellites: they analyzed the electron density and temperature, ion density composition and temperature data from DEMETER ISL (Langmuir probe), ICE (electric field instrument) and IAP (plasma analyzer Instrument), together with CHAMP PLP data (electron density and temperature) and IONEX maps of vTEC (vertical TEC) from IGS (International GNSS Service). They investigated the ionospheric fluctuations related to the EQs occurred in September 2004 near to the south coast of Honshu, Japan [103] and Wenchuan EQ (M7.9) of 12 May 2008 [104]. The main result was the detection of a gradual enhancement of the EIA (Equatorial Ionospheric Anomaly) intensity starting one month prior to the event, reaching its maximum eight days before, followed by a decreasing behavior, very likely due to an external electric field generated over the epicenter affecting the existing $\mathbf{E}{\times}\mathbf{B}$ drifts responsible of the EIA.

Ref. [105] confirmed and improved the previous results on the full lifetime of the DEMETER satellite. Their main result is that there is a significant positive or negative deviation of ion density around five days before the earthquake occurrence within 200 km of the future epicenter.

By analyzing the magnetic data from Swarm satellites of the European Space Agency, a recent paper [106] found some important patterns before the April 25, 2015, M7.8 Nepal EQ, that resemble the same obtained from the seismological analysis of the foreshocks.

Other two large earthquakes have been investigated by the same approach as [106]. They are the M7.8 16 April 2016 Ecuador [107] and M8.2 8 September 2017 Mexico earthquakes [108], confirming a particular pattern in the cumulative number of the Y magnetic component swarm anomalous tracks. In these two works, the turning point anticipates the earthquake of about 9 and 100 days, respectively. A comparison of the daily level of the geomagnetic field, electron density and electron temperature in the Dobrovolsky area by detailed time series analyses was applied by finding other possible evidence for ionospheric EM effects induced by lithospheric activity.

10.3. Pre-EQ Atmospheric Evidence

The improvement and increase of satellite remote sensing missions go back to the early 1980s. Since then, evidence of many types of infrared (IR) physics parameters have been recognized as useful to identify possible pre-EQ anomalies. Among them, the most cited are the brightness temperature (BT), outgoing longwave radiation (OLR), surface latent heat flux (SLHF), skin surface temperature (SST), and the atmospheric temperature at different altitudes. Although the topic is still debated or even controversial, many scientists agree that those parameters could change during the preparation phase of EQs and so they are regularly recorded by satellite at regional and global scales. [96,109,110] carried out studies where found variations of temperature or aerosols. [111] found a clear BT anomaly (BT corresponds to the temperature of a black body that emits the same intensity as measured), in correspondence of Lushan M7 EQ (China). On the other hand, OLR is the emission of the terrestrial radiation from the top of the Earth's atmosphere to space; it is controlled by the temperature of the Earth and the atmosphere above it, in particular, by the water vapor and the clouds. [112] reported anomalies in this parameter days before the seismic events. SLHF describes the heat released by phase changes and shows an evident dependence on meteorological parameters such as surface temperature, relative humidity, wind speed, etcetera. SST is the temperature of the Earth's surface at radiative equilibrium (usually, the interface between soil and atmosphere, on lands; it is identical to Sea Surface Temperature over the seas), in contrast with the meteorological definition of surface temperature measured by air thermometers which take readings at approximately 1 m above ground level. We will study the SST for the epicentral areas of the L'Aquila and Emilia main-shocks.

The nature of the detected IR anomaly as a real temperature change, or perhaps just an emission in the IR frequency band, is a debated issue. In a recent paper, [113] showed a clear thermal IR (TIR) anomaly preceding the 2009 M6.2 L'Aquila (Italy) EQ. The authors proposed a mechanism of generation of electric currents in the lithospheric rocks when they are under stress and a consequent IR irradiation with no actual temperature change (e.g., [114]). However, some recent works identified SLHF [115] and surface temperature anomalies [116] occurring before large EQs, thus supporting the possibility for some actual change of temperature too. However, according to Freund (personal communication), this is only an apparent paradox because any stimulated IR emission from vibrationally very "hot" systems is not a "clean" process. Eventually, the system will "thermalize", meaning literally that each newly formed peroxy bond on the surface of the Earth will become a "hot spot", surrounded by a small halo where the neighboring atoms have actually increased their Joule temperature. Although the exact cause of such temperature rise is still unknown, it is possible to definitely exclude the radon as a possible direct heat source, based on the results of laboratory experiments conducted by [117]. Ref. [118] resort to another role of radon as a possible indirect source: it could drive particle ionization and aerosol aggregation, where the latent heat release can cause the found increase in the atmospheric temperature.

Application of particularly sophisticated techniques is mandatory to identify the anomalous signal in the TIR data. For instance, [119–122] propose some robust satellite techniques that take into proper account the past behavior of the signal under investigation: the typical seasonal and yearly background is computed and statistically significant deviation from it may represent the thermal anomaly. [123] focused the attention on the air-quality data as possible indicators of an impending EQ: these authors found a staggering increase in ambient SO_2 concentrations by more than one order of magnitude across Taiwan several hours prior to two (M6.8 and M7.2) significant EQs in the island.

Although still controversial, an interesting emerging study concerns the EQ clouds [124], suggesting that their formation is due to some local weather conditions caused by energy and particle exchanges between crust and atmosphere. This process is believed to be able to locally modify the global electric circuit during the EQ preparation phase (e.g., [125]); or to create the conditions for electrical discharges in an atmosphere that may be the source of very high frequency (VHF) radio-emissions, sometime detected prior to large EQs [126]. Recently, the claim of unusual cloud formation prior strong EQs by [124] was strongly questioned by [127] with a counter-analysis based on examination of 4 years of satellite images and correlation analyses between linear-cloud formations and EQ occurrence.

10.4. Physical Models

A plausible physical omni-comprehensive model justifying the great variety of evidence given before is the real difficult conundrum for the scientists in this field. There are many theories that attempt to describe the physical processes manifesting anomalous behavior in some parameters before the occurrence of an EQ and try to explain what could cause these precursors. Several reviews of these processes can be found in [78,114,128] and the references therein (Figure 7).

There exist many proposed mechanisms of generations to explain the LAIC, which can generally be classified as those based on mechanical (atmospheric waves generated by earth motions) and electrical (electric fields in Earth's crust) sources: among the former, we can count the various kinds of atmospheric waves as internal or acoustic-gravity waves (IGW and AGW, respectively), planetary waves and tides. In particular, the hypothesis of acoustic-gravity waves generation before EQs was proposed by many authors (e.g., [78]; and more recently, [129]).

The mechanisms that describe the anomalous electric field generation are more complex and intriguing. A theory that could explain many observations is based on the emission of radioactive gas or metallic ions before an EQ, which might change the distribution of electric potential above the surface of the Earth and then up to the ionosphere (e.g., [130]).

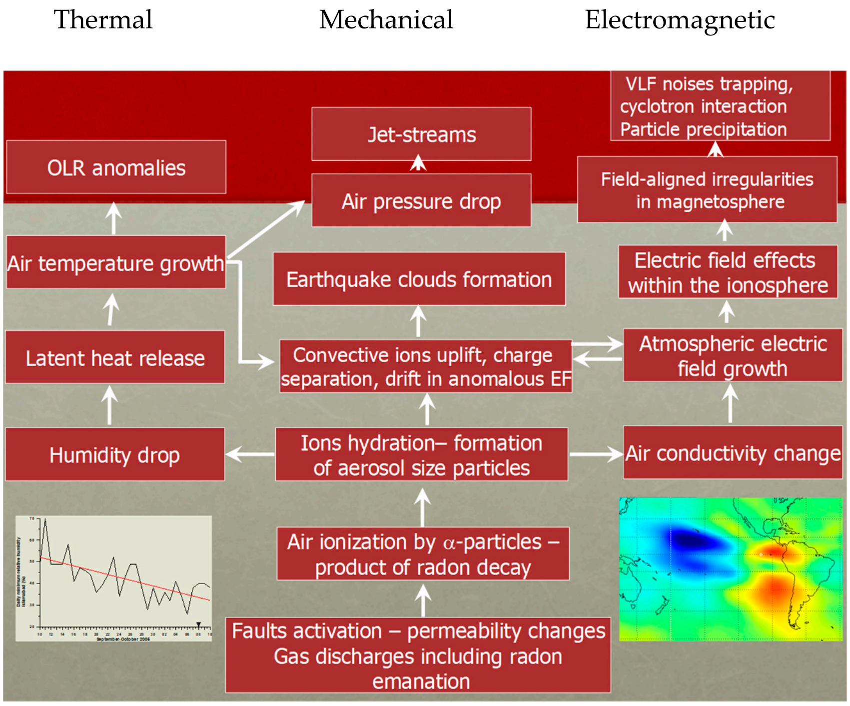

Figure 7. Pulinets-Ouzonouv LAIC (Lithosphere-Atmosphere-Ionosphere_Coupling) model (adapted from [118,128]).

Whatever its source is, penetration of the electric field into the ionosphere could induce anomalies in the ionospheric plasma density and/or conductivity, which are observed above seismic zones (see e.g., [86,131]). In contrast with this view, [125] proposed that radon emitted before an EQ would increase the conductivity of air at ground level and that the ensuing increase of current in the fair weather global circuit would descend the ionosphere. This mechanism is also supported by [118]. However, [132] estimated that even if radon is coming out the ground in seismic areas, its contribution to the air conductivity is of minor importance relative to the air ionization rate, which can be expected from charge carriers from the rocks, the so-called positive-holes (or p-holes) (Figure 8).

They showed experimentally that these mobile electric charge carriers flow out of the stressed rocks (see [132], and references therein) and, at the Earth's surface, they cause extra ionization of the air molecules. However, the original experiments that detected these p-holes have been recently contrasted [133] (but see also [134]).

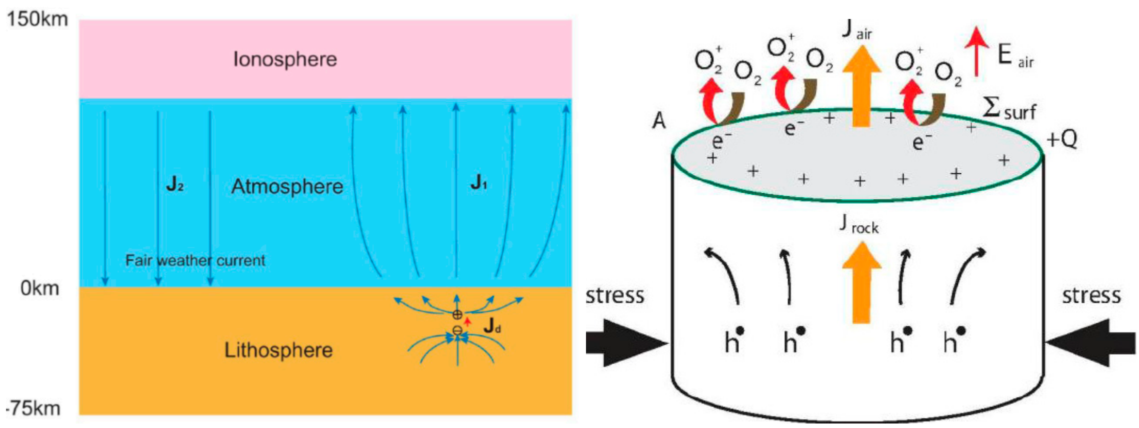

Figure 8. Freund model (adapted from [136]).

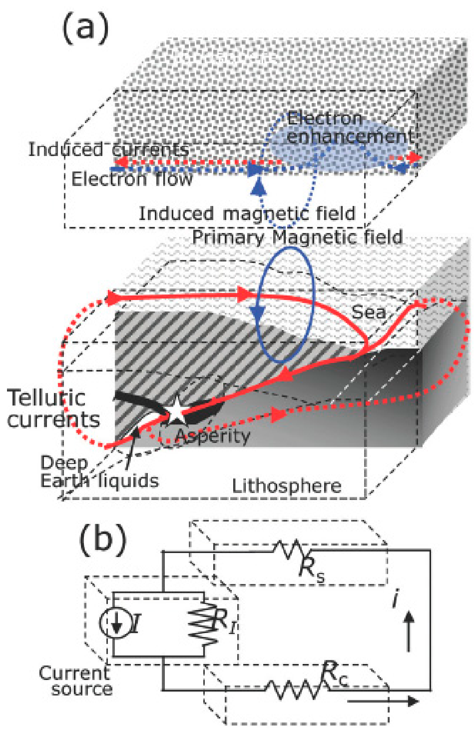

Figure 9. Enomoto model (adapted from [137]).

Refs. [135,136] showed that ionospheric density variations could be induced by changes of the current in the global electric circuit between the bottom of the ionosphere and the Earth's surface where electric charges associated with stressed rocks can appear. The interaction of the anomalous electric current with the geomagnetic field can even amplify the effect in the higher atmosphere [136].

Ref. [137] introduced a fault model that takes account of the couple interaction between EQ nucleation and deep Earth gases and proposed a physical model of magnetic induction coupling with ionosphere before large offshore EQs (Figure 9).

11. Examples of Thermal Coupling before L'Aquila and Emilia EQs

An important feature in the LAIC model should be the coupling between the lithosphere and the low atmosphere (i.e., the troposphere) in terms of thermal coupling. While the thermal coupling in case of volcanic eruptions is quite clear and convincing (e.g., [138]), that for earthquakes is more controversial. As was mentioned in the previous section, no general consensus exists about the fact that the thermal anomaly is just an infrared effect (e.g., [114]) or a real change of temperature (e.g., [116]). We do not want to express here a clear position in this debate. Rather, as didactical examples, we will show some SST studies for the same cases we analyzed for the entropy, i.e., the 2009 L'Aquila and the 2012 Emilia sequences of EQs.

In each case study, we will consider the SST in the epicentral region about two months around the EQ occurrence, and then we will compare the temperatures with those measured in the same day, at the same time (06:00UT) in the time interval 1979-2008 (2011) for L'Aquila (Emilia) EQ. An anomaly of the physical quantity of concern is defined as a value that exceeds the mean (or median) by two times the standard deviation and persists for at least two days (see also [35]).

Figures 10 and 11 show the results for the two analyses. In detail, Figure 10 (Figure 11) shows for L'Aquila (Emilia) EQ the median behavior of 2009 (2012), from 1 March (April) to 30 April (31 May), compared with all 1979–2008 (2011) medians, and particular comparison with 2003 (2004) and 2005 (2006) medians. For each day, the use of the median was preferred because it was thought to be a more robust indicator. The latter years have been used for comparison because no significant seismicity occurred in those years in the two considered regions. All values have been estimated at the EQ epicenter. The red oval indicates when the thermal anomaly in 2009 (2012) is larger than or equal to 2 standard deviations, σ (as computed for each day from the previous 1979–2008 (2011) years) and persists for at least two days. In both analyses, a clear anomaly is found around a week before the EQ occurrence (vertical line in both figures). In the case of Emilia EQ, another persisting anomaly is also found around 1 month and a half before the main-shock.

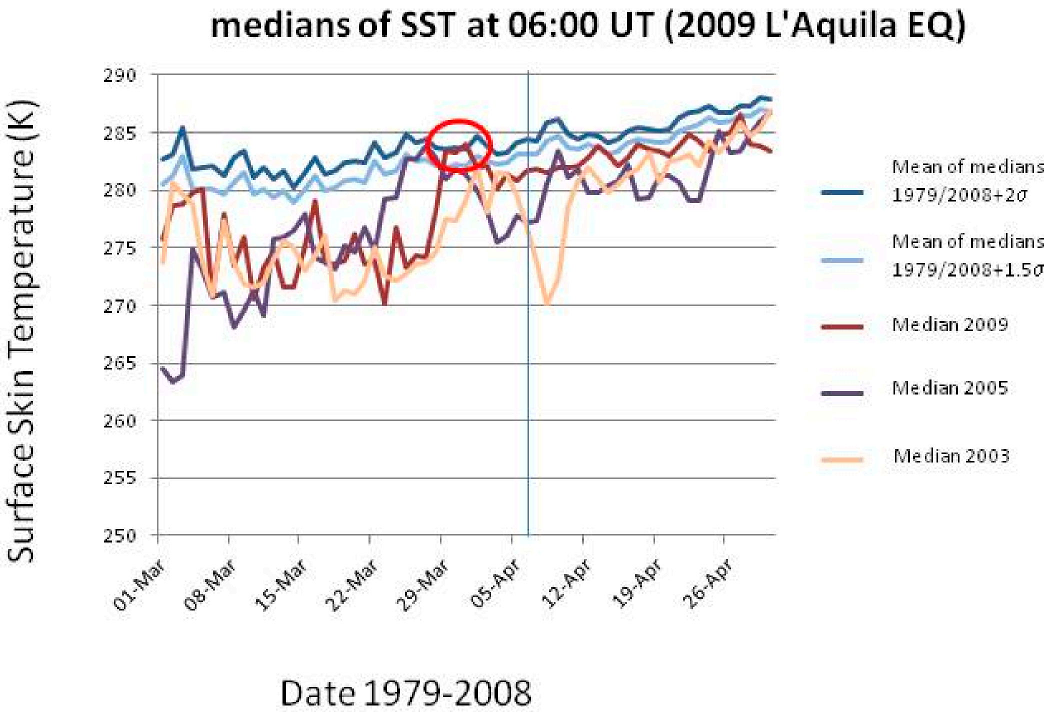

Figure 10. Median behavior of 2009 from 1 March to 30 April, compared with all 1979–2008 medians, and particular comparison with 2003 and 2005 medians. All values have been estimated at the epicenter. The red oval indicates when the thermal anomaly in 2009 is larger than or equal to 2 standard deviations, σ (as computed from the previous 1979–2008 years) and persists for at least two days. The vertical line is the EQ occurrence.

These results confirm some previous studies on the possible thermal coupling in the two EQ cases (e.g., [113,116]). Central Italy showed an analogous thermal anomaly around 40 days before the recent 24 August 2016 M6 Amatrice EQ: [35] applied the CAPRI algorithm (CAPRI stands for "Climatological Analysis for seismic PRecursor Identification") that removes the long-term trend over the whole day by day dataset. This procedure is used mainly to remove a possible "global warming" effect, avoiding to classify as abnormal a more recent year just because of global warming. These authors integrated the analysis of the skin temperature (skt) also with total column water vapor and total column of ozone and made a confusion matrix analysis for the last twenty years. As an example, Table 3 shows the confusion matrix of the validity of the skt as precursor applied to Central Italy earthquakes from 1994 to 2016. The following results are obtained: overall accuracy = 74%, hit rate of success = 40%, false alarms = 17%, (for more details please see [35]). These values confirm the validity of this thermal parameter as a potential pre-earthquake indication, at least for the area of concern, i.e., Central Italy.

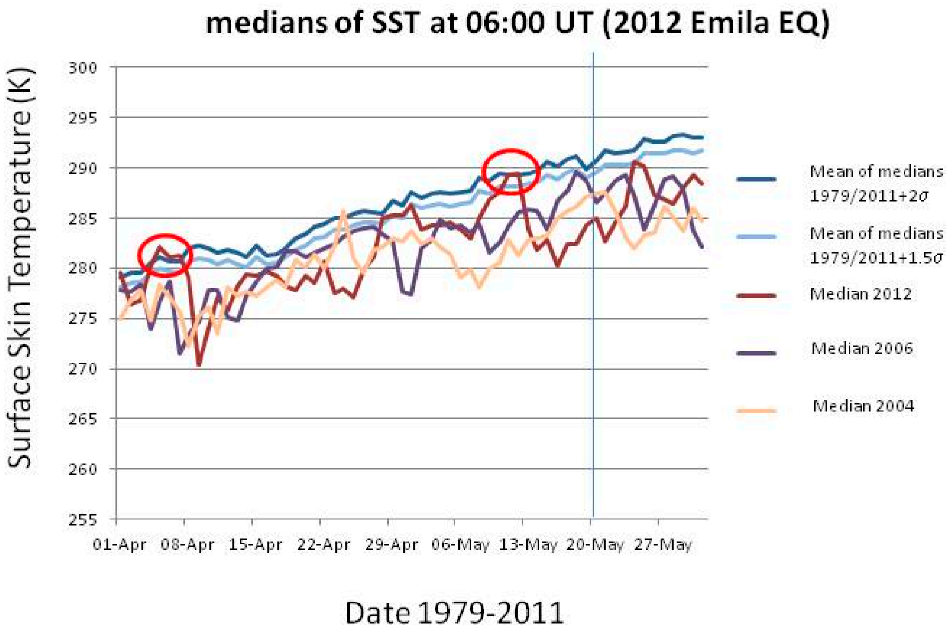

Figure 11. Median behavior of 2012 from 1 April to 31 May, compared with all 1979–2011 medians, and particular comparison with 2004 and 2006 medians. All values have been estimated at the epicenter. The red ovals indicate when the thermal anomaly in 2012 is larger than or equal to 2 standard deviations, σ (as computed from the previous 1979–2012 years) and persists for at least two days. The vertical line is the EQ occurrence.

Table 3. Confusion matrix for pre-earthquake anomaly detection obtained from skt time series analysis from 1994 to 2016 in Central Italy (adapted from [35]).

Skin Temperature Anomaly	Seismicity	
	Yes	No
Yes	2	3
No	3	15

12. Mutual Information and Transfer Information: A Possible Future Direction

Geosystemics focuses on the inter-relations among the components composing the terrestrial complex system. For this reason, every statistical (or physical) quantity that measures these inter-relations is useful. However, given that the system under study is not usually linear, instead of linear quantities such as correlation coefficient or cross-correlation function between two variables belonging to linear processes, we have to resort to statistical quantities, which are more appropriate for nonlinear processes, as typical in a complex system.

Given two variables or time series X and Y, which characterize two processes of the phenomenon under study, we define the mutual information I(X, Y) extending definition (1) to two variables, i.e.,

$$I(X;Y) = \sum_{y\in Y}\sum_{x\in X} p(x,y)\cdot\log\left(\frac{p(x,y)}{p_1(x)p_2(y)}\right) \tag{13}$$

where $p_1(x)$ and $p_2(y)$ are the corresponding probabilities and p(x,y) is the joint probability.

However, this formulation does not provide hints about the direction of information transfer between process X and process Y, i.e., from a part of a system to another. For this purpose, it is possible to introduce a useful definition that quantifies the information flow in terms of the Kullback and Leibler entropy [139], which can be defined for a single process X as:

$$K_x = \sum_x p(x) \cdot \log[p(x)/q(x)]. \tag{14}$$

The above quantity is the entropy related to the process X when a different probability $q(x)$ is used instead of the true $p(x)$. We can also consider two different processes or variables and adapt the Equation (14) using conditional probabilities and taking into account a proper delay in one (see [31]). This gives rise to the so-called transfer information (changing its sign it becomes the transfer entropy) which provides knowledge not only about the information exchange but also about the direction of the information flow.

Here, we do not describe more details but we just want to emphasize the importance of quantifying direction of information flow amongst different parts or processes of the system under study. Often it is more important to know where the flow of information is going, instead of just estimating the information that is exchanged by the whole process between internal components or external ones [140].

Applying this concept to two different time series can be useful to say if one is the master quantity (that represents the causal process) and the other the affected one. [141] gave a very recent example of an application of this concept to geomagnetic field and climate.

In all cases, where we would like to compare/correlate a seismic sequence with possible atmospheric or ionospheric series of precursors, the calculation of the transfer information would provide a robust answer.

13. Conclusions

This paper has introduced the concepts of geosystemics [1,2,21] and then has shown its applications to some case studies. The spirit of geosystemics is to use some universal tools to look at some macroscopic quantities, such as the entropy, the Benioff strain, or the temperature to consequently deduce macroscopic properties of the physical system under study. An important frame is that of dynamical systems approaching a critical point when the macroscopic properties of the system change dramatically. This could be the case of a sequence of EQs that culminates with a main-shock. Therefore, we have shown some results obtained with the study of two recent Italian seismic sequences, the 2009 L'Aquila and the 2012 Emilia sequences.

It is obvious that being the study of EQs a very complex problem, the more characterizing parameters are analyzed, the more robust the result will be. [67], for the case of the 2009 L'Aquila seismic sequence, gave a recent and extensive example of this approach.

A further question is how we can use the Big Data in geosciences and, in particular, to analyze precursory patterns of big earthquakes. Of course, the analysis of a greater number of data and the check of multiple models is perceptible that allows us to find some type of pattern before an earthquake, that could be likely valid only for regions very localized. An extensive statistical big data analysis would be important to confirm or confute the individual case results (although no definitive conclusions can be arisen because high correlation does not always mean causation; however can be of great help in proposing a physical framework of the chain of processes that could occur before a large earthquake). [35] gave an example of this approach, where the validity of local climatological variations as possible seismic precursors in Central Italy was statistically established.

Finally, we hope that this investigation can contribute to the worldwide scientific debate and efforts in understanding the earthquake preparation phase in order to arm the scientific community and stakeholders, against the natural disasters.

Author Contributions: Conceptualization, A.D.S. and L.P.; Data curation, G.C.; Formal analysis, G.C., D.M., L.M. and A.P.; Funding acquisition, A.D.S., C.A. and G.D.F.; Investigation, A.D.S., S.A.C., M.L.R. and L.S.; Methodology, A.D.S. and G.C.; Project administration, C.A., L.A. (Leonardo Amoruso) and M.C.; Resources, G.C.; Software, G.C., A.D.S., D.M., A.P. and F.S.; Supervision, A.D.S., R.D.G. and L.P.; Visualization, L.M. and M.S.; Writing—original draft, A.D.S.; Writing—review and editing, A.D.S., C.A., L.A., L.A. (Leonardo Amoruso), S.A.C., M.C., C.C., G.C., G.D.F., A.D.S. (Anna De Santis), R.D.G., D.M., L.M., L.P., A.P., M.L.R., M.S., L.S. and F.S.

Funding: The authors thank ESA (European Space Agency) for funding the SAFE (Swarm for Earthquake study; safe-swarm.ingv.it) project under STSE Swarm+Innovation Programme, ASI (Italian Space Agency) for funding LIMADOU-Science project, and INGV (Istituto Nazionale di Geofisica e Vulcanologia) for funding LAIC-U (Lithosphere-Atmosphere-Ionosphere Coupling Understanding) and ECHO (Entropy and CHaOs: tools for studying and characterizing seismic sequences evolution) Projects, under which much work was undertaken for preparing this work.

Conflicts of Interest: We declare that there are no conflicts of interest.

References

1. Nott, J. *Extreme Events: A Physical Reconstruction and Risk Assessment*; Cambridge University Press: Cambridge, UK, 2006; p. 297.
2. Meyers, R.A. *Extreme Environmental Events*; Springer: New York, NY, USA, 2009; p. 1250.
3. Peduzzi, P. Is climate change increasing the frequency of hazardous events? *Environ. Poverty Times* **2005**, *3*, 7.
4. Bunde, A.; Kropp, J.; Schellnhuber, H.J. *The Science of Disasters. Climate Disruptions, Heart Attacks, and Market Crashes*; Springer: Berlin, Germany, 2002.
5. Skinner, B.J.; Porter, S.C. *The Blue Planet: An Introduction to Earth System Science*; Wiley VCH: New York, NY, USA, 1995.
6. De Santis, A. Geosystemics. In Proceedings of the 3rd IASME/WSEAS International Conference on Geology and Seismology (GES'09), Cambridge, UK, 21–26 February 2009; pp. 36–40.
7. De Santis, A. Geosystemics, Entropy and Criticality of Earthquakes: A Vision of Our Planet and a Key of Access. In *Addressing Global Environmental Security through Innovative Educational Curricula*; Springer Nature: Basingstoke, UK, 2014; pp. 3–20.
8. Lovelock, J. Gaia as seen through the atmosphere. *Atmos. Environ. (1967)* **1972**, *6*, 579–580. [CrossRef]
9. Aki, K.; Richards, P. *Quantitative Seismology*, 2nd ed.; University Science Books: Sausalito, CA, USA, 2002; p. 700.
10. Bizzarri, A. On the deterministic description of earthquakes. *Rev. Geophys.* **2011**, *49*, 1–32. [CrossRef]
11. Bizzarri, A. Rupture speed and slip velocity: What can we learn from simulated earthquakes? *Earth Planet. Sci. Lett.* **2012**, *317–318*, 196–203. [CrossRef]
12. Scholz, C.H. *The Mechanics of Earthquake and Faulting, Vol. xxiv*; Cambridge University Press: Cambridge, UK; New York, NY, USA, 2002; 471p.
13. Kanamori, H. The nature of seismicity patterns before large earthquakes. In *Earthquake Prediction*; Simpson, D.W., Richards, P.G., Eds.; American Geophysical Union: Washington, DC, USA, 1981.
14. Baskoutas, I.; Papadopoulos, G.A. Precursory seismicity pattern before strong earthquakes in Greece. *Res. Geophys.* **2014**, *4*, 7–11. [CrossRef]
15. Bizzarri, A. The mechanics of seismic faulting: Recent advances and open issues. *La Riv. Del Nuovo Cim.* **2014**, *37*, 181–271.
16. Dobrovolsky, I.P.; Zubkov, S.I.; Miachin, V.I. Estimation of the size of Earthquake preparation zones. *Pure Appl. Geophys.* **1979**, *117*, 1025–1044. [CrossRef]
17. Dobrovolsky, I.; Gershenzon, N.; Gokhberg, M. Theory of electrokinetic effects occurring at the final stage in the preparation of a tectonic earthquake. *Phys. Earth Planet. Inter.* **1989**, *57*, 144–156. [CrossRef]
18. Sobolev, G.A.; Huang, Q.; Nagao, T. Phases of earthquake's preparation and by chance test of seismic quiescence anomaly. *J. Geodyn.* **2002**, *33*, 413–424. [CrossRef]
19. Cicerone, R.D.; Ebel, J.E.; Britton, J. A systematic compilation of earthquake precursors. *Tectonophysics* **2009**, *476*, 371–396. [CrossRef]
20. De Santis, A.; De Franceschi, G.; Spogli, L.; Perrone, L.; Alfonsi, L.; Qamili, E.; Cianchini, G.; di Giovambattista, R.; Salvi, S.; Filippi, E.; et al. Geospace perturbations induced by the Earth: The state of the art and future trends. *Phys. Chem. Earth* **2015**, *85–86*, 17–33. [CrossRef]
21. De Santis, A.; Qamili, E. Geosystemics: A systemic view of the Earth's magnetic field and possibilities for an imminent geomagnetic transition. *Pure Appl. Geophys.* **2015**, *172*, 75–89. [CrossRef]
22. Bekenstein, J.D. Information in the Holographic Universe. *Sci. Am.* **2003**, *289*, 61. [CrossRef]

23. Chuvieco, E.; Huete, A. *Fundamentals of Satellite Remote Sensing*; CRC Press: Boca Raton, FL, USA, 2009; p. 448.
24. Favali, P.; Beranzoli, L.; De Santis, A. *Seafloor Observatories: A New Vision of the Earth from the Abyss*; Springer—Praxis Publishing: New York, NY, USA, 2015; pp. 1–2.
25. Schneider, S.; Boston, P. *The Gaia Hypothesis and Earth System Science*; University of Florida: MIT Press: Cambridge, MA, USA, 1992.
26. Jacobson, M.; Charlson, R.J.; Rodhe, H.; Orians, G.H. (Eds.) *Earth System Science, From Biogeochemical Cycles to Global Changes*, 2nd ed.; Elsevier Academic Press: London, UK, 2000.
27. Butz, S.D. *Science of Earth Systems*; Thomson Learning: Boston, MA, USA, 2004.
28. Grandy, W.T., Jr. *Entropy and the Time Evolution of Macroscopic Systems*; Oxford University Press: Oxford, UK, 2008.
29. Kleidon, A. *Thermodynamic Foundation of the Earth System*; Cambridge University Press: Cambridge, UK, 2016.
30. Shannon, C.E. A mathematical theory of communication. *Bell Syst. Tech. J.* **1948**, *27*, 379–423. [CrossRef]
31. Schreiber, T. Measuring Information Transfer. *Phys. Rev. Lett.* **2000**, *85*, 461–464. [CrossRef]
32. Hough, S. *Predicting the Unpredictable: The Tumultuous Science of Earthquake Prediction*; Princeton University Press: Princeton, NJ, USA, 2009.
33. Collaboratory for the Study of Earthquake Predictability. Available online: http://www.cseptesting.org/ (accessed on 20 March 2019).
34. Corssa: The Community Online Resource for Statistical Seismicity Analysis. Available online: http://www.corssa.org (accessed on 20 March 2019).
35. Piscini, A.; De Santis, A.; Marchetti, D.; Cianchini, G. A multi-parametric climatological approach to study the 2016 Amatrice-Norcia (Central Italy) earthquake preparatory phase. *Pure Appl. Geophys.* **2017**, *174*, 3673. [CrossRef]
36. Perrone, L.; De Santis, A.; Abbattista, C.; Alfonsi, L.; Amoruso, L.; Carbone, M.; Cesaroni, C.; Cianchini, G.; De Franceschi, G.; De Santis, A.; et al. Ionospheric anomalies detected by ionosonde and possibly related to crustal earthquakes in Greece. *Ann. Geophys.* **2018**, *36*, 361–371. [CrossRef]
37. Mignan, A. The Stress Accumulation Model: Accelerating Moment Release and Seismic Hazard. *Adv. Geophys.* **2008**, *49*, 67–201.
38. De Santis, A.; Cianchini, G.; Di Giovambattista, R. Accelerating moment release revisited: Examples of application to Italian seismic sequences. *Tectonophysics* **2015**, *639*, 82–98. [CrossRef]
39. Keilis-Borok, V.I.; Kossobokov, V.G. Premonitory activation of earthquake flow: Algorithm M8. *Phys. Earth Planet. Inter.* **1990**, *61*, 73–83. [CrossRef]
40. Kossobokov, V.G. Earthquake prediction: 20 years of global experiment. *Nat. Hazards* **2013**, *69*, 1155–1177. [CrossRef]
41. Shebalin, P.; Keilis-Borok, V.; Gabrielov, A.; Zaliapin, I.; Turcotte, D. Short-term earthquake prediction by reverse analysis of lithosphere dynamics. *Tectonophysics* **2006**, *413*, 63–75. [CrossRef]
42. Zoller, G.; Hainzl, S. A systematic spatiotemporal test of the critical point hypothesis for large earthquakes. *Geophys. Res. Lett.* **2002**, *29*, 1558. [CrossRef]
43. Tyupkin, Y.S.; Di Giovambattista, R. Correlation length as an indicator of critical point behavior prior to a large earthquake. *Earth Planet. Sci. Lett.* **2005**, *230*, 85–96. [CrossRef]
44. Gabrielov, A.; Keilis-Borok, V.; Zaliapin, I.; Newman, W.I. Critical transitions in colliding cascades. *Phys. Rev. E* **2000**, *62*, 237–249. [CrossRef]
45. Zechar, J.D.; Zhuang, J. Risk and return: Evaluating RTP earthquake predictions. *Geophys. J. Int.* **2010**, *182*, 1319–1326. [CrossRef]
46. Molchan, G.; Romashkova, L. Gambling score in earthquake prediction analysis. *Geophys. J. Int.* **2011**, *184*, 1445–1454. [CrossRef]
47. Rundle, J.B.; Tiampo, K.F.; Klein, W.; Martins, J.S.S. Self-organization in leaky threshold systems: The influence of near mean field dynamics and its implications for earthquakes, neurobiology and forecasting. *Proc. Natl. Acad. Sci. USA* **2002**, *99*, 2514–2521. [CrossRef]
48. Nanjo, K.Z.; Rundle, J.B.; Holliday, J.R.; Turcotte, D.L. Pattern Informatics and its application for optimal forecasting of large earthquakes in Japan. *Pure Appl. Geophys.* **2005**, *163*, 2417–2432. [CrossRef]
49. Tiampo, K.; Rundle, J.; Klein, W.; Tiampo, K. Premonitory seismicity changes prior to the Parkfield and Coalinga earthquakes in southern California. *Tectonophysics* **2006**, *413*, 77–86. [CrossRef]
50. Dieterich, J.H. A constitutive law for rate of earthquake production and its application to earthquake clustering. *J. Geophys. Res.* **1994**, *99*, 2601–2618. [CrossRef]

51. Holliday, J.R.; Chen, C.-C.; Tiampo, K.F.; Rundle, J.B.; Turcotte, D.L.; Donnelan, A. A RELM earthquake forecast based on pattern informatics. *Seismol. Res. Lett.* **2007**, *78*, 87–93. [CrossRef]
52. Beck, C.; Schlögl, F. *Thermodynamics of Chaotic Systems*; Cambridge University Press: Cambridge, UK, 1993; p. 306.
53. Gutenberg, B.; Richter, C.F. Frequency of earthquakes in California. *Bull. Seism. Soc. Am.* **1944**, *34*, 185–188.
54. Scholz, C.H. The frequency-magnitude relation of microfracturing in rock and its relation to earthquakes. *Bull. Seismol. Soc. Am.* **1968**, *58*, 399–415.
55. Schorlemmer, D.; Wiemer, S.; Wyss, M. Variations in earthquake-size distribution across different stress regimes. *Nature* **2005**, *437*, 539–542. [CrossRef]
56. Aki, K. Maximum likelihood estimate of b in the formula log(N) = a − bM and its confidence limits. *Bull. Earthq. Res. Inst. Tokyo Univ.* **1965**, *43*, 237–239.
57. Utsu, T. Estimation of parameter values in the formula for the magnitude-frequency relation of earthquake occurrence. *Zisin* **1978**, *31*, 367–382. [CrossRef]
58. De Santis, A.; Cianchini, G.; Favali, P.; Beranzoli, L.; Boschi, E. The Gutenberg-Richter Law and Entropy of Earthquakes: Two Case Studies in Central Italy. *Bull. Seism. Soc. Am.* **2011**, *101*, 1386–1395. [CrossRef]
59. Ihara, S. *Information Theory for Continuous Systems*; World Scientific Pub Co Pte Ltd.: Singapore, 1993.
60. Klir, G.J. *Uncertainty and Information. Foundations of Generalized Information Theory*; J Wiley and Sons, Inc.: Hoboken, NJ, USA, 2006; p. 499.
61. Sugan, M.; Kato, A.; Miyake, H.; Nakagawa, S.; Vuan, A. The preparatory phase of the 2009 M_W 6.3 L'Aquila earthquake by improving the detection capability of low-magnitude foreshocks. *Geophys. Res. Lett.* **2014**, *41*, 6137–6144. [CrossRef]
62. Gulia, L.; Tormann, T.; Wiemer, S.; Herrmann, M.; Seif, S. Short-term probabilistic earthquake risk assessment considering time-dependentbvalues. *Geophys. Res. Lett.* **2016**, *43*, 1100–1108. [CrossRef]
63. Takens, F. Detecting Strange Attractors in Turbulence. In *Dynamical Systems and Turbulence, Warwick 1980*; Springer: Berlin, Germany, 1981; Lecture Notes in Mathematics; Volume 898, ISBN 978-3-540-11171-9.
64. De Santis, A.; Qamili, E.; Cianchini, G. Ergodicity of the recent geomagnetic field. *Phys. Earth Planet. Inter.* **2011**, *186*, 103–110. [CrossRef]
65. Stanley, H.E. *Introduction to Phase Transitions and Critical Phenomena*; Oxford University Press: New York, NY, USA, 1971.
66. Sarlis, N.V.; Skordas, E.S.; Varotsos, P.A.; Nagao, T.; Kamogawa, M.; Tanaka, H.; Uyeda, S. Seismicity order parameter fluctuations in Japan. *Proc. Natl. Acad. Sci. USA* **2013**, *110*, 13734–13738. [CrossRef]
67. Wu, L.X.; Zheng, S.; De Santis, A.; Qin, K.; Di Mauro, R.; Liu, S.J.; Rainone, M.L. Geosphere Coupling and Hydrothermal Anomalies before the 2009 Mw 6.3 2 L'Aquila Earthquake in Italy. *Nat. Hazards Earth Syst. Sci.* **2016**, *16*, 1859–1880. [CrossRef]
68. Varotsos, P.; Sarlis, N.; Skordas, E.; Lazaridou, M.; Varotsos, P.; Sarlis, N.; Skordas, E. Seismic Electric Signals: An additional fact showing their physical interconnection with seismicity. *Tectonophysics* **2013**, *589*, 116–125. [CrossRef]
69. Sarlis, N.V.; Skordas, E.S.; Varotsos, P.A. A remarkable change of the entropy of seismicity in natural time under time reversal before the super-giant M9 Tohoku earthquake on 11 March 2011. *EPL* **2018**, *124*, 29001. [CrossRef]
70. Ramirez-Rojas, A.; Flores-Márquez, E.L.; Sarlis, N.V.; Varotsos, P.A. The Complexity Measures Associated with the Fluctuations of the Entropy in Natural Time before the Deadly México M8.2 Earthquake on 7 September 2017. *Entropy* **2018**, *20*, 477. [CrossRef]
71. Benioff, H. Seismic evidence for the fault origin of oceanic deeps. *Geol. Soc. Am. Bull.* **1949**, *60*, 1837. [CrossRef]
72. Reid, H.F. *The Mechanics of the Earthquake, The California Earthquake of April 18, 1906, Report of the State Investigation Commission Vol. 2*; Carnegie Institution of Washington: Washington, DC, USA, 1910.
73. Bufe, C.G.; Varnes, D.J. Predictive modeling of the seismic cycle of the Greater San Francisco Bay Region. *J. Geophys. Res. Phys.* **1993**, *98*, 9871. [CrossRef]
74. Brehm, D.J.; Braile, L.W. Intermediate-term earthquake prediction using the modified time-to-failure method in southern California. *Bull. Seismol. Soc. Am.* **1999**, *89*, 275–293.
75. Hardebeck, J.L.; Felzer, K.R.; Michael, A.J. Improved test results reveal that the accelerating moment release hypothesis is statistically insignificant. *J. Geophys. Res.* **2008**, *113*, B08310. [CrossRef]

76. Vallianatos, F.; Chatzopoulos, G. A Complexity View into the Physics of the Accelerating Seismic Release Hypothesis: Theoretical Principles. *Entropy* **2018**, *20*, 754. [CrossRef]
77. Bowman, D.D.; Sammis, C.G.; Sornette, A.; Sornette, D.; Ouillon, G. An observational test of the critical earthquake concept. *J. Geophys. Res. Phys.* **1998**, *103*, 24359–24372. [CrossRef]
78. Pulinets, S.A.; Boyarchuk, K.A. *Ionospheric Precursors of Earthquakes*; Springer: Berlin, Germany, 2004.
79. Kelley, M.C. *The Earth's Ionosphere. Plasma Physics and Electrodynamics*, 2nd ed.; Elsevier: Amsterdam, The Netherlands, 2009.
80. Jin, S.; Occhipinti, G.; Jin, R. GNSS ionospheric seismology: Recent observation evidences and characteristics. *Earth-Sci. Rev.* **2015**, *147*, 54–64. [CrossRef]
81. Pulinets, S.; Davidenko, D. Ionospheric Precursors of Earthquakes and Global Electric Circuit. *Adv. Space Res.* **2014**, *53*, 709–723. [CrossRef]
82. Row, R.V. Acoustic-gravity waves in the upper atmosphere due to a nuclear detonation and an earthquake. *J. Geophys. Res. Phys.* **1967**, *72*, 1599–1610. [CrossRef]
83. Afraimovich, E.L.; Feng, D.; Kiryushkin, V.V.; Astafyeva, E.I. Near-field TEC response to the main shock of the 2008 Wenchuan earthquake. *Earth Planets Space* **2010**, *62*, 899–904. [CrossRef]
84. GPS Data Show How Nepal Quake Disturbed Earth's Upper Atmosphere. Available online: http://gpsworld.com/gps-data-show-how-nepal-quake-disturbed-earths-upper-atmosphere/(accessed on 20 March 2019).
85. Hobara, Y.; Parrot, M. Ionospheric perturbations linked to a very powerful seismic event. *J. Atmos. Sol.-Terr. Phys.* **2005**, *67*, 677–685. [CrossRef]
86. Liu, J.Y.; Chen, Y.I.; Chuo, Y.J.; Chen, C.S. A statistical investigation of pre-earthquake ionospheric anomaly. *J. Geophys. Res.* **2006**, *111*, A05304. [CrossRef]
87. Dabas, R.; Das, R.M.; Sharma, K.; Pillai, K. Ionospheric pre-cursors observed over low latitudes during some of the recent major earthquakes. *J. Atmos. Sol.-Terr. Phys.* **2007**, *69*, 1813–1824. [CrossRef]
88. Perrone, L.; Korsunova, L.; Mikhailov, A. Ionospheric precursors for crustal earthquakes in Italy. *Ann. Geophys.* **2010**, *28*, 941–950. [CrossRef]
89. Xu, T.; Hu, Y.L.; Wang, F.F.; Chen, Z.; Wu, J. Is there any difference in local time variation in ionospheric F2 layer disturbances between earthquake induced and Q- disturbances events? *Ann. Geophys.* **2015**, *33*, 687–695. [CrossRef]
90. Silina, A.S.; Liperovskaya, E.V.; Liperovsky, V.A.; Meister, C.-V. Ionospheric phenomena before strong earthquakes. *Nat. Hazards Earth Syst. Sci.* **2001**, *1*, 113–118. [CrossRef]
91. Ondoh, T. Anomalous sporadic-E layers observed before M 7.2 Hyogo-ken Nanbu earthquake; Terrestrial gas emanation model. *Adv. Polar Up. Atmos. Res.* **2003**, *17*, 96–108.
92. Ondoh, T.; Hayakawa, M. Synthetic study of precursory phenomena of the M7.2 Hyogo-ken Nanbu earthquake. *Phys. Chem. Earth Parts A/B/C* **2006**, *31*, 378–388. [CrossRef]
93. Fawcett, T. An introduction to ROC analysis. *Pattern Recognit. Lett.* **2006**, *27*, 861–874. [CrossRef]
94. Mancini, F.; Galeandro, A.; De Giglio, M.; Barbarella, M. Ionospheric Activityand possible connection with seismicity: Contribution from the analysis of long time series of GNSS Signals. *Phys. Chem. Earth* **2015**, *85–86*, 106–113. [CrossRef]
95. Contadakis, M.; Arabelos, D.; Vergos, G.; Spatalas, S. TEC Variations over Mediterranean before and during the Strong Earthquake (M = 6.2) of 12th October 2013 in Crete, Greece. *Phys. Chem. Earth* **2015**, *85–86*, 9–16. [CrossRef]
96. Akhoondzadeh, M. Ant Colony Optimization detects anomalous aerosol variations associated with the Chile earthquake of 27 February 2010. *Adv. Res.* **2015**, *55*, 1754–1763. [CrossRef]
97. Kuo, C.-L.; Lee, L.-C.; Heki, K. Preseismic TEC Changes for Tohoku-Oki Earthquake: Comparisons Between Simulations and Observations. *Terr. Atmos. Ocean. Sci.* **2015**, *26*, 63. [CrossRef]
98. Masci, F.; Thomas, J.N.; Villani, F.; Secan, J.A.; Rivera, N. On the onset of ionospheric precursors 40 min before strong earthquakes. *J. Geophys. Res. Phys.* **2015**, *120*, 1383–1393. [CrossRef]
99. Heki, K. Ionospheric electron enhancement preceding the 2011 Tohoku-Oki earthquake. *Geophys. Res. Lett.* **2011**, *38*, 1–5. [CrossRef]
100. Heki, K.; Enomoto, Y. Preseismic ionospheric electron enhancements revisited. *J. Geophys. Res. Phys.* **2013**, *118*, 6618–6626. [CrossRef]

101. Kelley, M.C.; Swartz, W.E.; Heki, K. Apparent ionospheric total electron content variations prior to major earthquakes due to electric fields created by tectonic stresses. *J. Geophys. Res. Phys.* **2017**, *122*, 6689–6695. [CrossRef]
102. Píša, D.; Němec, F.; Santolík, O.; Parrot, M.; Rycroft, M. Additional attenuation of natural VLF electromagnetic waves observed by the DEMETER spacecraft resulting from preseismic activity. *J. Geophys. Res. Phys.* **2013**, *118*, 5286–5295. [CrossRef]
103. Ryu, K.; Lee, E.; Chae, J.S.; Parrot, M.; Oyama, K.-I. Multisatellite observations of an intensified equatorial ionization anomaly in relation to the northern Sumatra earthquake of March 2005. *J. Geophys. Res. Phys. Space Phys.* **2014**, *119*, 4767–4785. [CrossRef]
104. Ryu, K.; Parrot, M.; Kim, S.G.; Jeong, K.S.; Chae, J.S.; Pulinets, S.; Oyama, K.-I. Suspected seismo-ionospheric coupling observed by satellite measurements and GPS TEX related to the M7.9 Wenchuan earthquake of 12 May 2008. *J. Geophys. Res. Phys. Space Phys.* **2014**, *119*, 10305–10323.
105. Yan, R.; Parrot, M.; Pinçon, J.-L. Statistical Study on Variations of the Ionospheric Ion Density Observed by DEMETER and Related to Seismic Activities. *J. Geophys. Res. Phys.* **2017**, 122. [CrossRef]
106. De Santis, A.; Balasis, G.; Pavon-Carrasco, F.J.; Cianchini, G.; Mandea, M. Potential earthquake precursory pattern from space: The 2015 Nepal event as seen by magnetic Swarm satellites. *Earth Planet. Sci. Lett.* **2017**, *461*, 119–126. [CrossRef]
107. Akhoondzadeh, M.; De Santis, A.; Marchetti, D.; Piscini, A.; Cianchini, G. Multi precursors analysis associated with the powerful Ecuador (M_W = 7.8) earthquake of 16 April 2016 using Swarm satellites data in conjunction with other multi-platform satellite and ground data. *Adv. Res.* **2018**, *61*, 248–263. [CrossRef]
108. Marchetti, D.; Akhoondzadeh, M. Analysis of Swarm satellites data showing seismo-ionospheric anomalies around the time of the strong Mexico (Mw = 8.2) earthquake of 08 September 2017. *Adv. Space Res.* **2018**, *62*, 614–623. [CrossRef]
109. Pulinets, S.A.; Ouzounov, D.; Ciraolo, L.; Singh, R.; Cervone, G.; Leyva, A.; Dunajecka, M.; Karelin, A.V.; Boyarchuk, K.A.; Kotsarenko, A. Thermal, atmospheric and ionospheric anomalies around the time of the Colima M7.8 earthquake of 21 January 2003. *Ann. Geophys.* **2006**, *24*, 835–849. [CrossRef]
110. Jing, F.; Shen, X.H.; Kang, C.L.; Xiong, P. Variations of multi-parameter observations in atmosphere related to earthquake. *Nat. Hazards Earth Syst. Sci.* **2013**, *13*, 27–33. [CrossRef]
111. Xie, T.; Weiyu, M. Possible Thermal Brightness Temperature Anomalies Associated with the Lushan (China) MS7.0 Earthquake on 20 April 2013. *Earthq. Sci.* **2015**, *28*, 37–47. [CrossRef]
112. Ouzounov, D.; Pulinets, S.; Hattori, K.; Kafatos, M.; Taylor, P. Atmospheric Signals Associated with Major Earthquakes. A Multi-Sensor Approach, Chapter 9. 2011. no. March: 1–23. Available online: http://hdl.handle.net/2060/20110012856 (accessed on 1 March 2019).
113. Piroddi, L.; Ranieri, G.; Freund, F.; Trogu, A. Geology, tectonics and topography underlined by L'Aquila earthquake TIR precursors. *Geophys. J. Int.* **2014**, *197*, 1532–1536. [CrossRef]
114. Freund, F.T. Pre-earthquake signals: Underlying physical processes. *J. Asian Earth Sci.* **2011**, *41*, 383–400. [CrossRef]
115. Qin, K.; Wu, L.X.; De Santis, A.; Wang, H. Surface latent heat flux anomalies before the Ms 7.1 New Zealand earthquake 2010. *Chin. Sci. Bull.* **2011**, *56*, 3273–3280. [CrossRef]
116. Qin, K.; Wu, L.X.; De Santis, A.; Cianchini, G. Preliminary analysis of surface temperature anomalies that preceded the two major Emilia 2012 earthquakes (Italy). *Ann. Geophys.* **2012**, *55*, 823–828.
117. Martinelli, G.; Solecki, A.T.; Tchorz-Trzeciakiewicz, D.E.; Piekarz, M.; Grudzinska, K.K. Laboratory Measurements on Radon Exposure Effects on Local Environmental Temperature: Implications for Satellite TIR Measurements. *Phys. Chem. EarthParts A/B/C* **2015**. [CrossRef]
118. Pulinets, S.A.; Ouzounov, D.P.; Karelin, A.V.; Davidenko, D.V. Physical bases of the generation of short-term earthquake precursors: A complex model of ionization-induced geophysical processes in the Lithophere-Atmosphere-Ionosphere-Magnetosphere System. *Geomagn. Aeron.* **2015**, *4*, 522–539. [CrossRef]
119. Tramutoli, V. Robust Satellite Techniques (RST) for Natural and Environmental Hazards Monitoring and Mitigation: Theory and Applications. In Proceedings of the 2007 International Workshop on the Analysis of Multi-temporal Remote Sensing Images, Leuven, Belgium, 18–20 July 2007.
120. Tramutoli, V. Using RST approach and EOS-MODIS radiances for monitoring seismically active regions: A study on the 6 April 2009 Abruzzo earthquake. *Nat. Hazards Earth Syst. Sci.* **2010**, *10*, 239–249.

121. Aliano, C.; Corrado, R.; Filizzola, C.; Genzano, N.; Pergola, N.; Tramutoli, V. Robust TIR Satellite Techniques for Monitoring Earthquake Active Regions: Limits, Main Achievements and Perspectives. *Ann. Geophys.* **2008**, *51*, 303–317.
122. Xiong, P.; Shen, X.; Gu, X.; Meng, Q.; Bi, Y.; Zhao, L.; Zhao, Y.; Li, Y.; Dong, J. Satellite detection of IR precursors using bi-angular advanced along-track scanning radiometer data: A case study of Yushu earthquake. *Earthq. Sci.* **2015**, *28*, 25–36. [CrossRef]
123. Hsu, S.C.; Huang, Y.T.; Tu, J.Y.; Huang, J.-C.; Engling, G.; Lin, C.Y.; Lin, F.J.; Huang, C.H. Evaluating real-time air-quality data as earthquake indicator. *Sci. Total Environ.* **2010**, *408*, 2299–2304. [CrossRef] [PubMed]
124. Guangmeng, G.; Jie, Y. Three attempts of earthquake prediction with satellite cloud images. *Nat. Hazards Earth Syst. Sci.* **2013**, *13*, 91–95. [CrossRef]
125. Harrison, R.G.; Aplin, K.L.; Rycroft, M.J. Earthquake-cloud coupling through the global atmospheric electric circuit. *Nat. Hazards Earth Syst. Sci.* **2014**, *14*, 773–777. [CrossRef]
126. Ruzhin, Y.; Nomicos, C. Radio VHF precursors of earthquakes. *Nat. Hazard* **2007**, *40*, 573–583. [CrossRef]
127. Thomas, J.N.; Masci, F.; Love, J.J. On a report that the 2012 M 6.0 earthquake in Italy was predicted after seeing an unusual cloud formation. *Nat. Hazards Earth Syst. Sci.* **2015**, *15*, 1061–1068. [CrossRef]
128. Pulinets, S.A.; Ouzounov, D. Lithosphere–Atmosphere–Ionosphere Coupling (LAIC) model. An unified concept for earthquake precursors validation. *J. Asian Earth Sci.* **2011**, *41*, 371–382. [CrossRef]
129. Yang, S.-S.; Asano, T.; Hayakawa, M. Abnormal gravity wave activity in the stratosphere prior to the 2016 Kumamoto earthquakes. *J. Geophys. Res. Space Phys.* **2019**, *124*.
130. Sorokin, V.; Chmyrev, V.; Yaschenko, A. Electrodynamic model of the lower atmosphere and the ionosphere coupling. *J. Atmos. Sol.-Terr. Phys.* **2001**, *63*, 1681–1691. [CrossRef]
131. Kon, S.; Nishihashi, M.; Hattori, K. Ionospheric anomalies possibly associated with M ≥ 6.0 earthquakes in the Japan area during 1998–2010: Case studies and statistical study. *J. Earth Sci.* **2011**, *41*, 410–420. [CrossRef]
132. Freund, F.T.; Kulahci, I.G.; Cyr, G.; Ling, J.; Winnick, M.; Tregloan-Reed, J.; Freund, M.M. Air ionization at rock surfaces and pre-earthquake signals. *J. Atmos. Sol.-Terr. Phys.* **2009**, *71*, 1824–1834. [CrossRef]
133. Dahlgren, R.P.; Johnston, M.J.S.; Vanderbilt, V.C.; Nakaba, R.N. Comparison of the Stress-Stimulated Current of Dry and Fluid-Saturated Gabbro Samples. *Bull. Seism. Soc. Am.* **2014**, *104*, 2662–2672. [CrossRef]
134. Scoville, J.; Heraud, J.; Freund, F. Pre-Earthquake Magnetic Pulses. *Nat. Hazards Earth Syst. Sci.* **2015**, *15*, 1873–1880. [CrossRef]
135. Kuo, C.L.; Huba, J.D.; Joyce, G.; Lee, L. Ionosphere plasma bubbles and density variations induced by pre-earthquake rock currents and associated surface charges. *J. Geophys. Res.* **2011**, *116*, A10317. [CrossRef]
136. Kuo, C.L.; Lee, L.; Huba, J.D. An improved coupling model for the lithosphere–atmosphere–ionosphere system. *J. Geophys. Res.* **2014**. [CrossRef]
137. Enomoto, Y. Coupled interaction of earthquake nucleation with deep Earth gases: A possible mechanism for seismo-electromagnetic phenomena. *Geophys. J. Int.* **2012**, *191*, 1210–1214. [CrossRef]
138. Piscini, A.; Marchetti, D.; De Santis, A. Multi-parametric climatological analysis associated with global significant volcanic eruptions during 2002–2017. *Pure Appl. Geophys.* **2019**, in press. [CrossRef]
139. Kullback, S.; Leibler, R.A. On information and sufficiency. *Ann. Math. Stat.* **1951**, *22*, 79–86. [CrossRef]
140. Ahlswede, R.; Baumer, L.; Cao, N.; Aydinian, H.; Blinovsky, V.; Deppe, C.; Mashurian, H. (Eds.) *General Theory of Information Transfer and Combinatorics*; Springer: Berlin/Heidelberg, Germany, 2006.
141. Campuzano, S.A.; De Santis, A.; Pavon-Carrasco, F.J.; Osete, M.L.; Qamili, E. New perspectives in the study of the Earth's magnetic field and climate connection: The use of transfer entropy. *PLoS ONE* **2018**, *13*, e0207270. [CrossRef]

ORIGINAL RESEARCH
published: 24 November 2020
doi: 10.3389/feart.2020.540398

A Multiparametric Approach to Study the Preparation Phase of the 2019 M7.1 Ridgecrest (California, United States) Earthquake

Angelo De Santis[1], Gianfranco Cianchini[1], Dedalo Marchetti[1,2], Alessandro Piscini[1], Dario Sabbagh[1], Loredana Perrone[1], Saioa Arquero Campuzano[1†] and Sedat Inan[1†]*

[1]Istituto Nazionale di Geofisica e Vulcanologia, Roma, Italy, [2]School of Remote Sensing and Geomatics Engineering, Nanjing University of Information Science and Technology, Nanjing, China

Edited by:
Giovanni Martinelli,
National Institute of Geophysics and Volcanology, Italy

Reviewed by:
Michael Emmanuel Contadakis,
Aristotle University of Thessaloniki, Greece
Jing Liu,
China Earthquake Administration, China

***Correspondence:**
Angelo De Santis
angelo.desantis@ingv.it

†Present address:
Saioa Arquero Campuzano,
Instituto de Geociencias IGEO (CSIC-UCM), Madrid, Spain
Sedat Inan,
Faculty of Mines, Department of Geological Engineering, Istanbul Technical University, Istanbul, Turkey

Specialty section:
This article was submitted to Solid Earth Geophysics, a section of the journal Frontiers in Earth Science

Received: 04 March 2020
Accepted: 25 September 2020
Published: 24 November 2020

Citation:
De Santis A, Cianchini G, Marchetti D, Piscini A, Sabbagh D, Perrone L, Campuzano SA and Inan S (2020) A Multiparametric Approach to Study the Preparation Phase of the 2019 M7.1 Ridgecrest (California, United States) Earthquake. Front. Earth Sci. 8:540398. doi: 10.3389/feart.2020.540398

The 2019 M7.1 Ridgecrest earthquake was the strongest one in the last 20 years in California (United States). In a multiparametric fashion, we collected data from the lithosphere (seismicity), atmosphere (temperature, water vapor, aerosol, and methane), and ionosphere (ionospheric parameters from ionosonde, electron density, and magnetic field data from satellites). We analyzed the data in order to identify possible anomalies that cannot be explained by the typical physics of each domain of study and can be likely attributed to the lithosphere-atmosphere-ionosphere coupling (LAIC), due to the preparation phase of the Ridgecrest earthquake. The results are encouraging showing a chain of processes that connect the different geolayers before the earthquake, with the cumulative number of foreshocks and of all other (atmospheric and ionospheric) anomalies both accelerating in the same way as the mainshock is approaching.

Keywords: earthquake, lithosphere-atmosphere-ionosphere coupling, multiparametric approach, earthquake precursor anomalies, earthquake preparation process

INTRODUCTION

The 2019 Ridgecrest seismic sequence started on July 4, 2019: many small magnitude events (Ml ~ 0) preceded by 2 h the major earthquake with a 6.4 magnitude (Ross et al., 2019), occurred at 17:33 UTC on 4 July and now considered as the largest foreshock. The sequence of foreshocks continued with numerous events with magnitude from intermediate to large (e.g., an M5.4 about 16 h, and an M5.0 almost 3 min before the mainshock) culminating with the M7.1, which struck on 6 July at 03:19 UTC. This earthquake was the most powerful event occurring in California in the last 20 years (after the M7.1 1999 Hector Mine earthquake, e.g., Rymer et al., 2002). These major shocks occurred north and northeast of the town of Ridgecrest, California (about 200 km north-northeast of Los Angeles). After 21 days, they were followed by more than 111,000 aftershocks (M > 0.5, Ross et al., 2019), mainly within the area of the Naval Air Weapons Station China Lake (California).

Recent works on the Ridgecrest seismic sequence revealed much of the complexity of the seismic source of the major ruptures and relative mechanisms (e.g., Barnhart et al., 2019; Ross et al., 2019; Chen et al., 2020), but nothing was investigated about the preparation phase of the seismic sequence and its possible coupling with the above geolayers, such as the atmosphere and ionosphere. This article intends to fill the gap.

We know how much difficult the study of what happens before a large earthquake is and how controversial the concept of preparation phase of an earthquake is within the scientific community.

Nevertheless, it is rather difficult to think that a so large energetic phenomenon such as a strong earthquake cannot provide any sign of its preparation (e.g., Sobolev et al., 2002; Bulut 2015). With this work, we want to give a fundamental contribution to the study of the preparation phase of earthquakes, considering the case study of the 2019 Ridgecrest seismic sequence.

The idea of an interconnected planet where all its parts interact each other is known as geosystemics (De Santis, 2009; De Santis, 2014) and it is a very interesting concept to apply to the study of earthquakes (De Santis et al., 2019a). This idea suggests that the best way to study Earth's physical phenomena is a multiparametric analysis. This means that, in order to understand how some processes work, we need to analyze different parameters from the area of interest, originating from different sources. In the particular case of earthquakes, the lithosphere-atmosphere-ionosphere coupling (LAIC) proposes a relation between events occurred in lithosphere, atmosphere, and ionosphere that could precede the occurrence of large earthquakes. Therefore, the study of the preparation phase of large earthquakes, as this one in California, can be especially useful to identify possible precursors. There exist different models to explain how these three layers could be linked to each other. A model predicts at fault level the existence of p-holes (positive holes) that, once released at the surface, are able to ionize the atmosphere (Freund, 2011; Freund, 2013) and finally reach the ionosphere. Another model is based on a gas or fluid (such as radon) that can be released by the lithosphere during the preparation phase of earthquake (Pulinets and Ouzounov, 2011; Hayakawa et al., 2018). Both models foresee the creation of a chain of processes that connects the lithosphere to the atmosphere and then to the ionosphere.

In this work, we analyze data from the lithosphere (earthquakes), atmosphere (temperature, water vapor, aerosol, and methane), and ionosphere (e.g., electron density, magnetic field, and other ionospheric parameters) in order to possibly identify the chain of processes preceding the seismic sequence of concern. Limited ground-based observations have been also incorporated. Such an approach demonstrated its powerful capability also in some previous case studies (e.g., Akhoondzadeh et al., 2018; Akhoondzadeh et al., 2019; Marchetti et al., 2019a; Marchetti et al., 2019b; Marchetti et al., 2020), when the view of the earthquake is wider (geosystemic view) and includes all the geolayers involved in the processes (De Santis et al., 2019a; De Santis et al., 2019b).

Being a multiparametric approach, the statistics we applied in this article depends on the parameter and its historical availability (e.g., while atmospheric data have a long history of about 40 years, the satellite data are rather short, about 6 years, so we had to resort to another approach). For the single parameters and their methodology of analysis, we already conducted some statistical validations in our previous works, i.e., skin temperature and total column water vapor analyzed by Climatological Analysis for seismic PRecursor Identification (CAPRI) algorithm have been statistically demonstrated to be successfully related as EQ-precursors in Central Italy in the last 25 years (with 73–74% of overall accuracy; Piscini et al., 2017). The accelerated moment release (AMR) seismic methodology has been successfully validated on 14 medium-large earthquakes (M6.1–M8.3), providing statistical evidence on this set of events that the technique is able to detect a seismic acceleration (Cianchini et al., 2020).

DATA ANALYSES

A seismic characterization of the sequence was conducted by inspecting data collected by the Southern California Earthquake Data Center (SCEDC): we downloaded its catalog from January 1, 2000, to November 13, 2019 (last visit November 14, 2019).

Then, we restricted the events in time (t), depth (z), and magnitude (M) by setting the threshold values to $2000.0 \leq t < 2019.51$ (this latter being the mainshock origin time in decimal year), $z \leq 50$ km and $M \geq 2$, respectively: from now on, this is the complete catalog considered for our analyses. **Figure 1** represents the seismicity of South California as emerged by the imposed limits. The epicenter and the focal mechanism of the M7.1 mainshock are shown. The thick white line shows approximately (more detailed in **Figure 2** by Ross et al., 2019) the projection on the surface of the rupture plane as is depicted by the sequence of the aftershocks. In evidence, a green star shows the strongest foreshock (M6.4), which preceded by almost 34 h the main event, indicated by a red star.

The Ridgecrest sequence occurred in a region with a prevailing NW-SE faulting trend, almost parallel to the more famous San Andreas Fault. The double-couple solution obtained by the U.S. Geological Survey (USGS) indicates that it could have been due to either a right NW-SE or a left NE-SW slip, the former being the more reasonable, if we consider that this fault lays approximately 150 km NE of San Andreas Fault and that the Pacific Plate moves to the NW with respect to the North America Plate (USGS, https://earthquake.usgs.gov/earthquakes/eventpage/ci38457511/executive, last visit January 08, 2020): a confirmation of that is offered by the GPS data analysis conducted by Ross et al. (2019) (please see their Supplementary Figure S13). The "pervasive orthogonal faulting" (Ross et al., 2019) of the area is the origin of a certain degree of geometric complexity: indeed, the largest foreshock was expression of the NE-SW trending fault, orthogonal to that of the M7.1 event.

In the past, around 2002, a former seismic sequence occurred almost in the same area of Ridgecrest, where the recent M7.1 seismic event has been localized (Ross et al., 2019). In order to better analyze the recent Ridgecrest seismicity, we further restricted the time and spatial intervals to those events, which occurred starting from January 1, 2000, confined by a circular area whose radius is 100 km and centered in the epicenter. The obtained catalog of the events in this circular area shows some interesting features: the plot on top of **Figure 2** represents the time-magnitude distribution of the selected events where, in particular, the red color identifies all the events, which fall onto the superficial projection of the fault plane (thick white line in **Figure 1**); on the bottom, the cumulative number of the events is reported: it increments earthquake by earthquake, i.e., as a new earthquake occurs. It is evident that around the first half of 2001, the Ridgecrest fault area was hit by a sequence whose maximum magnitude was a

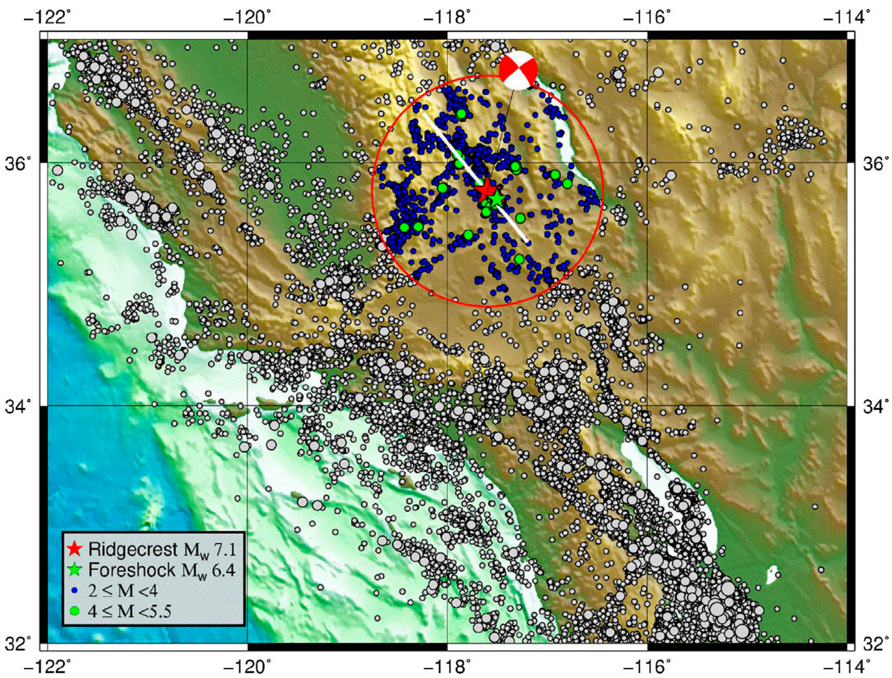

FIGURE 1 | Spatial distribution of earthquake epicenters from 2000 to 2019.5. The thick white line at the central top represents approximately the projection on the surface of the rupture plane, which has been depicted by the aftershocks of the Ridgecrest main event (realized by the GMT Tool). The red circle has a radius of 100 km and is explained in the text. The earthquakes outside the circular areas are presented without colors, but the size corresponds to the range of magnitudes.

bit larger than 5. Although many other events followed this sequence and rarely exceeded magnitude 4, it was only around 2010 that another shorter sequence took place: even in that case, the maximum magnitude did not exceed M4. Please note the steep accumulation of events at the end of the figure. When focusing on approximately the previous month before the mainshock to better inspect the distribution of the earthquakes (**Figure 2**), we can check that no significant event occurred on the fault, except for the earlier 2 days when many earthquakes, several M4+, hit the area, starting from (triggered by) the M6.4 foreshock.

One of the features of the seismic sequences is its accelerating character, i.e., the increase in the rate of earthquake occurrence, which can appear in a region before a large earthquake: this is called AMR, whose physical model promoted by Bowman et al. (1998) is based on the hypothesis that stress changes in the lithosphere lead to an increase in the rate of smaller sized earthquakes before a mainshock. Here, for clarity purpose, we give only the formulation of the quantities involved in the analysis: for a complete discussion of this topic, please refer to De Santis et al. (2015).

To take into account the cumulative effect of a series of N earthquakes at the time t of the last N-th earthquake on a fault, Benioff (1949) introduced the quantity $s(t)$, now called cumulative Benioff strain:

$$s(t) = \sum_i \sqrt{E_i} = \sum_{i=1}^{N(t)} 10^{2.4} 10^{0.75 \cdot M_i}, \tag{1}$$

where the energy in Joule $E_i = (10^{1.5M_i+4.8})$ of the i-th event as a function of its magnitude is involved (De Santis et al., 2015). The AMR can be estimated by looking at the power-law behavior with time of $s(t)$, as given by the following form:

$$s(t) = A + B \cdot \left(t_f - t\right)^m, \tag{2}$$

where $A > 0$, $B < 0$, $t_f > 0$, and $0 < m < 1$ are sequence-dependent "constant" parameters to be determined through a fit to $s(t)$ (**Figure 3**). In theory, t_f would represent the time of failure of the earthquake fault.

A measure of presence for acceleration is the so-called *C-factor* (Bowman et al., 1998) defined as the ratio between the root mean square errors for the power law and the linear fit: when $C < 1$ significantly, then acceleration is meant to be present.

The initial time and the threshold in the minimum magnitude of earthquakes for the AMR analysis are usually a subjective choice: we preferred to be conservative and decided that 5 years of M4+ data were sufficient to detect any possible acceleration in the data. **Figure 3** shows the AMR analysis applied to the events with M4+ occurred in the selected region from 2013.0 to the M7.1 origin time (excluded): blue dots represent the cumulative Benioff strain $s(t)$; the black lines and the red curve are their linear and power-law fits, respectively. We note that the power-law curve fits better data as even *C-factor* confirms, being well below 1 (C = 0.46). However, the most impressive fact is that the acceleration is driven by the rapid sequence of earthquakes happening just after the M6.4 foreshock, i.e., 2 days before the large event, and that

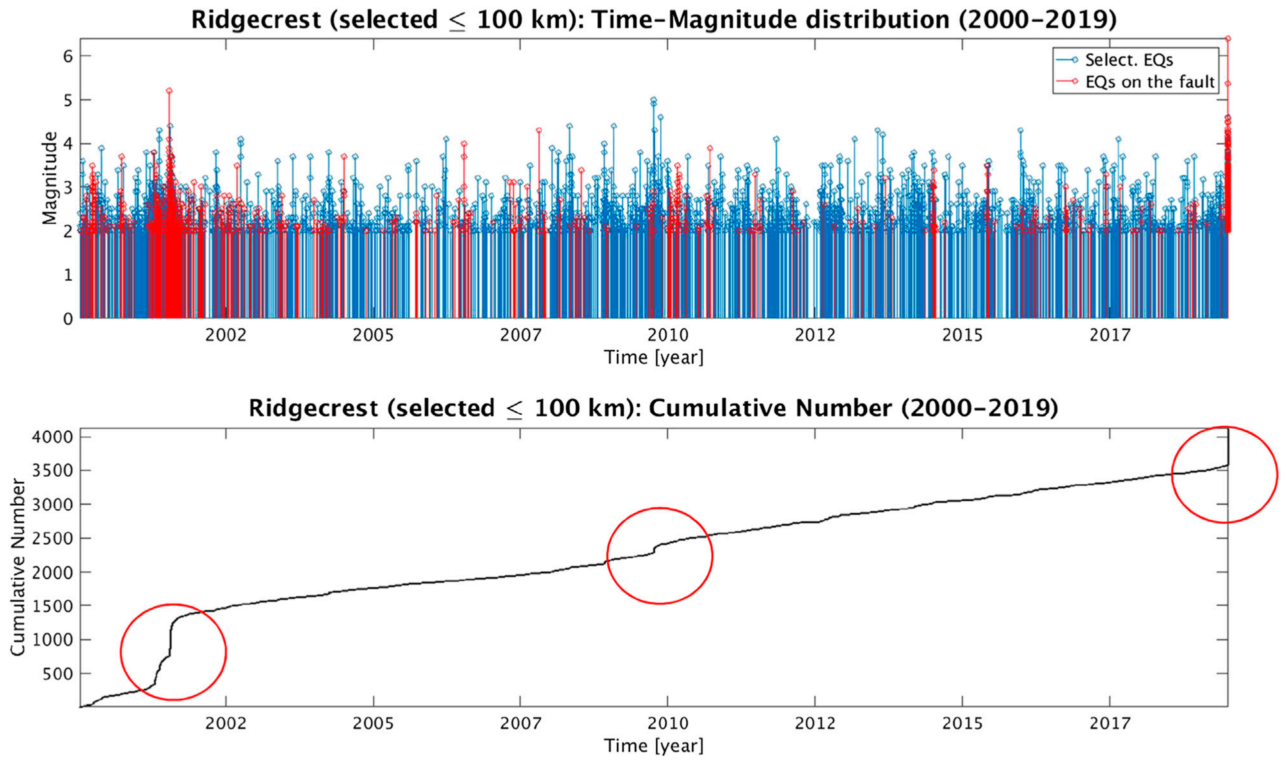

FIGURE 2 | (Top) Time-magnitude distribution of the seismicity in the circular area of 100 km radius around the epicenter of the M7.1 mainshock since January 1, 2000. The earthquakes which are on the fault are indicated with red lines. **(Bottom)** The cumulative number of earthquakes in the same area. At least three sequences can be recognized (as evidenced by red circles): the first, a long lasting one, in 2001, where the largest magnitude exceeded M5; the second, shorter, around the beginning of 2010, whose largest magnitude slightly went beyond M4 and the last concentrated within just 2 days before the 2019 mainshock.

most of the events occurred on the mainshock fault plane, as evidenced by the use of the red color for them.

Atmosphere

Regarding the atmosphere and how it is possibly affected by the preparation phase of the earthquake, we analyze four different parameters, i.e., skin temperature (skt), total column water vapor (tcwv), aerosol optical thickness (AOT), and methane (CH4) concentration, in an adequate region around the mainshock epicenter. Each parameter is taken at some epoch (day, year) as spatial mean of the considered region. In addition to the typical parameters that we already analyzed in previous works, such as skt and tcwv (Piscini et al., 2017) and AOT (Marchetti et al., 2019a; Marchetti et al., 2019b; Piscini et al., 2019), we also considered CH_4 since it seems a potential precursor of seismic activity from recent studies (e.g., Cui et al., 2019).

With regard to the land data, skt and tcwv have been collected from European Centre for Medium-Range Weather Forecasts (ECMWF), the meteorological European center that provides meteo-climatological observations and forecasts. The real time observations are provided in a global model called "operational archive" that is the base for the forecast. The elaboration of the measurements for long-term studies is constantly inserted in another climatological model called "Era-Interim" (ECMWF is now updating to Era-5). The year of interest has been compared to ERA-Interim historical time series. This dataset is a global atmospheric reanalysis project that uses satellite data (European remote sensing satellite, EUMETSAT, and others), input observations prepared for ERA-40, and data from ECMWF's operational archive. Starting from January 1, 1979, it is continuously updated in real time (Dee et al., 2011). The data have been extracted with a spatial resolution of 0.5° corresponding to a resolution of around 50 km.

The AOT has been retrieved from climatological physical-chemical model MERRA-2 (Modern-Era Retrospective Analysis for Research and Applications, version 2, Gelaro et al., 2017) provided by NOAA in the sub-dataset M2T1NXAER version 5.12.4. The data have a spatial resolution of 0.625° longitude and 0.5° latitude and a temporal resolution of 1 h. For this study, the values of skt, tcwv, and AOT closer to the local midnight have been considered to avoid disturbances induced by the daily solar variability. Moreover, the data from 1980 to 2019 have been analyzed, using the data from 1980 to 2018 to construct the historical time series and 2019 to investigate the earthquake preparation phase.

The square area selected for the above three parameters is centered on the mainshock epicenter and the size is selected inside the Dobrovolsky strain radius of $10^{0.43 \cdot M}$ = 1,130 km (Dobrovolsky et al., 1979), which approximates the large-scale

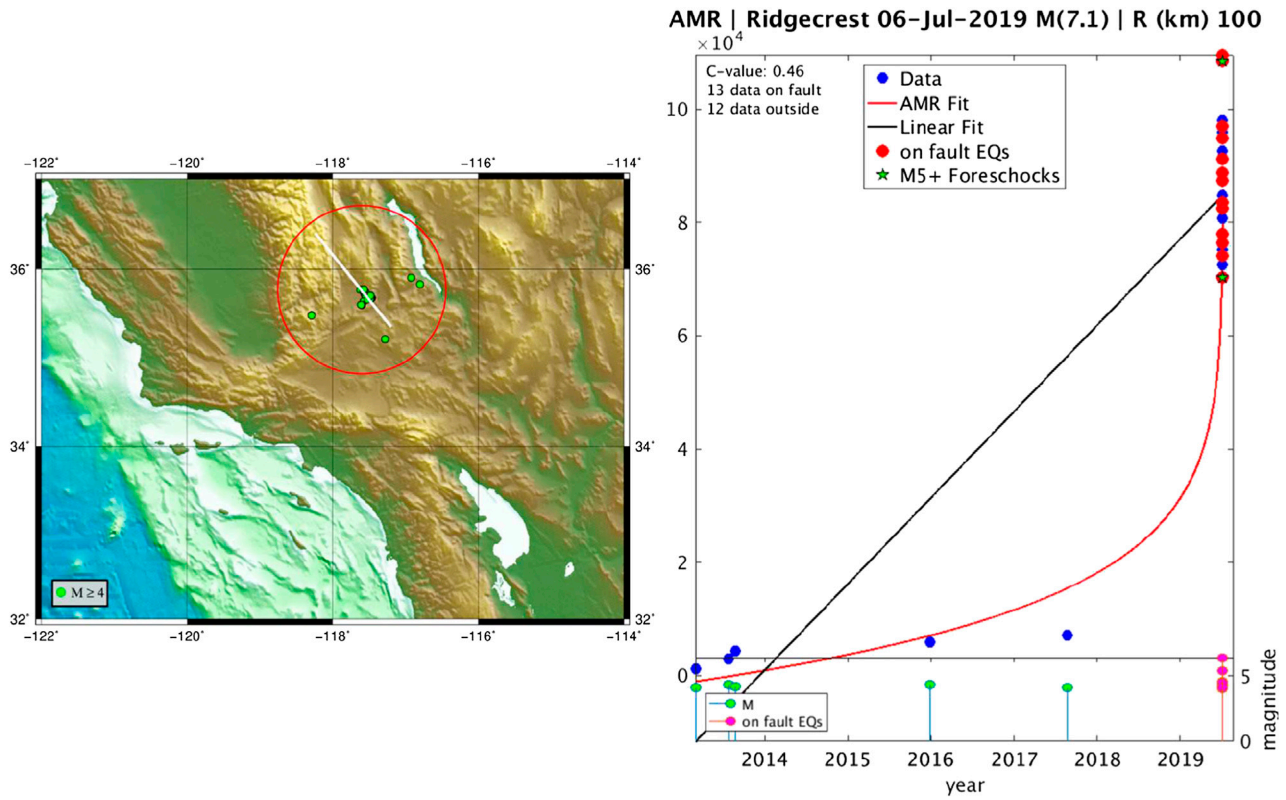

FIGURE 3 | (Left) Geographical map with the M4+ earthquakes, selected since 2013.0 until the mainshock origin time, inside the 100 km radius circle for the accelerated moment release (AMR) analysis. **(Right)** The results of the AMR technique applied together with the temporal sequence of earthquake magnitudes. We notice an acceleration mostly occurring in the few days preceding the mainshock. Two green stars show the largest foreshocks, i.e., the M6.4 and M5.4.

region where seismic precursors are usually expected around the impending faults.

The methane measurements are given as a daily product extracted from atmospheric infrared sounder (AIRS) instrument onboard NASA Earth observation system satellite Aqua provided separately for ascending and descending orbits, so the first one corresponds to daytime (1:30 PM local time at the equator) and the second one to the nighttime (1:30 AM local time at the equator). The satellite was launched into Earth's orbit on May 4, 2002, and it is still in orbit. The instrument is based on a multispectral microwave detector (2,378 channels) that permits to monitor the atmosphere determining the surface temperature, water vapor, cloud, and overall the greenhouse gases concentrations such as ozone, carbon monoxide, carbon dioxide, and methane (Fetzer et al., 2003). In this study, we analyzed the methane volume mixing ratio data (variable CH4_VMR_D) retrieved from level 3 dataset version 6.0.9.0 from 2002 until the 2019 California earthquake only descending orbits, i.e., nighttime at about 1:30 AM. These measurements come directly from the instrument, so differently from investigated data of skt, tcwv, and AOT, the coverage depends on the orbit and so not the whole world is covered for each day. To have some data for every day, we selected an area sufficiently large, but this means to mediate different parts of the same region. For methane data, the area is smaller than the Dobrovolsky area, because it is very sensitive to anthropic activity (e.g., Le Mer and Roger, 2001). In fact, this quantity has been selected in a circle (distance of the center of the pixel from epicenter not greater than 2.0°). As methane is a powerful greenhouse gas, we applied the "global warming" correction (see next paragraph for details).

For all parameters, we essentially applied the method CAPRI or MEANS ("MErra-2 ANalysis to search Seismic precursors" that does not include the "global warming"; see below), already introduced by Piscini et al. (2017) and Piscini et al. (2019) and applied both to seismic and volcanic hazards. These methods compare the present values of the parameter of interest with the corresponding historical time series, i.e., the background, in terms of mean and standard deviation (σ).

The CAPRI algorithm searches for anomalies in the time series of climatological parameters by a statistical analysis. Before being processed, the data are spatially averaged day-by-day selecting those over the land only by applying a land-sea mask because the sea tends to stabilize most of the atmospheric parameters (especially temperature), attenuating all eventual anomalies. Then, the algorithm removes the long-term trend over the whole day-by-day dataset mainly to remove a possible "global warming" effect, which is particularly important in skt and methane. For analogy, we removed the "global warming" effect also to tcwv data, but of course not to AOT because this parameter cannot be affected by a global warming. The data of the time series are averaged over all the years, thus obtaining the average value of a particular day over the past 40 years. Then, to make the comparison feasible, we impose the (operational archive) average value in the period analyzed to coincide with the average of the historical (ERA-Interim) time series, by a simple subtraction. Finally, an anomaly is defined when the present value overcomes the historical mean by two standard deviations. Since with both CAPRI and MEANS approaches there is an uncertainty of 1–2 days in the background, the detected anomaly should also emerge clearly such as a shift by 2–3 days (to be conservative) does not cover the data by the background.

Skin Temperature

This parameter shows three anomalies (**Figure 4**). We exclude the first two (blue circles) because there is not a clear emergence from the historical time series: shifting the peaks by a few days, they could be covered by the typical signal and its variations. On the other hand, the red circle indicates an evident anomaly around 25 days before the mainshock, clearly emerging by more than 2σ the historical time series. In addition, it is also characterized by a two-day persistence. The negative anomaly on around 16 March is not considered because a LAIC model expects only positive increments of temperature due to the earthquake preparation (e.g., Pulinets and Ouzounov, 2011).

Total Column Water Vapor

For the water vapor, we can see one anomaly, which does not clearly emerge from the historical time series (**Figure 5**) and, in addition, it is not persistent. Hence, we consider this anomaly unlikely associated to the earthquake preparation phase.

Aerosol Optical Thickness

AOT is more irregular in time with respect to the two previous parameters. For this reason, we prefer to estimate the mean and standard deviation for a longer time period (6 months instead of 4). The analysis of AOT (**Figure 6**) shows two possible anomalies but only that one around two months before the mainshock looks more reliable: although not persistent, it clearly emerges from the overall background. In this case, the historical time series starts in 1980, because no data are available before this year. MEANS algorithm automatically excluded the 1982 and 2009 datasets because some of their values are particularly anomalous (i.e., greater than 10σ with respect to a preliminary estimation of the historical mean).

Methane

As for AOT, we extended the analysis to 6 months before the mainshock also for methane because it is more irregular than skt and tcwv: **Figure 7** shows the analysis. Please note that the historical time series of CH_4 concentration is computed over a time interval (2002–2018) much shorter than that of the previous climatological quantities (1979–2018 for both historical skt and tcwv time series; 1980–2018 for AOT), because the methane parameter is temporally limited by the AQUA satellite availability. The first apparent CH_4 anomaly (blue circle) is not considered, because there is a close peak (by a few days) in the historical time series, so it could be within 2σ if we shift this point by 2–3 days. The second anomaly, at around 70 days from the mainshock (red circle), is considered significant instead, being clearly emerging from the 2σ band. The negative anomaly on around 15 January is not considered because a reliable LAIC model

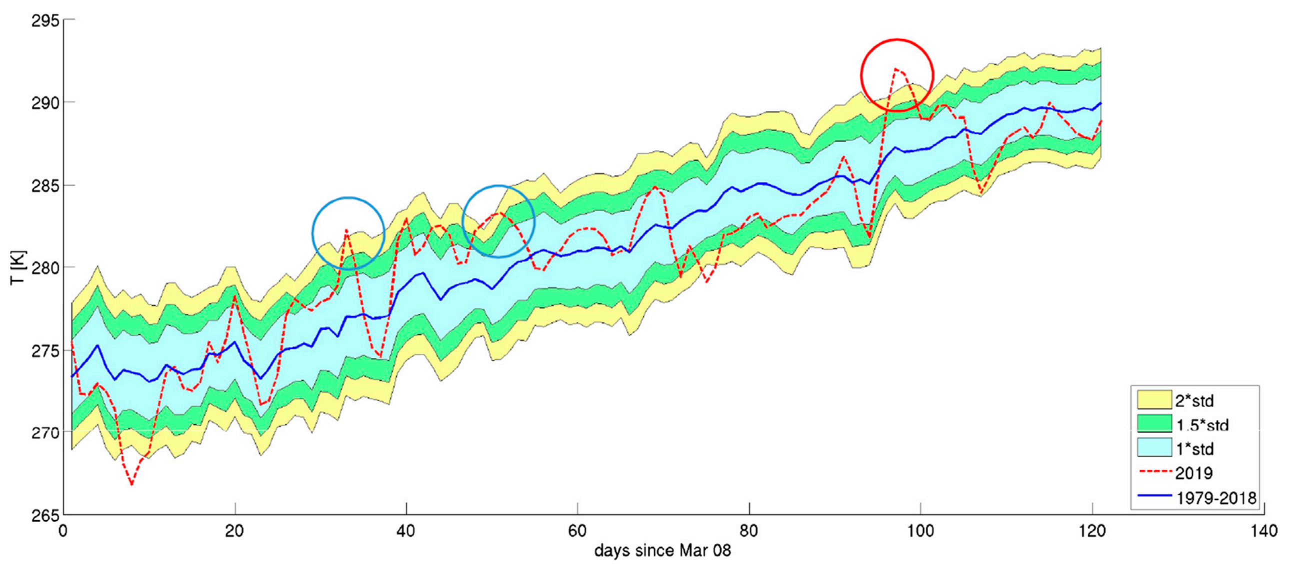

FIGURE 4 | Skin temperature (skt) in the 4 months before the mainshock compared with the historical time series of the previous 40 years. The blue line is the historical mean, while the colored bands present the 1 (light blue), 1.5 (green), and 2 (yellow) standard deviations. Blue circles are anomalies that do not emerge clearly from the 2σ background, while the red circle shows a clear anomaly.

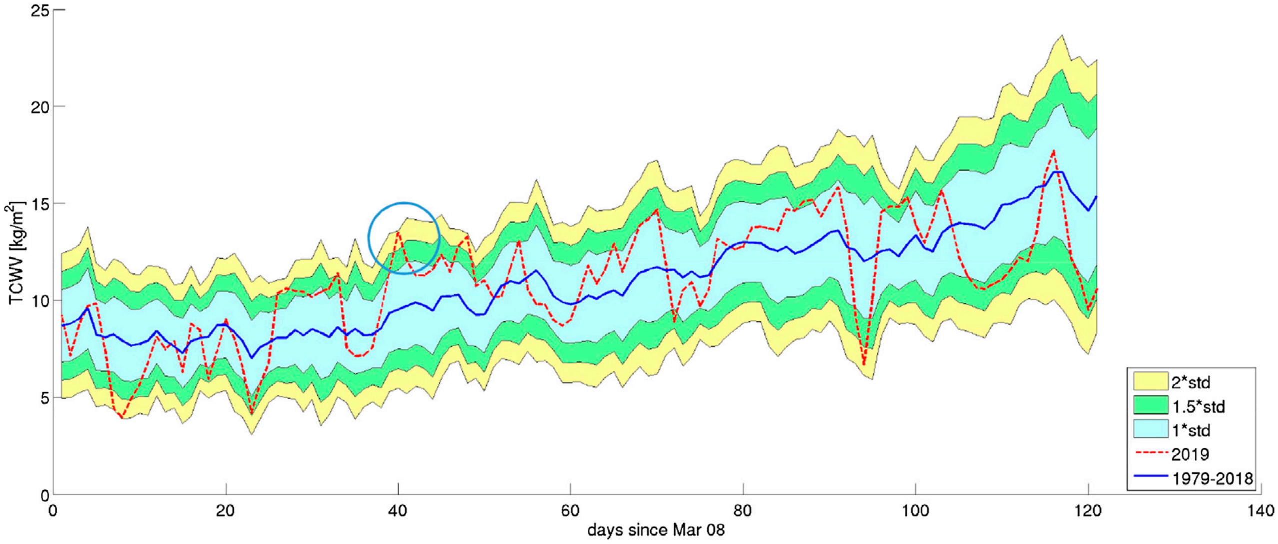

FIGURE 5 | Total column water vapor (tcwv) in the 4 months before the mainshock compared with the historical time series of the previous 40 years. The blue line is the historical mean, while the colored bands present the 1 (light blue), 1.5 (green), and 2 (yellow) standard deviations. The blue circle indicates an anomaly that does not emerge clearly from the 2σ background.

expects a release from underground sources, i.e., a positive increment due to the earthquake preparation.

Ionosphere

Ionosonde

In order to search for possible pre-earthquake ionospheric anomalies, the method proposed by Korsunova and Khegai (2006) and Korsunova and Khegai (2008) and successively developed by Perrone et al. (2010), Perrone et al.(2018), and Ippolito et al. (2020) for ionosonde data was applied here. A peculiar feature of this method is the multi-ionospheric parameter approach, which takes into account the variations of sporadic E (Es) and regular F2 layers occurred simultaneously during magnetically quiet conditions (Perrone et al., 2010; Perrone et al. 2018; Ippolito et al., 2020). The occurrence of the abnormally high Es layer with Δh'Es ≥ 10 km is considered followed by an increase over 20% in f_oEs (maximum frequency of the ionogram trace associated to the Es layer) and over 10% in f_oF2 (critical frequency of the F2 layer) within

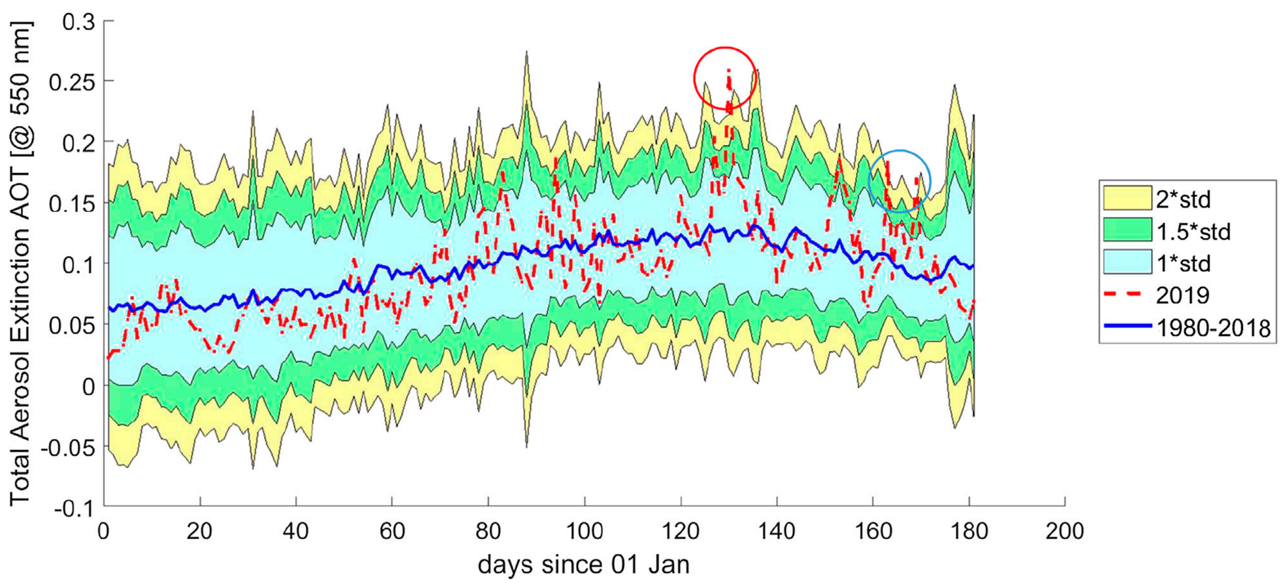

FIGURE 6 | Aerosol optical thickness (AOT) in the 6 months before the mainshock, compared with the historical time series of the previous almost 40 years. The blue line is the historical mean, while the colored bands present the 1 (light blue), 1.5 (green), and 2 (yellow) standard deviations. The blue circle indicates two distinct anomalies that do not emerge clearly from the 2σ background, while the red circle shows a clear anomaly.

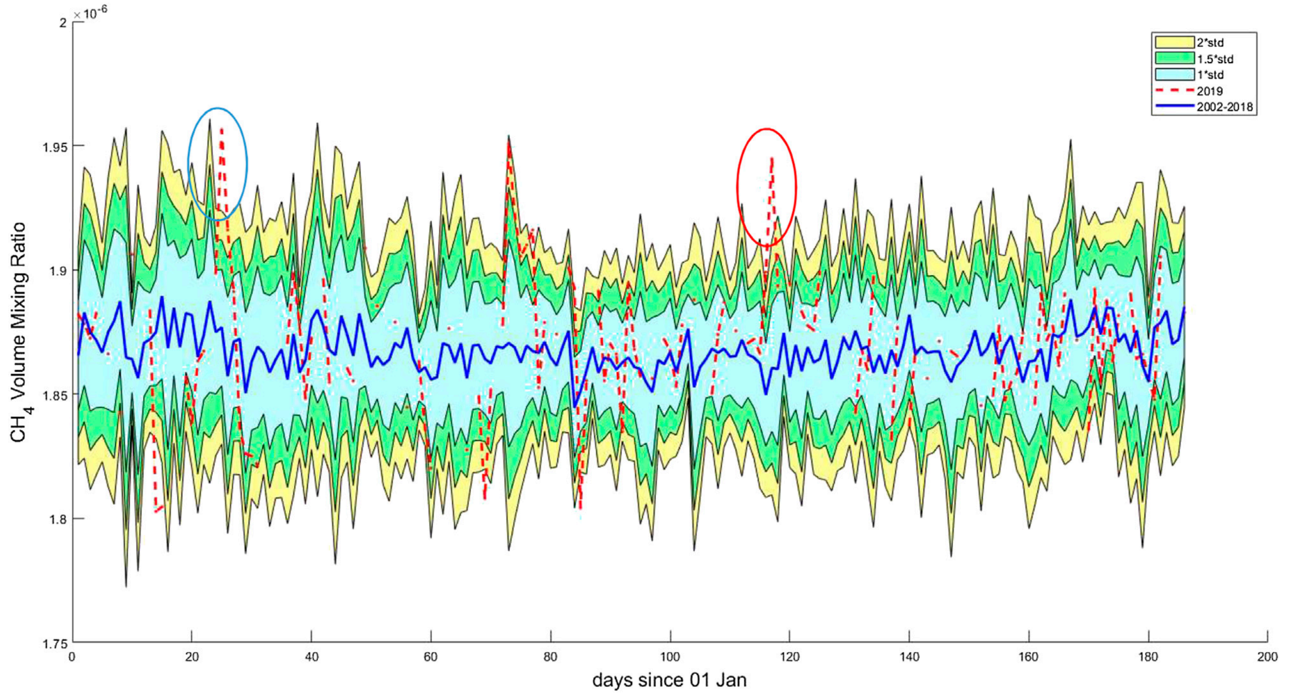

FIGURE 7 | Methane (CH4) concentration in the 6 months before the mainshock compared with the historical time series of the previous almost 20 years. The blue line is the historical mean, while the colored bands present the 1 (light blue), 1.5 (green), and 2 (yellow) standard deviations. The blue circle indicates an anomaly that does not emerge clearly from the 2σ background, while the red circle shows a clear anomaly.

one day for 2–3 h, where the variations are computed w.r.t. 27-days running medians.

Applying the method to the hourly data from the ionosonde of Point Arguello (34.7°N, 239.4°E; distant around 264 km from the epicenter), we recognize a possible pre-earthquake ionospheric anomaly from 22:00 UT on 2 June to 04:00 UT on 3 June (see **Figure 8**), with a significant increasing in f_oF2 at 03:00 UT on 3 June. According to the time of its occurrence, this anomaly anticipates by 5–10 h a magnetic field anomaly found by the Swarm Alpha satellite (see below and **Figure 9**).

Electron Density and Magnetic Field From Satellite

For the electron density (*Ne*), we considered a background based on median values from ionosonde data of hmF2 (peak true height of the F2 layer). The satellite data have been scaled at the F2 altitude by a simple proportion using the International Reference Ionosphere, IRI-2016, model (Bilitza et al., 2017) computed for both altitudes. This background was associated to a geographic cell of 5° longitude and 3° latitude centered in the ionosonde location, used to select the satellite data and compare them with the ionosonde background. For the comparison of *Ne*, we resorted to Swam satellite data. The Swarm mission by ESA is composed of three identical quasi-polar satellites, Alpha, Bravo, and Charlie launched on November 22, 2013, with a multisensor payload: among them, magnetometers and Langmuir probes (Friis-Christensen et al., 2006). Alpha and Charlie fly almost in parallel at around 460 km of altitude, while Bravo flies at around 510 km (in an almost 90° phase orbit in longitude at the epoch of Ridgecrest earthquake). One of the most interesting results was obtained during the comparison of the background *Ne* value of the ionosonde with that measured by the Swarm Alpha satellite (**Figure 9**). During the satellite passage over the same cell of the ground ionosonde on 3 June at 09:14 UT (i.e., around 01 LT), we obtained a relative variation of 1.94, i.e., the *Ne* value measured by the satellite is almost double w.r.t. the background (the latter has been represented in **Figure 9** as a green dashed line extended in latitude for 5° around Pt. Arguello ionosonde location).

Following recent works (e.g., De Santis et al., 2017), a magnetic anomaly from the satellite can be defined from first differences, comparing the root mean square (rms) over a 3°-latitude window with respect to the analogous RMS of the whole satellite track within ±50° geomagnetic latitude. An interesting result is shown in **Figure 9** (in this case rms>2.5 RMS for the window highlighted by red circle). During the same orbit when we detected the *Ne* anomaly, a clear anomaly in Y (East) component of the magnetic field (actually first differences in nT/s are shown) was recorded by the Swarm Alpha satellite on 3 June at 09:14 UT, when the external magnetic field was negligible (magnetic indices Dst = 4 nT and a_p = 2 nT). We notice that the track is almost along the epicenter longitude and the anomaly is located northward in latitude with respect to the epicenter. The anomaly has been recorded in nighttime, and in the same moment, the absolute value of *Ne* was about the double of the typical one (as shown by the green dashed line in **Figure 9**). The anomalous features of the magnetic and plasma measurements of Swarm for this track cannot be

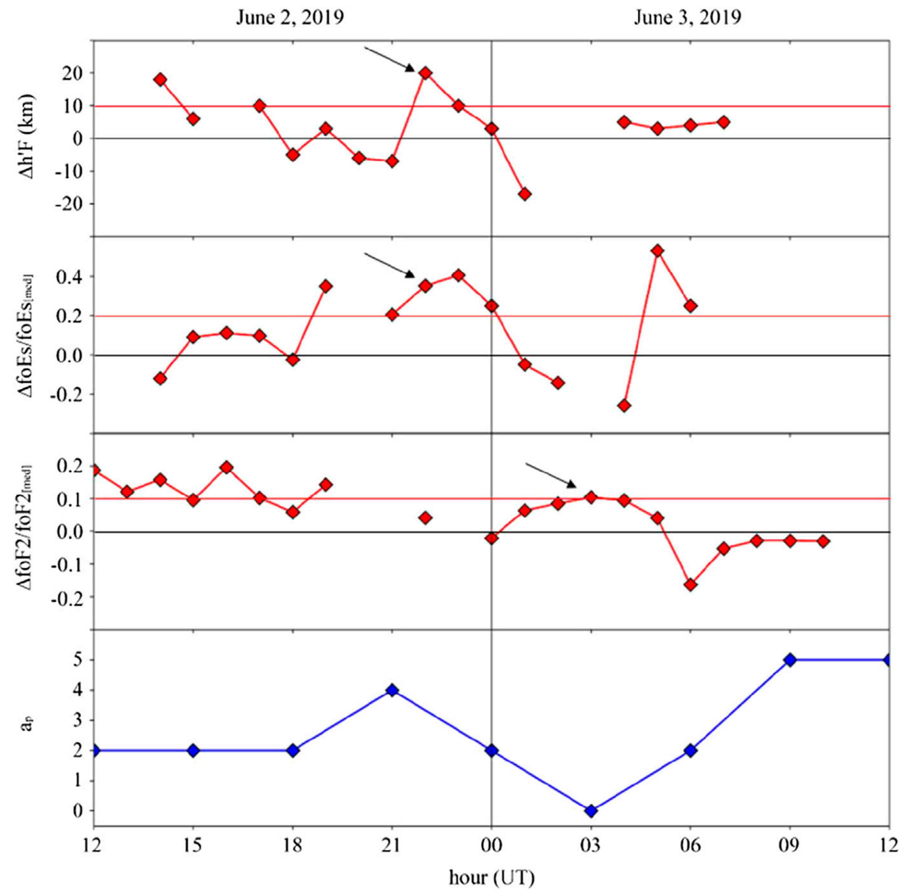

FIGURE 8 | Anomaly taken from ionosonde of Point Arguello (34.7°N, 239.4°E) using observed Δh'Es, δfoEs, and δfoF2 variations (arrows). Three-hour ap geomagnetic index values are given in a lower panel. Black arrows point to possible anomalies.

simply explained by typical ionospheric disturbances. Therefore, we suggest the preparation of the seismic event as a possible source for these phenomena.

As an alternative technique for magnetic field anomaly detection, the residual values, with respect to the recently updated international geomagnetic reference model IGRF-13 (https://www.ngdc.noaa.gov/IAGA/vmod/), have been calculated. Y (East) component of geomagnetic field measured by Swarm Alpha, Bravo, and Charlie satellites has been systematically inspected over the 6 months before the mainshock (this time interval is useful to have sufficiently robust statistics). A three-degree polynomial has been also further subtracted after the removal of the model in order to clean the time series from the seasonal or magnetospheric variations, not predicted by the model.

As in Akhoondzadeh et al. (2018) and Akhoondzadeh et al. (2019), we estimate a median over the 6 months before the mainshock together with the corresponding interquartile (IQR). We then define an anomaly when the residual overcomes the median by more than 1.25 IQR, by at least 1 nT, and the possible effect of the external magnetic fields can be neglected (i.e., the magnetic indices are very low: $|Dst| \leq 20$ nT and $a_p \leq 10$ nT). We prefer to use IQR instead of standard deviation because ionospheric magnetic signals are expected non-Gaussian. However, by analogy, the choice of this threshold would correspond for a Gaussian signal to the largest threshold of 2σ applied in the previous analyses.

Although the threshold is constant for the analyzed 6 months, please note that, before computing it, we removed the daily variation by daily median and the seasonal trend by a polynomial fit. So, after this data processing, the residuals are not anymore affected by daily or seasonal variations.

The disturbed days are automatically excluded from the graph. Three days are particularly anomalous (**Figure 10**): January 31, 2019 (+3.1 nT more than the upper threshold), April 26, 2019 (+2.8 nT above the upper threshold), and June 12, 2019 (−3.3 nT down the lower threshold). Another anomalous day is April 29, 2019 (+1.0 nT).

The same time series analysis has been also applied to the scalar intensity of magnetic field F measured by Swarm (**Figure 11**). The residuals depict some days as clearly anomalous (also here at least 1 nT larger than the adopted threshold): June 3, 2019 (+6.2 nT), June 5, 2019 (−7.3 nT), June 12, 2019 (+1.4 nT), June 16, 2019 (−13.7 nT), June 22,

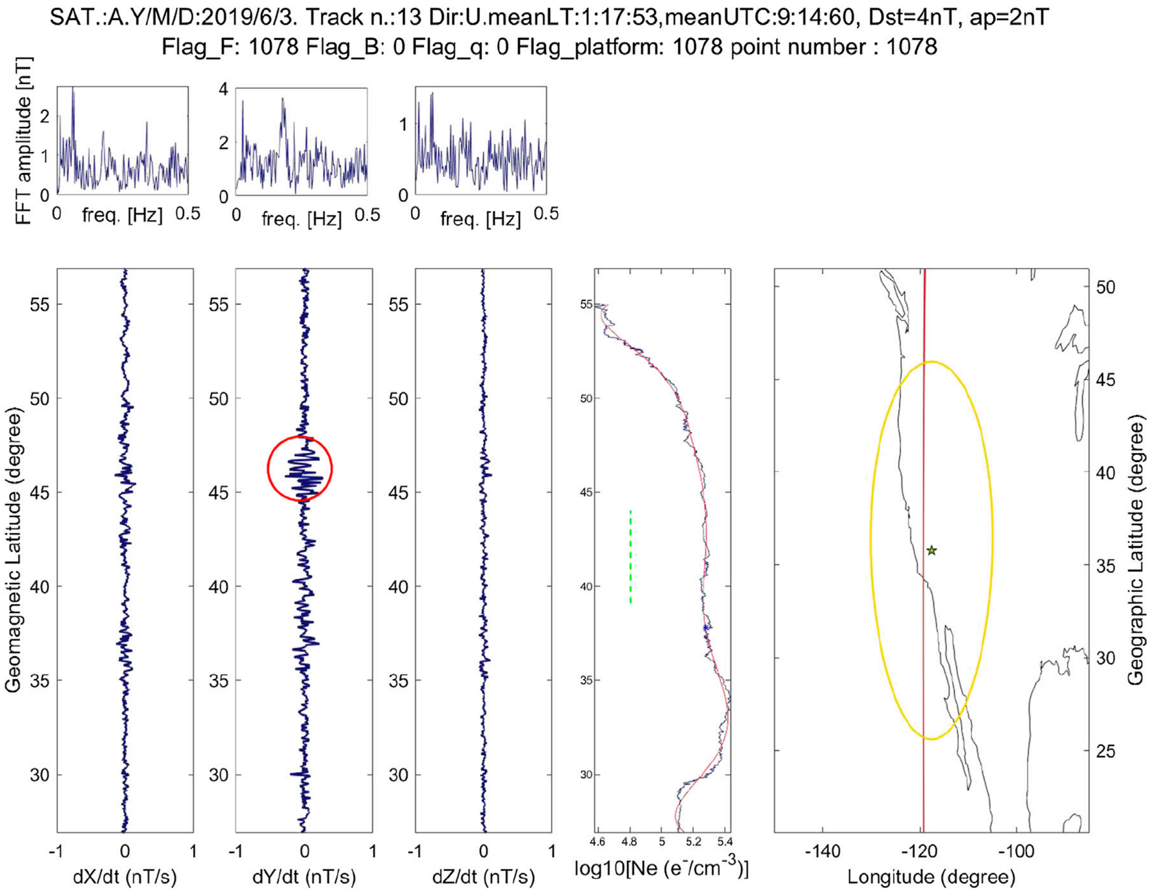

FIGURE 9 | Magnetic anomaly (red circle in Y magnetic field component) taken from the Swarm Alpha satellite on June 3, 2019, at 9:14 UT (around 01 LT). From left, we show plots of dX/dt, dY/dt, and dZ/dt (i.e., the first differences of X, Y, and Z magnetic field components), the logarithm of the electron density Ne along with a green dashed line that is the Ne background level expected from the ionosonde, and finally the geographic map of the region, where the central star represents the earthquake epicenter, the yellow oval is the Dobrovolsky region, and the south-north red line indicated the satellite track projection at the Earth's surface. Top small pictures show the FFT amplitudes for the magnetic components. First line of the heading reports the most important information about the analysis (i.e., type of satellite, date, track number, mean LT and UT, Dst, and ap magnetic indices); second line reports information about the status of satellite data flags that can reveal any problem in the satellite operations or sensor functioning.

2019 (+1.7 nT), June 24, 2019 (−9.1 nT), June 27, 2019 (−8.9 nT), June 30, 2019 (+2.6 nT), and July 3, 2019 (+2.8 nT). We notice that June 12, 2019, is extracted as anomalous by both Y and F analyses. It is interesting to note that in the last period (around one month) approaching the earthquake, the residuals of the magnetic field intensity present more anomalies (highlighted by large red ovals in the figure).

DISCUSSION AND CONCLUSION

Table 1 summarizes the occurrence of all anomalies (dubious anomalies are within a square bracket). It is interesting to highlight that our found precursor times are much longer than those identified by many other papers on earthquake precursors, especially ionospheric precursors, which seem to occur only a few hours to days before large earthquakes (e.g., Heki, 2011; He and Heki, 2017; Yan et al., 2017). Indeed, our recent works highlight a preparation time much longer than few days (e.g., Liu et al., 2020; Marchetti et al., 2019a; Marchetti et al., 2019b). These longer precursor times could be attributed to the long-term process of earthquake preparation (Sugan et al., 2014; Di Giovambattista and Tyupkin, 2004). Moreover, our recent results turned out to be in agreement with the empirical Rikitake (1987) law, recently confirmed for ionospheric precursors from the satellite by De Santis et al. (2019c), which also provide a reasonable physical explanation for the law itself. In accordance to this law, where the precursor time depends on the earthquake magnitude (i.e., the greater the magnitude, the longer the precursor time), Rikitake (1987) estimated an anticipation time from 32 days (radon) to some years for the seismicity precursor of a M7.1 earthquake. It should also be considered that the distance of the monitoring site to the earthquake epicenter could also be important for land-based observations. In fact, it is expected that with a shorter distance, the precursory time is usually longer (Sulthankhodaev, 1984). Therefore, precursory anomalies of only hours to days are

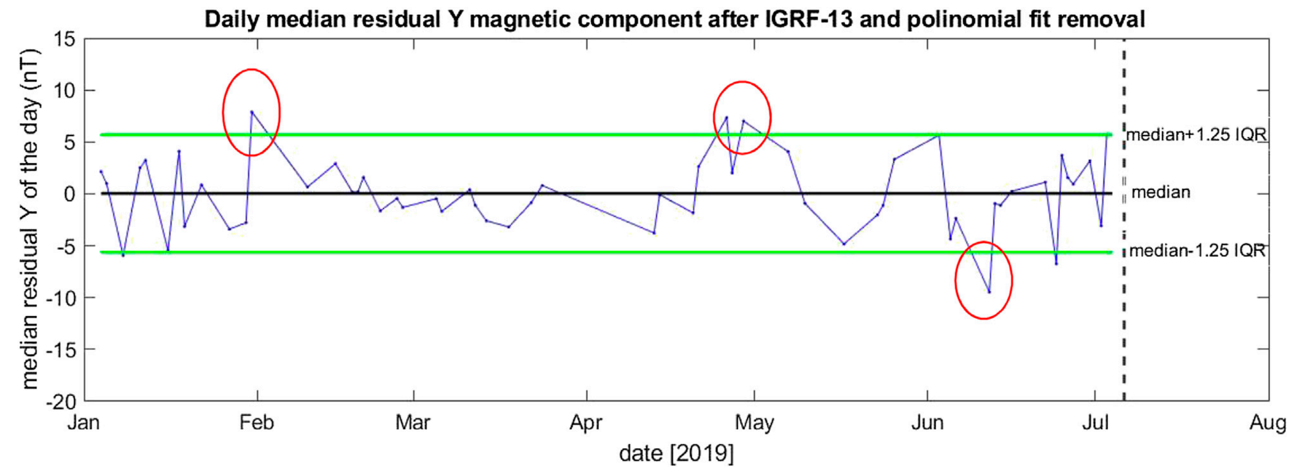

FIGURE 10 | Daily median anomaly taken from Y magnetic field of all Swarm satellites with respect to IGRF-13 model predictions. We underline only the most significant anomalies with red circles. The vertical dashed line represents the mainshock occurrence.

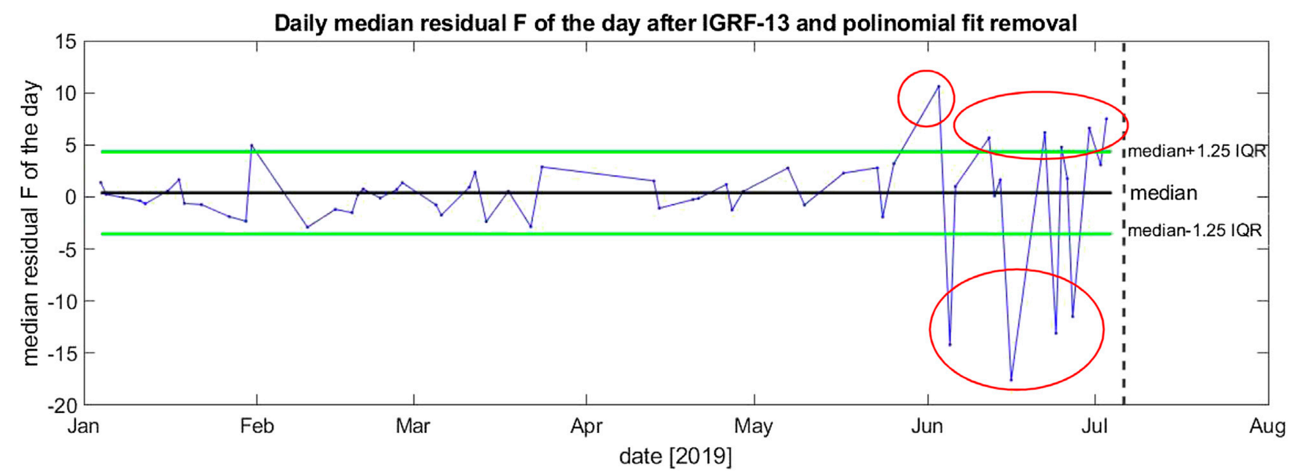

FIGURE 11 | Daily median anomaly taken from total intensity F of all Swarm satellites with respect to IGRF-13 model predictions. Periods of anomalies are evidenced by red circles. The vertical dashed line represents the mainshock occurrence.

TABLE 1 | Type of precursor and corresponding advance time(s).

Type of precursor		Advance time	
Lithosphere (increase of seismicity)		−17 years, −9 years,	quick acceleration a few days before
Atmosphere	Skin temperature (skt)	[−90–75 days]	−25 days
	Total column water vapor (tcwv)	[−85 days]	
	Aerosol optical thickness (AOT)	−60 days	
	Methane (CH_4)	−70 days	
Ionosphere	Ionosonde		−34 days
	Swarm satellite (individual tracks)		−33 days
	(Daily median anomalies)		
	Y	−150 days, −70–65 days,	−25 days
	F		−35 days > −25 days

We highlight synchronicity in some precursors. The dubious anomalies (blue circles in the previous figures) are shown within square brackets.

not frequent. Inan et al. (2010) mention precursory hydrogeochemical anomalies in Western Turkey lasting for more than a month before an earthquake magnitude 4.8; the epicenter was within few tens of kilometers to the observation site. The ground water level data we provide from a borehole located some 200 km distant from the epicenter (**Figure 12**) also show a precursory anomaly lasting almost a year (between September 2018 and July 2019). Another important point is to check whether previous researches investigated or not a long time in advance with respect to the seismic event. For example, DEMETER data investigation (e.g., Yan et al., 2017, which is the last statistic study on EQs-DEMETER) has explored only from 15 days before each earthquake. In De Santis et al. (2019c), published by most of the authors of this article, the DEMETER results with anticipation time around 6 days were confirmed, also giving evidences of the existence of possible longer time precursors, for example, 80 days before the seismic event or even some hundred days before for higher magnitude seismic events, which is in accordance to the Rikitake law. On the other hand, some ionospheric precursors have been also registered up to some months in advance (middle-term precursors) (Sidorin, 1979; Korsunova and Khegai, 2006; Korsunova and Khegai, 2008; Hao et al., 2000; Perrone et al., 2010; Perrone et al., 2018), confirming our present results.

From the overall results of our study, the atmosphere looks very sensitive to the preparation of the impending earthquake and the anomalies tend to concentrate in a few occasions, from three months to almost one before the mainshock. The ionosphere (from ionosonde and Swarm satellite data analysis) provides anomalous signals from five months before the mainshock and then at around 2 months before. It then clearly depicts 2–3 June 2019 as a disturbed period in both ionosonde and satellite, during very quiet geomagnetic conditions. The high compatibility of the anticipation time and distance of the ionosonde with respect to the future epicenter of the earthquake using the Korsunova and Khegai (2006) and Korsunova and Khegai (2008) method can strongly support the hypothesis that this feature is induced by the earthquake preparation processes, e.g., release of ionized particles from the lithosphere (see Freund, 2011; Pulinets and Ouzounov, 2011; Hayakawa et al., 2018), before the Ridgecrest major earthquakes.

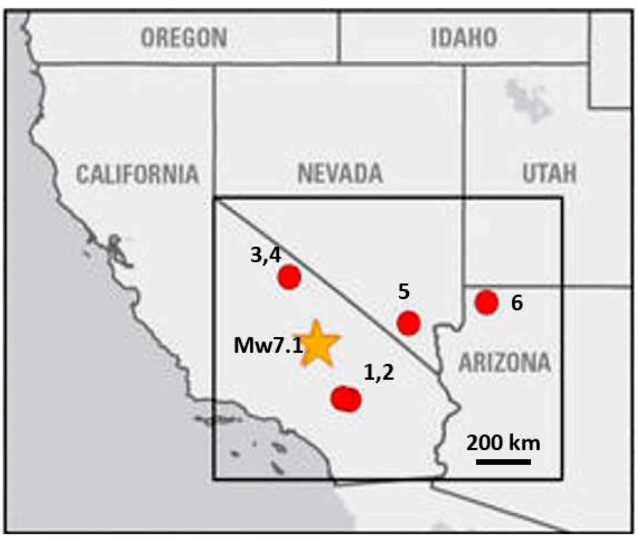

FIGURE 12 | Locations of the epicenter of the July 6, 2019, M7.1 Ridgecrest earthquake and six USGS groundwater-monitoring sites. The monitoring sites shown are California 1) 002S002W02F002S, 2) 002S002W12H001S, 3) 003S027E25N001M, and 4) 003S029E30E002M; Nevada 5) 212 S19 E61 19BC 1 CNLV Deer Springs; and, Arizona 6) B-40-04 06AAC1 [Kaibab-Paiute Well] (USGS 2019).

We can now attempt to consider all anomalies in a unique framework. Particularly powerful is to estimate a cumulative curve of all anomalies together (actually excluding the seismic ones, already included in the AMR fit). When we plot the cumulative number of anomalies (**Figure 13**), we find that a power-law fits the data points very well, much better than a straight line (we fixed the m-exponent of the power law as that typical of a critical system, i.e., $m = 0.25$). This can be measured by the analogous C-factor, already introduced for AMR, i.e., the ratio between the root mean square of the power-law fit w.r.t. the same of the straight line (Bowman et al., 1998). We estimate for this latter cumulate $C = 0.49$, which means a clear acceleration of all the anomalies: by the way, it is interesting that the value of this latter C-factor is almost the same as the one calculated for the AMR, producing a similar conclusion obtained for the M7.8 Nepal 2015 case study comparing seismic and magnetic anomaly patterns by De Santis et al. (2017). Therefore, from **Figure 13,** we can affirm that the anomalies tend to accelerate as the earthquake is approaching, pointing to the time of occurrence with a small uncertainty of only few days (±3 days). Inclusion of the few dubious anomalies (blue circles in the figures of analyses) does not change the overall result significantly. Ground-based precursory anomaly, for verification of our results, was sought and only borehole water level data have been found available from the USGS open access database. USGS reported in October 2019 (USGS, 2019) that oscillatory changes were recorded in short-term water levels of some boreholes varying in distance to the epicenter of the M7.1 earthquake from about 200 to 400 km (**Figure 12**). We downloaded the data for all six borehole locations for a time interval of 4 years (from January 1, 2016, to January 1, 2020) in order to assess the background level and evaluate pre-seismic anomalies, if any. Time series of the water level recorded in one borehole (#2) located about 200 km to the south of the epicenter is given in **Figure 14**. Data from other five boreholes did not enable robust evaluation with respect to seismicity (these can be viewed from USGS, (2019)): we explain this fact because one station (#6) is too far from the epicentral region, while the others (#1, #3, #4, and #5) do not show any pre-earthquake anomaly because of the stress anisotropy and/or block boundaries hindering stress transfer to localities of these stations (similar effects are discussed by Inan et al., 2012). In **Figure 14**, gradual shallowing trend in the water level is apparent until about September 2018 (about 9 months before the mainshock) when disturbance in the data started and the water level started to gradually decrease until July 6, 2019.

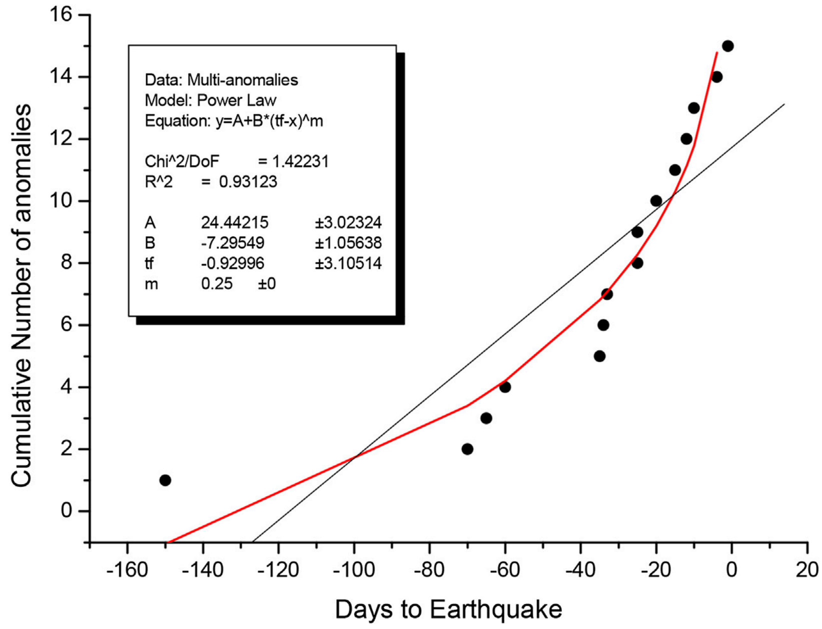

FIGURE 13 | Cumulative number of all clear anomalies (indicated here as black circles; here, we do not consider the lithospheric anomalies of seismicity, already counted in AMR). Time origin t = 0 is the mainshock occurrence. Red fit is a power law while the black is a straight line. As for AMR, also here can be estimated the C-factor, C = 0.49, which confirms a strong acceleration as the mainshock is approaching.

After that, the water level has gradually increased again. An anomaly at 270 days before the mainshock is suggested by the data. Using Sultankhodhaev's (1984) empirical formula, relating the time T (in days) of the anomaly, the distance D (in km) of its location w.r.t. the mainshock epicenter, and the earthquake magnitude M:

$$\log(DT) = 0.63 \cdot M - 0.15, \tag{3}$$

we calculated an expected anomaly anticipation time of 105 days as in this case D = 200 km and M = 7.1. The apparent anomaly anticipation time (270 days) from **Figure 14** and theoretical expected anticipation time (105 days) from the empirical approach correlate well with anomalies detected based on magnetic and ionospheric data as listed in **Table 1**.

From different analyses of seismic, atmospheric, and ionospheric data, as well as limited ground-based observations,

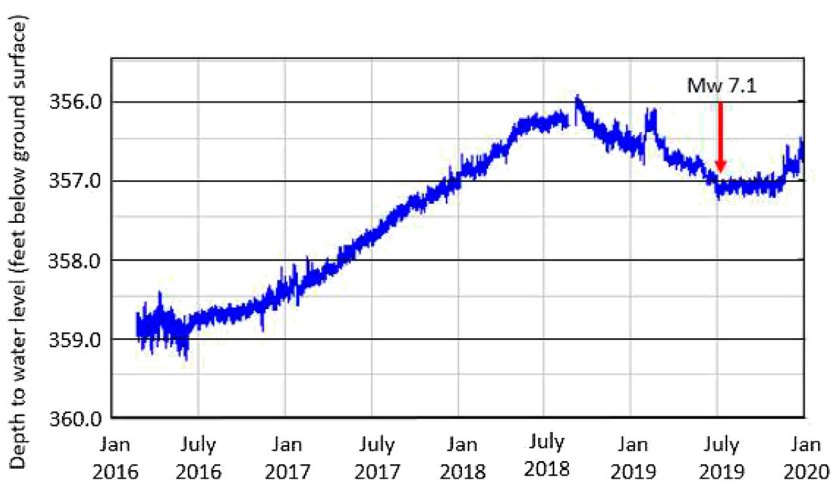

FIGURE 14 | Water level for about 4 years (3.5 years before and half year after the Ridgecrest mainshock) at location #2 (see **Figure 12** for location) (USGS report of October 2019). Disturbance of the water level in September 2018 is followed by gradual decrease of cumulative of about one foot (30.5 cm) until the day of the Ridgecrest mainshock. A peak representing a few weeks in February 2019 (about 5 months) prior to earthquake is also noteworthy.

we find a chain of processes from the ground to atmosphere and ionosphere. We can safely conclude that this series of anomalous events in the different geolayers (lithosphere where the earthquake occurs, atmosphere, and ionosphere) is probably activated by the preparation phase of the Ridgecrest earthquake.

DATA AVAILABILITY STATEMENT

Publicly available datasets were analyzed in this study. These data can be found in USGS Seismic Catalogue, ESA Swarm, ECMWF, and MERRA-2, data Portals.

AUTHOR CONTRIBUTIONS

ADS was responsible for the design and organization of the work, bibliography search, some data analyses and drawing of a few figures, writing the first draft of the article, and editing the final version. GC was involved in the bibliography search, data analyses and preparation of some figures, and editing for the final version. DM, AP, DS, LP, SAC, and SI were involved in the data analyses and preparation of a few figures, and editing the final version.

FUNDING

This work was undertaken in the framework of the European Space Agency (ESA)-funded project SAFE (Swarm for earthquake study) 4000116832/15/NL/MP, while Agenzia Spaziale Italiana (ASI) funded project LIMADOU-Scienza n. 2016-16-H0. Part of the work has been made also under the project ISSI-BJ "The electromagnetic data validation and scientific application research based on CSES satellite."

REFERENCES

Akhoondzadeh, M., De Santis, A., Marchetti, D., Piscini, A., and Cianchini, G. (2018). Multi precursors analysis associated with the powerful Ecuador (MW = 7.8) earthquake of 16 April 2016 using Swarm satellites data in conjunction with other multi-platform satellite and ground data, *Adv. Space Res.* 61, 248–263. doi:10.1016/j.asr.2017.07.014

Akhoondzadeh, M., De Santis, A., Marchetti, D., Piscini, A., and Jin, S. (2019). Anomalous seismo-LAI variations potentially associated with the 2017 Mw = 7.3 Sarpol-e Zahab (Iran) earthquake from Swarm satellites, GPS-TEC and climatological data. *Adv. Space Res.* 64, 143–158. doi:10.1016/j.asr.2019.03.020

Barnhart, W. D., Hayes, G. P., and Gold, R. D. (2019). The July 2019 Ridgecrest, California, earthquake sequence: kinematics of slip and stressing in cross-fault ruptures. *Geophys. Res. Lett.* 46, 11859–11867. doi:10.1029/2019gl084741

Bilitza, D., Altadill, D., Truhlik, V., Shubin, V., Galkin, I., Reinisch, B., et al. (2017). International Reference Ionosphere 2016: from ionospheric climate to real-time weather predictions. *Space Weather* 15, 418–429. doi:10.1002/2016SW001593

Bowman, D. D., Ouillon, G., Sammis, C. G., Sornette, A., and Sornette, D. (1998). An observational test of the critical earthquake concept. *J. Geophys. Res.* 103, 24359–24372. doi:10.1029/98jb00792

Bulut, F. (2015). Different phases of the earthquake cycle captured by seismicity along the North Anatolian Fault. *Geophys. Res. Lett.* 42, 2219–2227. doi:10.1002/2015gl063721

Chen, K., Avouac, J.-P., Aati, S., Milliner, C., Zheng, F., and Shi, C. (2020). Cascading and pulse-like ruptures during the 2019 ridgecrest earthquakes in the Eastern California shear zone. *Nat. Commun.* 11, 22. doi:10.1038/s41467-019-13750-w

Cianchini, G., De Santis, A., Giovambattista, R. D., Abbattista, C., Amoruso, L., Campuzano, S. A., et al. (2020). Revised accelerated moment release under test: fourteen worldwide real case studies in 2014–2018 and simulations. *Pure Appl. Geophys.* 177, 4057–4087. doi:10.1007/s00024-020-02461-9

Cui, J., Shen, X., Zhang, J., Ma, W., and Chu, W. (2019). Analysis of spatiotemporal variations in middle-tropospheric to upper-tropospheric methane during the Wenchuan Ms = 8.0 earthquake by three indices. *Nat. Hazards Earth Syst. Sci.* 19, 2841–2854. doi:10.5194/nhess-19-2841-2019

De Santis, A. (2009). "Geosystemics," in *Proceedings of the 3rd IASME/WSEAS international conference on geology and seismology (GES'09)*, Cambridge, UK, 21–26 February 2009, 36–40.

De Santis, A. (2014). "Geosystemics, Entropy and criticality of earthquakes: a vision of our planet and a key of access," in *Addressing global environmental security through innovative educational curricula*. (Basingstoke, United Kingdom: Springer Nature), 3–20.

De Santis, A., Cianchini, G., and Di Giovambattista, R. (2015). Accelerating moment release revisited: examples of application to Italian seismic sequences. *Tectonophysics* 639, 82–98. doi:10.1016/j.tecto.2014.11.015

De Santis, A., Balasis, G., Pavón-Carrasco, F. J., Cianchini, G., and Mandea, M. (2017). Potential earthquake precursory pattern from space: the 2015 Nepal event as seen by magnetic Swarm satellites. *Earth Planet Sci. Lett.* 461, 119–126. doi:10.1016/j.epsl.2016.12.037

De Santis, A., Abbattista, C., Alfonsi, L., Amoruso, L., Campuzano, S. A., Carbone, M., et al. (2019a). Geosystemics view of earthquakes. *Entropy* 21 (4), 412. doi:10.3390/e21040412

De Santis, A., Marchetti, D., Spogli, L, Cianchini, G., Pavón-Carrasco, F. J., Franceschi, G. D., et al. (2019b). Magnetic field and electron density data analysis from Swarm satellites searching for ionospheric effects by great earthquakes: 12 case studies from 2014 to 2016. *Atmosphere* 10, 371. doi:10.3390/atmos10070371

De Santis, A., Marchetti, D., Pavón-Carrasco, F. J., Cianchini, G., Perrone, L., Abbattista, C., et al. (2019c). Haagmans, Precursory worldwide signatures of earthquake occurrences on Swarm satellite data. *Sci. Rep.* 9, 20287. doi:10.1038/s41598-019-56599-1

Dee, D. P., Uppala, S. M., Simmons, A. J., Berrisford, P., Poli, P., Kobayashi, S., et al. (2011). The ERA-Interim reanalysis: configuration and performance of the data assimilation system. *Q. J. R. Meteorol. Soc.* 137, 553–597. doi:10.1002/qj.828

Di Giovambattista, R., and Tyupkin, Y. S. (2004). Seismicity patterns before the M=5.8 2002, Palermo (Italy) earthquake: seismic quiescence and accelerating seismicity. *Tectonophysics* 384 (1-4), 243–255. doi:10.1016/j.tecto.2004.04.001

Dobrovolsky, I. P., Zubkov, S. I., and Miachkin, V. I. (1979). Estimation of the size of earthquake preparation zones. *PAGE*, 117, 1025–1044. doi:10.1007/bf00876083

Fetzer, E., McMillin, L. M., Tobin, D., Aumann, H. H., Gunson, M. R., McMillan, W. W., et al. (2003). Airs/amsu/hsb validation, geoscience and Remote sensing. *IEEE Transactions* 41 (2), 418–431. doi:10.1109/tgrs.2002.808293

Freund, F. (2011). Pre-earthquake signals: underlying physical processes. *J. Asian Earth Sci.* 41, 383–400. doi:10.1016/j.jseaes.2010.03.009

Freund, F. (2013). Earthquake forewarning—a multidisciplinary challenge from the ground up to space. *Acta Geophysica* 61 (4), 775–807. doi:10.2478/s11600-013-0130-4

Friis-Christensen, E., Luhr, H., and Hulot, G. (2006). Swarm: a constellation to study the Earth's magnetic field. *Earth Planet. Space* 58, 351–358. doi:10.1186/bf03351933

Gelaro, R., McCarty, W., Suárez, M. J., Todling, R., Molod, A., Takacs, L., et al. (2017). The Modern-Era retrospective analysis for research and applications, version 2 (MERRA-2), American meteorological society - modern-Era retrospective analysis for research and applications version 2 (MERRA-2) special collection. *J. Climate* 30 (14), 5419–5454. doi:10.1175/JCLI-D-16-0758.1

Hao, J., Tianming, T., and Li, D. (2000). Progress in the research of atmospheric electric field anomaly as an index for short-impending prediction of earthquakes. *J. Earthquake Prediction Res.* 8, 241–255. doi:10.1007/BF02650462

Hayakawa, M., Asano, T., Rozhnoi, A., and Solovieva, M. (2018). "Very-low- and low-frequency sounding of ionospheric perturbations and possible association with earthquakes," in *Pre-earthquake Processes: a multidisciplinary approach to earthquake prediction studies*. Editors D. Ouzounov, et al. (New York, NY: AGU Book, Wiley), 277–304.

He, L., and Heki, K. (2017). Ionospheric anomalies immediately before Mw7.0–8.0 earthquakes. *J. Geophys. Res. Space Phys.* 122, 8659–8678. doi:10.1002/2017ja024012

Heki, K. (2011). Ionospheric electron Enhancement preceding the 2011 tohoku-oki earthquake. *Geophys. Res. Lett.* 38 (17), 1–5. doi:10.1029/2011gl047908

Ippolito, A., Perrone, L., De Santis, A., and Sabbagh, D. (2020). Ionosonde data analysis in relation to the 2016 central Italian earthquakes. *Geosciences* 10, 354. doi:10.3390/geosciences10090354

İnan, S., Ertekin, K., Seyis, C., Şimşek, Ş., Kulak, F., Dikbaş, A., et al. (2010). Multidisciplinary earthquake researches in Western Turkey: hints to select sites to study geochemical transients associated to seismicity. *Acta Geophysica* 58, 767–813. doi:10.2478/s11600-010-0016-7

İnan, S., Pabuccu, Z., Kulak, F., Ergintav, S., Tatar, O., Altunel, E., et al. (2012). Microplate boundaries as obstacles to pre-earthquake strain transfer in Western Turkey: inferences from continuous geochemical monitoring. *J. As. Earth Sc.* 48, 56–71. doi:10.1016/j.jseaes.2011.12.016

Korsunova, L. P., and Khegai, V. V. (2006). Medium-term ionospheric precursors to strong earthquakes. *Int. J. Geomagn. Aeron.* 6, GI3005, doi:10.1029/2005gi000122

Korsunova, L. P., and Khegai, V. V. (2008). Analysis of seismo-ionospheric disturbances at the chain of Japanese stations for vertical sounding of the ionosphere. *Geomagn. Aeron.* 48, 392–399. doi:10.1134/s0016793208030134

Le Mer, J., and Roger, P. (2001). Production, oxidation, emission and consumption of methane by soils: a review. *Eur. J. Soil Biol.* 37, 25–50. doi:10.1016/s1164-5563(01)01067-6

Liu, Q., De Santis, A., Piscini, A., Cianchini, G., Ventura, G., and Shen, X. (2020). Multi-parametric climatological analysis reveals the involvement of fluids in the preparation phase of the 2008 Ms 8.0 wenchuan and 2013 Ms 7.0 lushan earthquakes. *Rem. Sens.* 12, 1663. doi:10.3390/rs12101663

Marchetti, D., De Santis, A., D'Arcangelo, S., Poggio, F., Piscini, A., Campuzano, A., et al. (2019a). Pre-earthquake chain processes detected from ground to satellite altitude in preparation of the 2016–2017 seismic sequence in Central Italy. *Remote Sens. Environ.* 229, 93–99. doi:10.1016/j.rse.2019.04.033

Marchetti, D., De Santis, A., Shen, X., Campuzano, S. A., Perrone, L., Piscini, A., et al. (2019b). Possible Lithosphere-Atmosphere-Ionosphere Coupling effects prior to the 2018 Mw=7.5 Indonesia earthquake from seismic, atmospheric and ionospheric data. *J. Asian Earth Sci.* 188, 104097. doi:10.1016/j.jseaes.2019.104097

Marchetti, D., De Santis, A., D'Arcangelo, S., Poggio, F., Jin, S., Piscini, A., et al. (2020). Magnetic field and electron density anomalies from Swarm satellites preceding the major earthquakes of the 2016–2017 Amatrice-Norcia (Central Italy) seismic sequence. *Pure Appl. Geophys.* 177, 305–319. doi:10.1007/s00024-019-02138-y

Perrone, L., Korsunova, L. P., and Mikhailov, A. V. (2010). Ionospheric precursors for crustal earthquakes in Italy. *Ann. Geophys.* 28, 941–950. doi:10.5194/angeo-28-941-2010

Perrone, L., De Santis, A., Abbattista, C., Alfonsi, L., Amoruso, L., Carbone, M., et al. (2018). Ionospheric anomalies detected by ionosonde and possibly related to crustal earthquakes in Greece. *Ann. Geophys.* 36, 361–371. doi:10.5194/angeo-36-361-2018

Piscini, A., De Santis, A., Marchetti, D., and Cianchini, G. (2017). A multiparametric climatological approach to study the 2016 Amatrice-Norcia (Central Italy) earthquake preparatory phase. *Pure Appl. Geophys.* 174 (10), 3673–3688. doi:10.1007/s00024-017-1597-8

Piscini, A., Marchetti, D., and De Santis, A. (2019). Multi-parametric climatological analysis associated with global significant volcanic eruptions during 2002–2017. *Pure Appl. Geophys.* 176, 3629–3647. doi:10.1007/s00024-019-02147-x

Pulinets, S., and Ouzounov, D. (2011). Lithosphere–atmosphere–ionosphere coupling (LAIC) model—an unified concept for earthquake precursors validation. *J. Asian Earth Sci.* 41 (4–5), 371–382. doi:10.1016/j.jseaes.2010.03.005

Rikitake, T. (1987). Earthquake precursors in Japan: precursor time and detectability. *Tectonophysics* 136, 265–282. doi:10.1016/0040-1951(87)90029-1

Ross, Z. E., Idini, B., Jia, Z., Stephenson, O. L., Zhong, M., Wang, X., et al. (2019). Hierarchical interlocked orthogonal faulting in the 2019 Ridgecrest earthquake sequence. *Science* 366, 346–351. doi:10.1126/science.aaz0109

Rymer, M. J., Langenheim, V. E., and Hauksson, E. (2002). The hector mine, California, earthquake of 16 october 1999: introduction to the special issue. *Bull. Seismol. Soc. Am.* 92 (4), 1147–1153. doi:10.1785/0120000900

Sidorin, A. Y. (1979). The dependence of the time of appearance of earthquake precursors on the epicenter distance. *Proc. Acad. Sci. USSR* 25 (4), 825, 1979 [in Russian].

Sobolev, G. A., Huang, Q., and Nagao, T. (2002). Phases of earthquake's preparation and by chance test of seismic quiescence anomaly. *J. Geodyn.* 33, 413–424. doi:10.1016/s0264-3707(02)00007-8

Sugan, M., Kato, A., Miyake, H., Nakagawa, S., and Vuan, A. (2014). The preparatory phase of the 2009 Mw 6.3 L'Aquila earthquake by improving the detection capability of low-magnitude foreshocks. *Geophys. Res. Lett.* 41, 6137–6144. doi:10.1002/2014GL061199

Sultankhodhaev, G. A. (1984). *Earthquake prediction*. Paris: UNESCO, 181–191.

USGS (2019). The ups and downs of groundwater levels after the july 2019 ridgecrest, CA earthquakes. Available at: https://www.usgs.gov/center-news/ups-and-downs-groundwater-levels-after-july-2019-ridgecrest-ca-earthquakes. (Accessed October, 2019).

Yan, R., Parrot, M., and Pinçon, J.-L. (2017). Statistical study on variations of the ionospheric ion density observed by DEMETER and related to seismic activities. *J. Geophys. Res. Space Phys.* 122, 12421–12429. doi:10.1002/2017ja024623

Conflict of Interest: The authors declare that the research was conducted in the absence of any commercial or financial relationships that could be construed as a potential conflict of interest.

Remote Sensing of Environment 283 (2022) 113325

Contents lists available at ScienceDirect

Remote Sensing of Environment

journal homepage: www.elsevier.com/locate/rse

A comprehensive multiparametric and multilayer approach to study the preparation phase of large earthquakes from ground to space: The case study of the June 15 2019, M7.2 Kermadec Islands (New Zealand) earthquake

A. De Santis [a,*], L. Perrone [a], M. Calcara [a], S.A. Campuzano [b], G. Cianchini [a], S. D'Arcangelo [a,c], D. Di Mauro [a], D. Marchetti [d], A. Nardi [a], M. Orlando [a], A. Piscini [a], D. Sabbagh [a], M. Soldani [a]

[a] Istituto Nazionale di Geofisica e Vulcanologia, 00143 Rome, Italy
[b] Instituto de Geociencias IGEO (CSIC-UCM), 28040 Madrid, Spain
[c] Universidad Complutense de Madrid - UCM, 28040 Madrid, Spain
[d] College of Instrumentation and Electrical Engineering, Jilin University, 130061 Changchun, China

ARTICLE INFO

Edited by Jing M. Chen

Keywords:
Pre-earthquake anomalies
LAIC
Earthquake
Swarm satellites
CSES

ABSTRACT

This work deals with a comprehensive multiparametric and multilayer approach to study earthquake-related processes that occur during the preparation phase of a large earthquake. As a case study, the paper investigates the M7.2 Kermadec Islands (New Zealand) large earthquake that occurred on June 15, 2019 as the result of shallow reverse faulting within the Tonga-Kermadec subduction zone. The analyses focused on seismic (earthquake catalogs), atmospheric (climatological archives) and ionospheric data from ground to space (mainly satellite) in order to disclose the possible Lithosphere-Atmosphere-Ionosphere Coupling (LAIC). The ionospheric investigations analysed and compared the Global Navigation Satellite System (GNSS) receiver network with in-situ observations from space thanks to both the European Space Agency (ESA) Swarm constellation and the China National Space Administration (CNSA in partnership with Italian Space Agency, ASI) satellite dedicated to search for possible ionospheric disturbances before medium-large earthquakes, i.e. the China Seismo-Electromagnetic Satellite (CSES-01). An interesting comparison is made with another subsequent earthquake with comparable magnitude (M7.1) that occurred in Ridgecrest, California (USA) on 6 July of the same year but in a different tectonic context. Both earthquakes showed anomalies in several parameters (e.g. aerosol, skin temperature and some ionospheric quantities) that appeared at almost the same times before each earthquake occurrence, evidencing a chain of processes that collectively point to the moment of the corresponding mainshock. In both cases, it is demonstrated that a comprehensive multiparametric and multilayer analysis is fundamental to better understand the LAIC in the occasion of complex phenomena such as earthquakes.

1. Introduction

Earthquakes (EQs) release energies roughly proportional to 10^M, where M is their magnitude (e.g. Okal, 2019). The knowledge of the earthquake preparation process is a challenging task in the definition of the chain of events leading to the rupture. In case of large events, they are often made up of a sequence composed of foreshocks, mainshock and aftershocks (e.g. Mogi, 1963; Felzer et al., 2004). The recognition of all signals in the pre-seismic phase, with or without foreshocks, is the main task in earthquake prediction studies. Efforts have been made in real time foreshock phase recognition and, although some significant progress has been found in this field (e.g. McGuire et al., 2005; Gulia and Wiemer, 2019), some difficulties still remain (e.g. Dascher-Cousineau et al., 2020).

Even if one may usually consider a strategy based on seismic data analysis (e.g. De Santis et al., 2015; Cianchini et al., 2020), a non-seismic approach exists, based, for example, on the observation and detection of some anomalous behaviour of the above geolayers, i.e. atmosphere and ionosphere. This is simply justified by the fact that the lithospheric system under tectonic stress, including the earthquake preparation

* Corresponding author.
E-mail address: angelo.desantis@ingv.it (A. De Santis).

https://doi.org/10.1016/j.rse.2022.113325
Received 7 June 2022; Received in revised form 26 September 2022; Accepted 15 October 2022
Available online 28 October 2022

volume, is an open system, with, therefore, mass and energy exchange with neighbour environment, flowing, as an example, into the above atmosphere and, in turn, into the ionosphere, just during the preparation phase of the earthquake. This kind of interaction is also called Lithosphere-Atmosphere-Ionosphere Coupling (LAIC) (Hayakawa and Molchanov, 2002; Freund, 2011; Pulinets and Ouzounov, 2011). Usually, this approach takes advantage of the existence of dense ground observational networks and of currently orbiting satellites. These latter have the potential to have greater probability to be flying periodically over the seismic regions and detect any possible continuous or occasional precursors (e.g. Picozza et al., 2021).

Only recently, space missions were conducted and performed for the investigation of the circumterrestrial environment, with particular attention in observing and studying the possible coupling among solid earth, atmosphere, ionosphere and magnetosphere before strong earthquakes. The French DEMETER satellite (Parrot, 2002; Cussac et al., 2006) represented the very first attempt to put in low-Earth orbit a dedicated satellite for potential detection of ionospheric signals preceding strong earthquakes (e.g. Parrot, 2012). This satellite was flying from 2004 to 2010 and demonstrated to be able to monitor and detect ionospheric effects prior to large earthquakes (e.g. Zhima et al., 2020). Since 2013, the Swarm three-satellite mission by ESA is in progress to monitor the geomagnetic field at the best, taking advantage of the peculiar satellite orbital configuration: two satellites, Alpha and Charlie, fly at around 460 km of altitude while the third satellite, Bravo, flies at about 510 km. Its effectiveness to detect peculiar pre-earthquake anomalies of the magnetic field and electron density in the ionosphere has been lately studied and shown (De Santis et al., 2017, 2019b). The most recent space enterprise with the same objective has been the CSES-01 that was launched on 2 February 2018 and is still orbiting at about 500 km of altitude. Its on-board instruments represent the best nowadays to verify the possibility to observe anomalous behaviour of the ionosphere, possibly due to impending large earthquakes (Shen et al., 2018).

This study analyses multiparametric (seismic, atmospheric, Global Navigation Satellite System -GNSS and satellite) data trying to detect possible anomalies related to the M7.2 (as provided by GeoNet EQ catalogue, or M7.3 from USGS catalogue) Kermadec Islands (New Zealand) EQ, occurred on June 15, 2019 at 22:55:04 UTC, located at 30.644°S, 178.100°W and 46.0 km depth (USGS source: https://earthquake.usgs.gov/earthquakes/eventpage/us6000417i/executive). We also compare the results with the analogous findings of another recent seismic event, i.e. the M7.1 Ridgecrest EQ. (6 July 2019, California, USA; e.g. De Santis et al., 2020), whose open system character has been demonstrated in Pulinets et al. (2021) with the detection of an anomalous flux of radon, just days before the mainshock.

This paper is organized as follows. First, the used data are introduced, then the applied methods together with their main results are presented. Since this work is a comprehensive investigation of the EQ under study, the data analyses are made in the different geolayers from bottom to above, i.e. from lithosphere, atmosphere to ionosphere. All results are then combined and compared with those of the Ridgecrest EQ. We finally conclude with some discussion and conclusions. Although data and methods are different and heterogeneous, we attempt to provide a comprehensive and all-inclusive view of the found results, in the framework of the LAIC model. In addition, some Supplementary Material completes the work with further data analyses and results, complementary to those provided in the main text.

2. Data

In order to study the LAIC effects, several datasets are necessary. In fact, each geolayer that is investigated requires specific data from several sources. As the analysis is conducted separately in each layer, we cope with time/space different resolutions. However, the integration of the different results attempts to take into account these differences. Although some difficulties could be present to investigate the physics of the mechanism of coupling when the time or space resolution is limited, nevertheless the comparison with the results from several layers is still possible.

2.1. Lithospheric data

The seismic event under investigation was located in a very active region where one of the fastest plates (Pacific Plate) subducts beneath the Kermadec-Tonga subduction zone (Fig. 1a); here large earthquakes and volcanic eruptions are taking place (e.g. Smith and Price, 2006; D'Arcangelo et al., 2022).

The USGS catalogue (https://earthquake.usgs.gov/earthquakes/search/) and the national New Zealand catalogue, i.e. the GeoNet Earthquake Catalogue (https://www.geonet.org.nz/), were used in this study. The former catalogue has the advantage of having a global coverage due to a worldwide network of seismic stations and it has a magnitude of completeness (Mc) of about 4.5 worldwide (or even better in last years and for regions - e.g. in USA; Mueller, 2019). *Mc* is an important parameter when estimating *b*-values (Wiemer, 2000): *M*c is the minimum magnitude for which, in a given region and temporal interval, all earthquakes with magnitude $M \geq Mc$ are recorded by the seismic network.

Since we are interested in a deeper understanding and characterisation of the specific region of New Zealand, for more detailed analyses and to achieve a lower magnitude of completeness, we retrieved the seismic data from the GeoNet site too, in the period between January 01, 2018 and June 14, 2019. The area is delimited by the Dobrovolsky strain radius (Dobrovolsky et al., 1979), that scales with magnitude M as $10^{0.43M}$ km, collecting around 18 thousand events. Although the seismic network is decentralised with respect to the epicentre (Fig. 1b), nonetheless the proximity of the northernmost station (GLKZ) assures a good detection capability in the area. The GeoNet earthquake catalogue permits to study more in detail the seismicity because the magnitude of completeness can reach 2.0, or even lower values: in particular it allows to search for some seismic "precursors" such as the variation of *b-value* (e.g. Herrmann et al., 2022) or some recognisable patterns, such as the seismic quiescence or its almost opposite, i.e. the *Accelerated Moment Release (*AMR), and its revised version, hence called R-AMR (*Revised Accelerated Moment Release;* De Santis et al., 2015). To this purpose, we downloaded the New Zealand seismic data from 2018 to the mainshock origin time in a broad region around the epicentre.

2.2. Atmospheric data

As the method of analysis is based on the comparison of the phenomenon's behaviour in the present time with that in the historical background, the downloaded data were analysed from the beginning of their availability until present, and every while we updated our archive with the most recent data. In particular, to investigate the atmosphere we retrieved several parameters, such as SKin Temperature (SKT), Total Column Water Vapour (TCWV), Outgoing Longwave Radiation (OLR), Aerosol Optical Depth (AOD), Carbon Monoxide (CO), Sulphur Dioxide (SO_2) and Methane (CH_4) from ECMWF (European Centre for Medium-range Weather Forecasts) and NASA-NOAA. Most of the data have been selected from climatological re-analysis datasets. These ones have the advantage of having a homogeneous coverage in space and time and to be only slightly altered by observation conditions, like cloud cover for satellite observations. ECMWF elaborated ERA-Interim from 1979 to 2019 and the new version ERA-5 with improvements such as temporal resolution of one hour (instead of 6 h of ERA-Interim) and more parameters and higher space resolution, updated to present in quasi-real time. NASA-NOAA elaborated the climatological model MERRA-2 (Gelaro et al., 2017). This model provides physical and chemical estimations of atmospheric conditions from 1980 to present (updated once per month). Temporal resolution is one hour and spatial resolution is

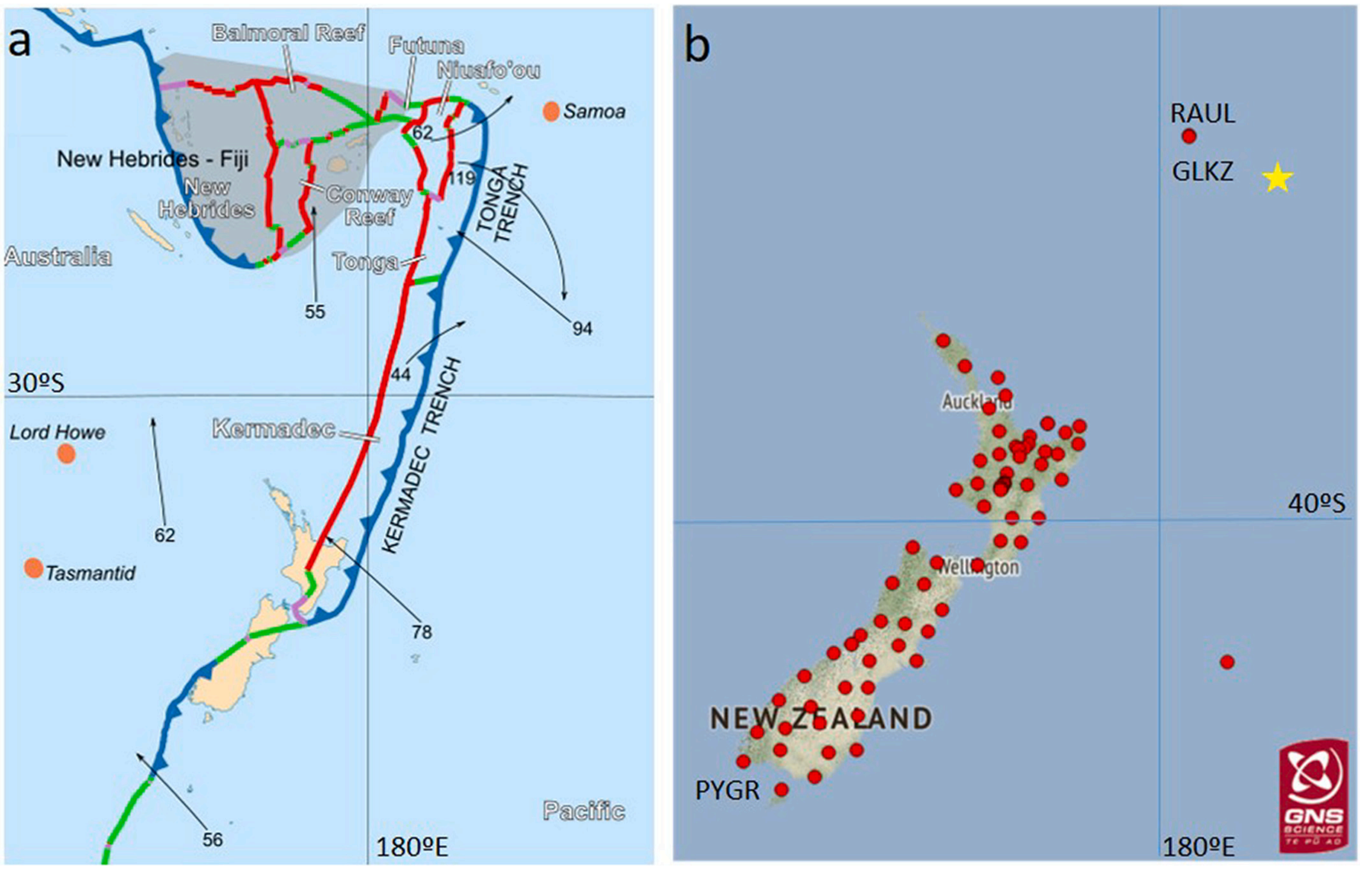

Fig. 1. (a) The Kermadec-Tonga subduction area, where the subduction direction and large velocities (the arrows and the associated velocities w.r.t. Africa in mm/yr) are evidenced. Tectonic margins are shown in red (diverging), green (transform), grey (orogens) and blue (subduction zones); red circles are seismographic stations on Islands (Image source: Wikipedia, under CC BY-SA 3.0); (b) Distribution of the seismographic stations in New Zealand: the northernmost station (GLKZ) is the closest one to the studied epicentre (Image source: GeoNet). Also two GNSS stations (RAUL, very close to the seismic station GLKZ, and PYGR) are shown: their TEC data have been used in our analysis. The yellow star shows the epicentre of the event. (For interpretation of the references to colour in this figure legend, the reader is referred to the web version of this article.)

0.625° longitude, 0.5° latitude. Both ERA-5 and MERRA-2 models were used to obtain the atmospheric parameters. We considered nighttime values because are typically less affected by local meteorological changes. The use of 40 years of data allows us to better evaluate the best background from which estimate the anomalies. The size of the geographical area investigated in the New Zealand region was determined by considering the circular earthquake preparation region (or Dobrovolsky area) centred in the earthquake epicentre (Dobrovolsky et al., 1979).

2.3. Ionospheric data

The ionospheric layer can be investigated in two ways: from in-situ observations by satellites (i.e. from satellites flying across ionosphere) and from ground observations by ionosondes and GNSS receivers. Our study addresses both approaches, mostly concentrating on CSES-01 satellite and integrating with ESA constellation Swarm three-satellites. The CSES-01 satellite is a multiplatform satellite whose main purpose is to search for ionospheric precursors of earthquakes, and for such reason it operates in "burst" mode over seismic active regions, i.e. seismic belts and China (Shen et al., 2018). We deeply investigated the plasma measurements (electron density, Ne and electron temperature, Te) from Langmuir Probes (LAP) and magnetic field measurements from High Precision Magnetometer (HPM) composed by two fluxgates and a Coupled Dark State scalar Magnetometer (CDSM) placed on one of the booms of the satellite. We also investigated the Search Coil Magnetometer (SCM) and Electric Field Detector (EFD) data from CSES-01. This satellite gives the possibility to have a good estimation of the background at two specific a.m. and p.m. local times due to its sun-synchronous orbit. For having a larger picture of the ionosphere at several local times, we integrated the magnetic field and plasma measurements from the Swarm constellation that is equipped with similar payloads with respect to CSES-01 satellite.

The CSES-01 HPM, LAP, SCM and EFD data were available at the CSES satellite web portal (www.leos.ac.cn). Regarding Swarm magnetic field data, they were downloaded as Level 1b low rate (1 Hz) data from all three satellites (up to baseline 0507) until 8 March 2020. For Swarm electron density data, we considered EFI LP (2 Hz), baseline 0501. Both datasets are provided in Common Data Format (CDF) and freely available in the ESA Swarm FTP and HTTP Server swarm-diss.eo.esa.int.

For the ground observations, we used GNSS data from the receivers of the GeoNet GNSS/GPS network (https://www.geonet.org.nz/), located within the earthquake preparation region, together with receivers outside the area of interest included for comparative analysis. The Total Electron Content (TEC), estimated from the time delay between two GPS (Global Positioning System) transmitting frequencies, can also be used to study the eventual effects in the ionosphere due to the preparation phase of strong earthquakes (e.g. Zhu and Jiang, 2020). By the other hand, a ionosonde has the advantage to determine important ionospheric parameters with the best precision, for example the altitude of the F2 layer, its limit-transmitting frequency, the eventual presence of the sporadic layer E, etcetera. Unfortunately, no ionosonde data are available from that area.

3. Data analyses and results

3.1. Seismological data analysis

The seismic data were retrieved from GeoNet Geological Information for New Zealand, in the period between 1 January 2018 and 14 June 2019 over a circular area contained by the Dobrovolsky strain radius, comprising 18,291 events. To characterise the seismicity trend, the first step was to calculate the magnitude of completeness (*M*c). We computed *M*c as a function of time by sliding the time window containing 150 earthquakes by steps of 5 events (Fig. 2a) and its variation in time in bold (grey lines are the upper and lower bands of confidence). Limits of the graph are set between 1 and 3, because it is the typical range of the *M*c values from a dense seismic network.

*M*c values of GeoNet network are quite stable and ranging between 1.8 and 2.2, for the time period considered. So, considering the largest value of the range, the catalogue was filtered in order to exclude all earthquakes with magnitudes lower than $Mc = 2.2$ and to obtain the *b-value* behaviour in time (Fig. 2b). The latter parameter depends on different physical and tectonic setting conditions: stress regime, heterogeneities of materials and temperature (Scholz, 2015). Low *b-values* have been correlated to asperity areas, possible origin of future earthquakes (e.g. Nanjo and Yoshida, 2021). From Fig. 2b it is worth noting a general tendence of decrease, with larger decrease at the end of 2018.

Accelerating seismicity is quite common during the preparation process of EQs. It can be detected by the Accelerated Moment Release (AMR) method, and its recent revised version (R-AMR; De Santis et al., 2015), applied to the EQ catalogue. The AMR method (e.g. Bowman et al., 1998; Bufe and Varnes, 1993) proposes that the cumulative value of the Benioff strain *s*(*t*) (Benioff, 1949), which is proportional to the square root of the EQ energy, may progress following a power-law diverging function with time:

$$s(t) = \sum_{i=1}^{n(t)} \sqrt{E(t_i)} = A + B\left(t_f - t\right)^m \tag{1}$$

where $E(t_i)$ is the energy of the i-th event; *n(t)* is the number of earthquakes at time *t*; $A \equiv s(t)_{|t=t_f} > 0$ at the time of failure t_f (i.e. the mainshock); $B < 0$ and $0 < m < 1$ are constant parameters, usually estimated by a non-linear least squares regression of data; *m* is an exponent representing the degree of accelerating energy release (De Santis et al., 2010), whose values usually are in the interval [0.2, 0.6] (Mignan, 2011). The estimation of the acceleration is given by the so-called *C*-factor (Bowman et al., 1998), defined as the ratio between the root mean square (rms) of the residuals of the non-linear (power-law) fit and the root mean square of the linear fit:

$$C = \frac{rms_{nlin}}{rms_{lin}} \tag{2}$$

If *C* is <1, then acceleration is present, and the lower *C*, the more the acceleration occurs in the seismic data.

When focusing on the state of a specific fault, also the distance R_i of the *i*-th foreshock of the sequence from the mainshock plays an important role. De Santis et al. (2015) introduced a *revised* version of AMR (called R-AMR) to take into account the maximum distance R, supposing that the effects of preceding EQs are still perceived at the fault level, the so-called *minimum strain radius* (Dobrovolsky et al., 1979). The expression for the cumulative reduced strain becomes:

$$\underline{s}(t) = \sum_{i=1}^{n(t)} \sqrt{E(t_i)} \cdot G(R_i) \tag{3}$$

where $G(R_i)$ is an attenuation function depending on the distance R_i of the *i*-th EQ from the epicentre, modelled by De Santis et al. (2015) as

$$G(r) = \begin{cases} r^{-\gamma_0} & r \le R_0 \\ r^{-\gamma_1} & r > R_0 \end{cases} \tag{4}$$

where R_0 denotes the limit between two regions around the seismogenic fault, each with its own weighting exponent γ. By analysing 14 case studies worldwide, Cianchini et al. (2020) evidenced that γ_1 is generally equal to 0.5, while reasonably we set $\gamma_0 = 0$ (De Santis et al., 2015; Cianchini et al., 2020), because there is a small area around the epicentre with negligible attenuation.

The R-AMR estimates, in a sufficiently large area, the collective but surely different effect of each i-th EQ on the fault under study, according to its magnitude M_i and distance R_i from the fault. When we applied the R-AMR method (De Santis et al., 2015) to the downloaded catalogue, we observed that the seismicity accelerated during the preparation phase of the earthquake (Fig. 3). An automatic search for a significant acceleration was applied to seismic time series from the date before the EQ back to past values till *C* was <0.6. It is interesting to notice that the R-AMR detects a clear seismic acceleration ($C = 0.56$) when starting from middle June 2018 and predicts a magnitude similar to the real one (M(A) = 7.1 and M(B) = 7.4; see De Santis et al., 2015 or Cianchini et al., 2020 for their definitions) and a time of failure which is only around 20 days after the mainshock.

3.2. Atmospheric data analysis

In the LAIC approach, some atmospheric quantities and contents of gases have been simultaneously processed in order to identify possible persistent anomalies some days or months before the impending earthquake (Pulinets and Ouzounov, 2011). In particular, a Climatological Analysis for Seismic PRecursor Identification (CAPRI) algorithm (Piscini et al., 2017, 2019) has been applied to the ECMWF Reanalysis v5 (ERA5) and ECMWF Copernicus Atmosphere Monitoring Service (CAMS) climatological dataset with a spatial grid of 0.25° x 0.25°.

The time series of each atmospheric quantity has been collected and preprocessed in order to apply CAPRI algorithm which compares daily time series of the investigated year with the forty-year (1979–2018) historical time series in a temporal window of some months preceding

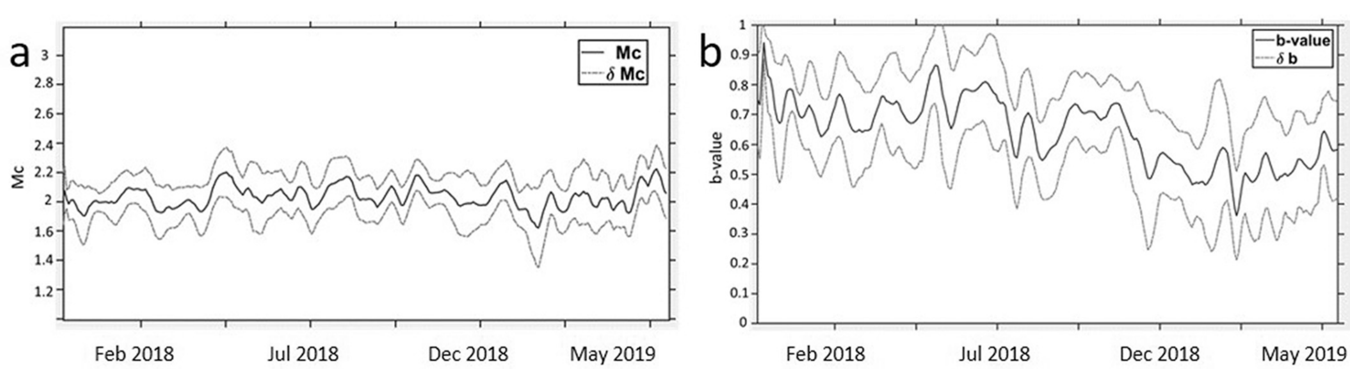

Fig. 2. Estimation of (a) Mc and (b) b-value in function of time with their bands of confidence for the earthquake of interest.

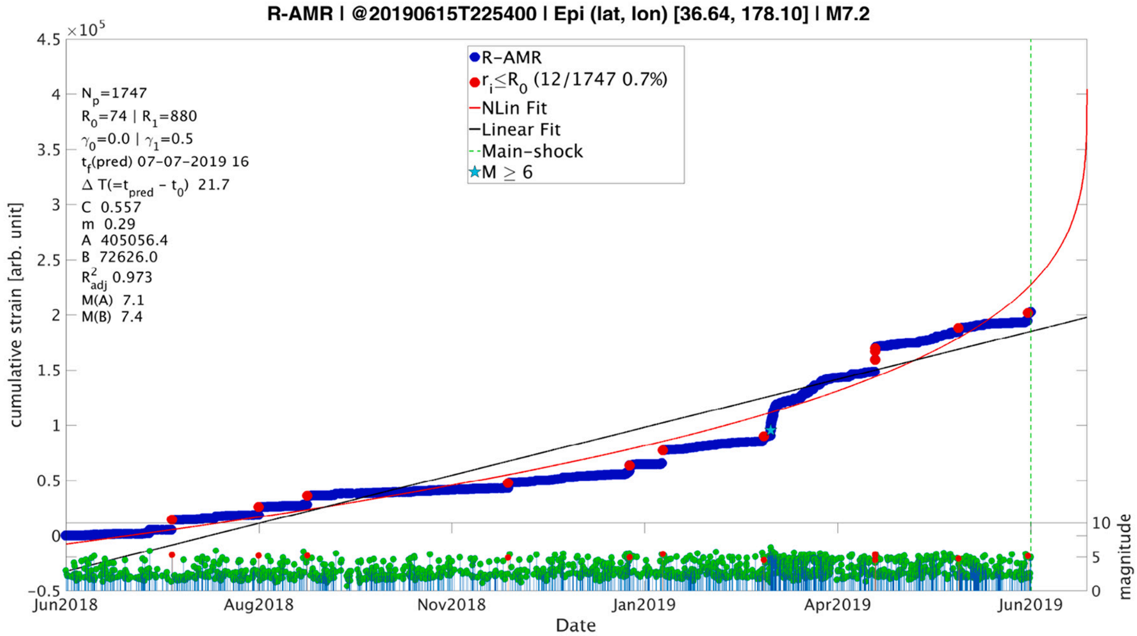

Fig. 3. The R-AMR analysis of the New Zealand catalogue around the 2019 M7.2 Kermadec Islands EQ. The algorithm evidenced an increased seismicity following a rather large foreshock (M > 6; shown as a cyan star) in March 2019, a few months before the mainshock. The figure shows also some parameters involved in the R-AMR analysis (see text for more details). (For interpretation of the references to colour in this figure legend, the reader is referred to the web version of this article.)

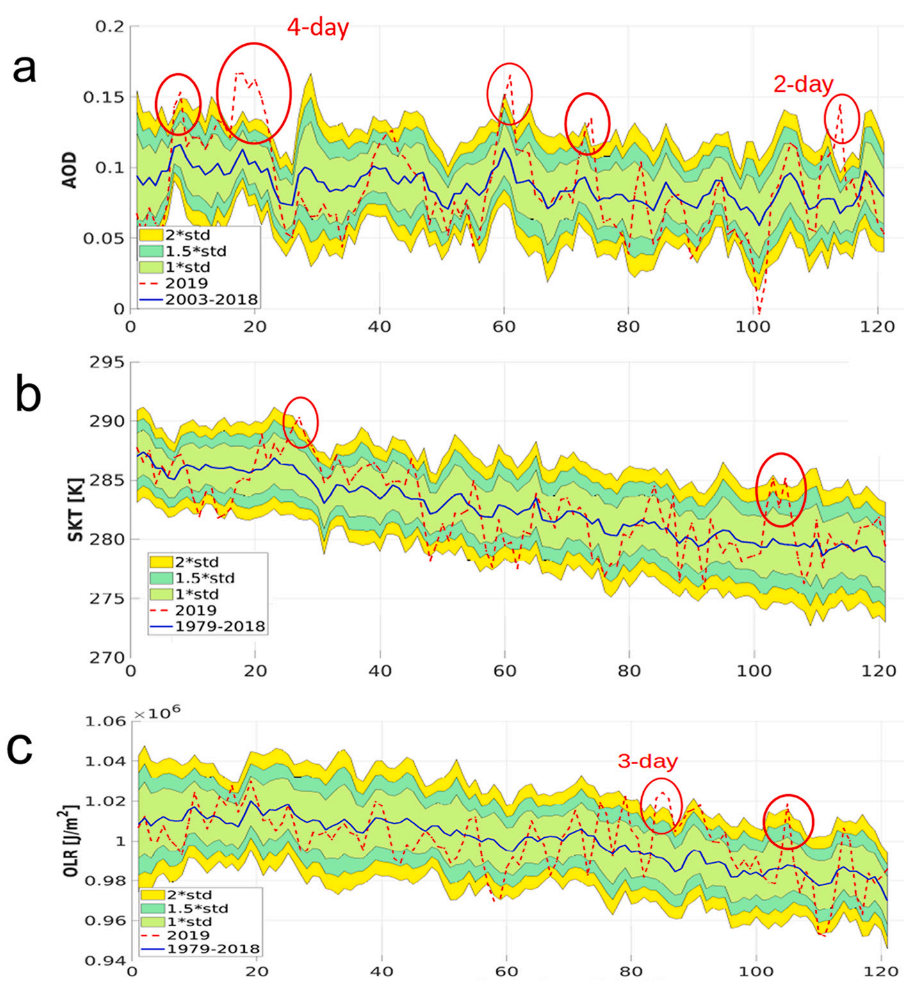

Fig. 4. Case study for the 2019 Kermadec Islands earthquake ECMWF AOD (a), SKT (b) and OLR (c). The 2019 time series (red dashed line) is compared with the historical time series (1979–2018 for SKT and OLR, 2003–2018 for AOD, blue line). The circles put in evidence the identified anomalous days. Coloured stripes indicate 1.0 (green), 1.5 (cyan) and 2.0 (yellow) times the standard deviation (std) from the mean of the historical time series, respectively. The earthquake occurred at the end of the analysed period (120 days). (For interpretation of the references to colour in this figure legend, the reader is referred to the web version of this article.)

the seismic event. If the observable of interest exceeds with a certain persistence the mean of the time series twice the standard deviation, an anomaly is identified. In this work we considered an interval of four months before the earthquake and preferred to identify also single day anomalies, at the cost to have more anomalies than usual.

In particular for ERA5 dataset, that starts from 1979, we focused on physical variables related to thermal radiative interaction of atmosphere with surface, i.e. SKT, TCWV and OLR. ERA5 provides hourly estimates of a large number of atmospheric, land and oceanic climate variables. The data cover the Earth's surface on a 30 km grid and resolve the atmosphere using 137 levels from the surface up to a height of 80 km.

As regard CAMS dataset, content of the main gases, possibly related to surface emissions (Chiodini et al., 2004, 2020), such as CO, SO_2, CH_4 and AOD, have been analysed, with the same 0.25° x 0.25° spatial grid resolution, with the exception of CO dataset that has a spatial resolution with a grid of 0.75° x 0.75°. The CAMS reanalysis dataset covers the period from January 2003 to 2020. We used all data from January 2003 to the date of the earthquake. The CAMS reanalysis is the latest global reanalysis dataset of atmospheric composition (AC) produced by CAMS, consisting of 3-dimensional time-consistent AC fields, including aerosols, chemical species and greenhouse gases (GHGs).

ECMWF climatological analysis for Kermadec Islands 2019 M7.2 seismic event puts in evidence some anomalous days for some of the studied parameters. In particular, AOD shows a 4-day persistent anomaly starting on 3 March 2019, and three single anomalies on 23 February, 17 April and 30 May 2019 (Fig. 4a), with positive anomalies around the epicentre (Fig. 5a). SKT shows two single anomalies on 13 March 2019 and on 30 May 2019 (Fig. 4b), with maximum concentration in northern New Zealand (Fig. 5b). OLR reveals a 3-day persistent anomaly starting on 9 May 2019 and two single anomalies on 15 and 30 May 2019 (Fig. 4c), with the EQ epicentre at the border between maximum and negative values (Fig. 5c). TCWV analysis shows three single anomalies, on 14 March, 31 March and 30 May 2019 (see Supplementary Material). As regards Sulphur dioxide content, it shows two anomalies on 11 April and 3 June (a two-day anomaly) 2019 with spatial concentrations as shown in the Supplementary Material. Methane shows three single anomalies on 10 March 2019, 23 and 25 May 2019, whilst CO analysis does not show any anomaly in the 120 day time window analysed (see Supplementary Material).

A confutation analysis performed for a year without significant

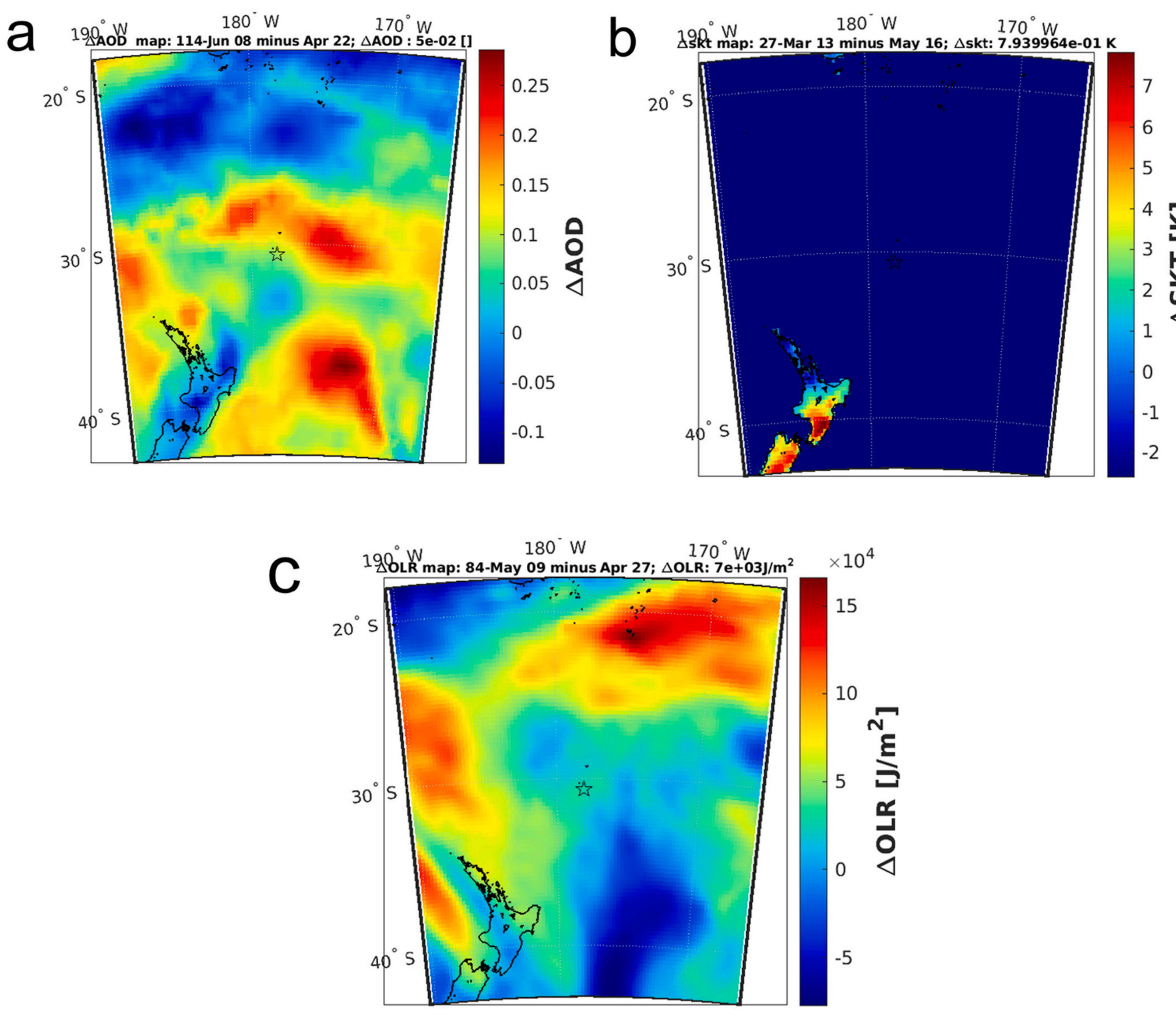

Fig. 5. ECMWF AOD (a), SKT (b) and OLR (c) anomalous day maps of the case study for the 2019 Kermadec Islands earthquake. The values are given as difference with respect to a typical non-anomalous day.

seismicity (i.e. 2018) is shown in the Supplementary Material where SKT and OLR do not show significant anomalies. AOD and SO_2 show many less anomalies than those detected by the same atmospheric quantities in 2019, i.e. the year of the EQ.

3.3. Satellite magnetic and electron density data analysis

After the analyses of lithospheric (i.e. seismological) and atmospheric data, we move to analyse the state of the ionosphere during the preparation of the Kermadec Islands EQ by satellites and GNSS receivers. Swarm and CSES-01 magnetic and Ne datasets are used to analyse and integrate the different approaches that can be implemented to detect electromagnetic anomalies caused by earthquakes preparation phase, thanks to their low earth orbits, at around 500 km of altitude. As shown in the Supplementary Material, starting from MASS (MAgnetic Swarm anomaly detection by Spline analysis; see for example De Santis et al., 2017, 2019b), four different approaches (hereafter also called Method 1, 2, 3 or 4, respectively) have been implemented: 1) classic MASS: using first differences divided by the time interval from sample to next sample and b-splines to remove the long trend; 2) using first differences of the data but removing the long trend by means of a 10-degree polynomial; 3) using the global geomagnetic field model CHAOS (i.e. a magnetic model initially based on **CHA**mp, **Ø**rsted and **S**ac-c satellites; the most recent version 7 also includes Swarm satellite data; Finlay et al., 2020), only for magnetic data, to calculate differences with respect to the satellite data and b-splines to remove the long trend; 4) using CHAOS model to calculate differences with respect to the satellite data and 10-degree polynomial to remove the long trend. The first approach (Method 1), i.e. the classic MASS, has the great advantage to be self-consistent, without the need of a global geomagnetic field model.

The main result of these analyses is a list of the most accurate and consistent anomalies that are provided by the classic MASS, being present in CSES-01 and Swarm magnetic tracks. This study has been performed considering 150 days before the EQ, detecting a promising anomaly 110 days (more than three months) before this event, present in different platform datasets. Fig. 6 shows an example acquired by CSES-01 and Swarm satellites on 25 February 2019. Fig. S11 in the Supplementary Material shows that the solar conditions before and during the found anomaly were quite calm, excluding the possibility of an external magnetic field effect.

In addition, on this day no M5+ EQs have been recorded from the USGS seismic network in a 1500 km area around the M7.2 EQ epicentre, so the anomaly is a great candidate as a possible precursor of the earthquake. From Swarm-CSES-01 joint analysis, the anomaly lasts for several hours from about 9:35 UTC to 17:10 UTC (i.e. 7 h and 35 min), still with a possible residual at 21:15 UTC. The peak of intensity of the anomaly has been recorded by nighttime passage of CSES-01 satellite in the area at 14:35 UTC, reaching a significant anomaly of 20 nT peak-to-peak, which seems in any case too much for a seismo-induced phenomenon.

Fig. 7 shows a CSES-01 anomalous track detected the day before the previous case. Also this anomaly is quite interesting: in fact, the highest intensity is in the Y-East component as expected for internal anomalies (Pinheiro et al., 2011) and it is the only anomaly in the whole track between 50° South and 50° North of geomagnetic latitude. In addition, also this track presents an anomaly intensity in the Y component of about 20 nT. The geomagnetic conditions were quiet (geomagnetic indices: Dst = −1 nT, ap = 4 nT and AE = 24 nT; source: World Data Center for Geomagnetism, Kyoto, http://wdc.kugi.kyoto-u.ac.jp/) and the anomaly is localised over land, in the southern segment of the plate boundary and at the border (but inside) the Dobrovolsky area. It is interesting to notice that the anomalies appear in the magnetic field components (larger in the Y-component) but not in the total intensity: this implies that the perturbation rotates the magnetic field vector without changing its intensity.

Fig. 8 shows a CSES-01 magnetic field track that contains a decrease

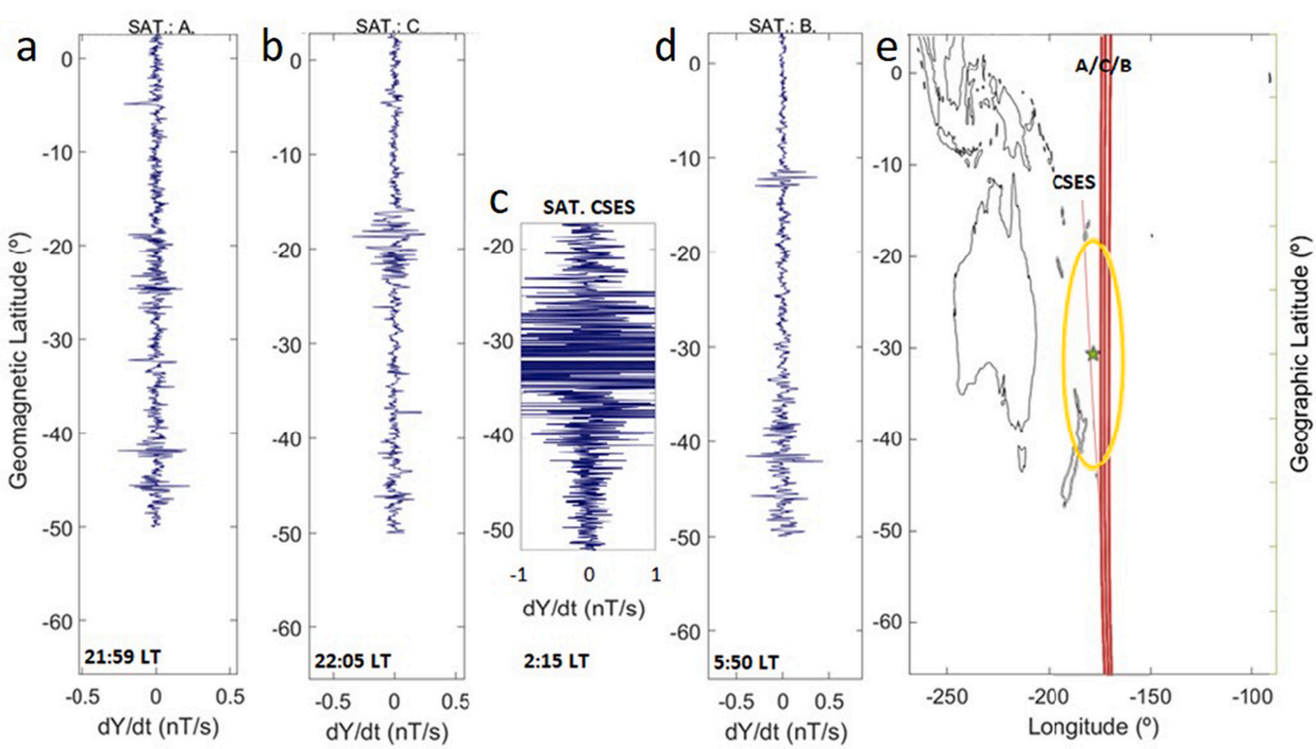

Fig. 6. Magnetic field Y-component analysis using the classic MASS method (Method 1) in different tracks of Swarm A (a), B (b), C(d) and CSES-01 (c) on 25 February 2019 for the local time windows as indicated in the form hh:mm. Red lines in panel e (with the geographical map) correspond to the four satellites' paths. The yellow oval is the Dobrovolsky area; the star is the EQ epicentre. (For interpretation of the references to colour in this figure legend, the reader is referred to the web version of this article.)

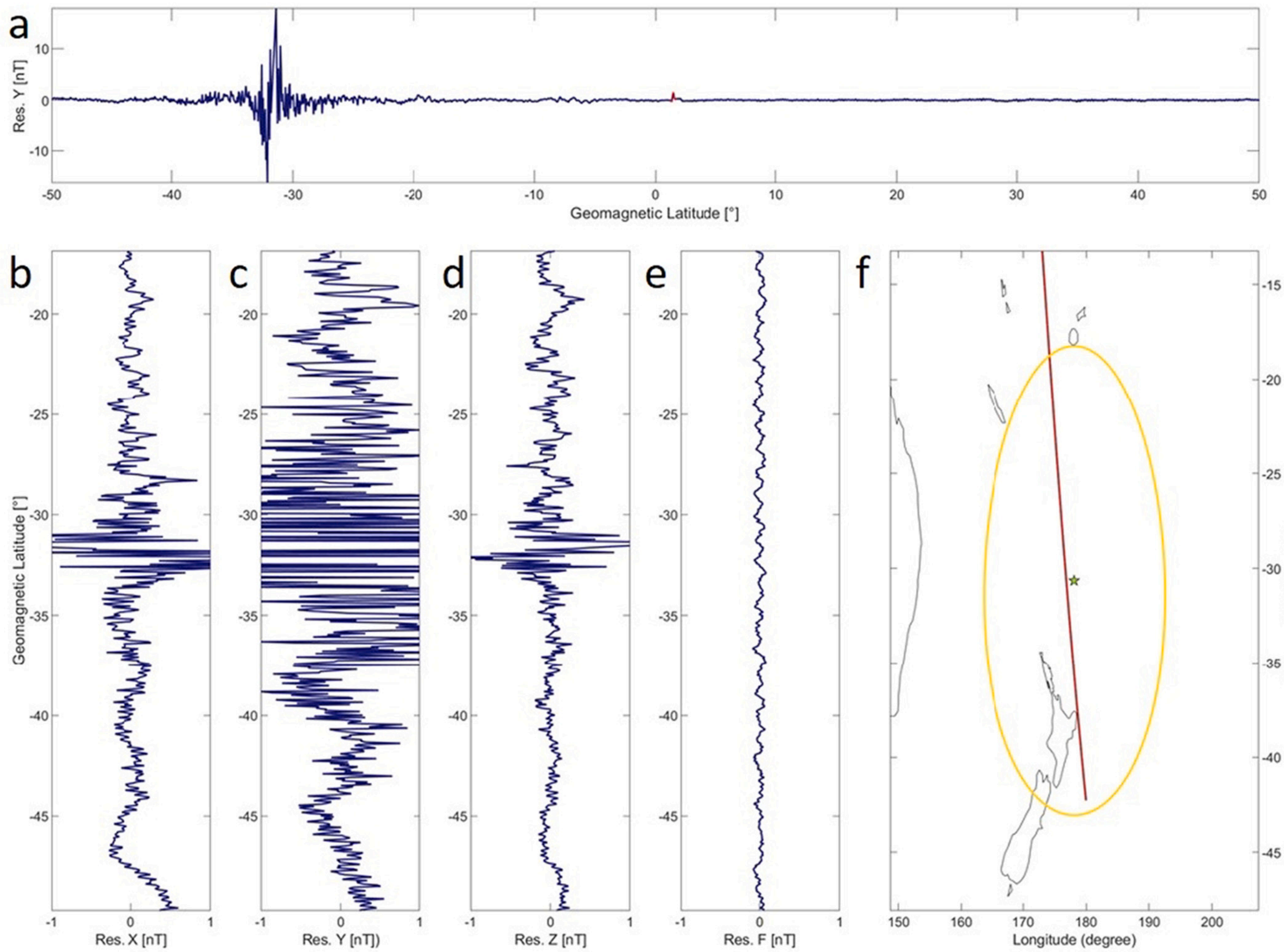

Fig. 7. Anomalous magnetic track of CSES-01 on 24 February 2019 analysed by method 3. a) Residuals of Y component vs. time; Residuals of (b) X, (c)Y, (d) Z and (e) F and (f) geographical map. The yellow oval is the Dobrovolsky area; the star is the EQ epicentre; the red line is the satellite path. (For interpretation of the references to colour in this figure legend, the reader is referred to the web version of this article.)

of Y-East component of magnetic field around the future epicentral latitude (extended a little northern). The track, acquired in geomagnetic quiet time (with Dst = −4 nT, ap = 4 nT and AE = 225 nT), shows a little geomagnetic activity at higher latitudes but the level is not anyway so strong.

Fig. 9 shows the track acquired by Swarm Charlie only 22 h and 36 min before the event. We notice a certain similarity of the anomaly with the track acquired 15 min before the Ridgecrest (California, USA) M7.1 EQ occurrence (see Fig. 1 of Marchetti et al., 2020). In addition, the ionospheric plasma has been investigated, with particular attention to the electron density Ne, to search for possible pre-earthquake ionospheric disturbances by the NeLOG algorithm (see De Santis et al., 2019a, for a full description of the method). NeLOG analyses the decimal logarithm of Ne by a 10-degree polynomial fit (red lines in Fig. 10a) and calculates the residual. If a sample overpasses by k_t times the standard deviation of the residual, it is marked by a blue asterisk in the figure. The method then classifies the track as “anomalous” if it contains >10 anomalous samples in the Dobrovolsky area. Fig. 10 shows an interesting example of an anomalous Ne track of Swarm Alpha satellite acquired 119 days before the M7.2 Kermadec Islands (New Zealand) EQ. This track shows a clear enhancement of Ne at a geomagnetic latitude of about −28° similar to the example shown in De Santis et al., 2021 with CSES-01 satellite in the case of a smaller magnitude earthquake. The track has been acquired during geomagnetic very quiet conditions (Dst = −6 nT and a_p = 0 nT). The same track is given in the Supplementary Material (Fig. S13) where, together with Ne, also the tracks of Te and Vs of Swarm-A satellite are shown.

On 1 June 2019, i.e. two weeks before the mainshock, Swarm Alpha detected an interesting electron density latitudinal profile that crossed the longitude of the incoming earthquake epicentre during nighttime and quiet geomagnetic conditions (see Fig. 11). The red box enlightens a part of the Ne profile that seems to be anomalously increased in terms of its absolute value between −44° and − 29° of latitude. Furthermore the same track shows two perturbations around the mean track value highlighted by continuous and dashed red ovals. Interestingly, all such anomalous features are localised inside the Dobrovolsky area and, in particular, the stronger perturbation, underlined by the continuous red oval, is localised at the same latitude of the future epicentre. Such perturbations not only are unusual at night time LT = 01:13 AM but also are localised southern of the typical geomagnetic latitude of the possible residual of daily EIA that could appear at about −15° / -20° geomagnetic latitude, and also sufficiently far from the South pole. Therefore for exclusion the remaining hypothesis on its origin could be a seismo-induced phenomenon.

3.4. Total Electron Content (TEC) data analysis

TEC data from GNSS receivers can also be analysed to detect electromagnetic anomalies possibly related to impending earthquakes. Vertical TEC (vTEC) data calibrated applying the techniques described

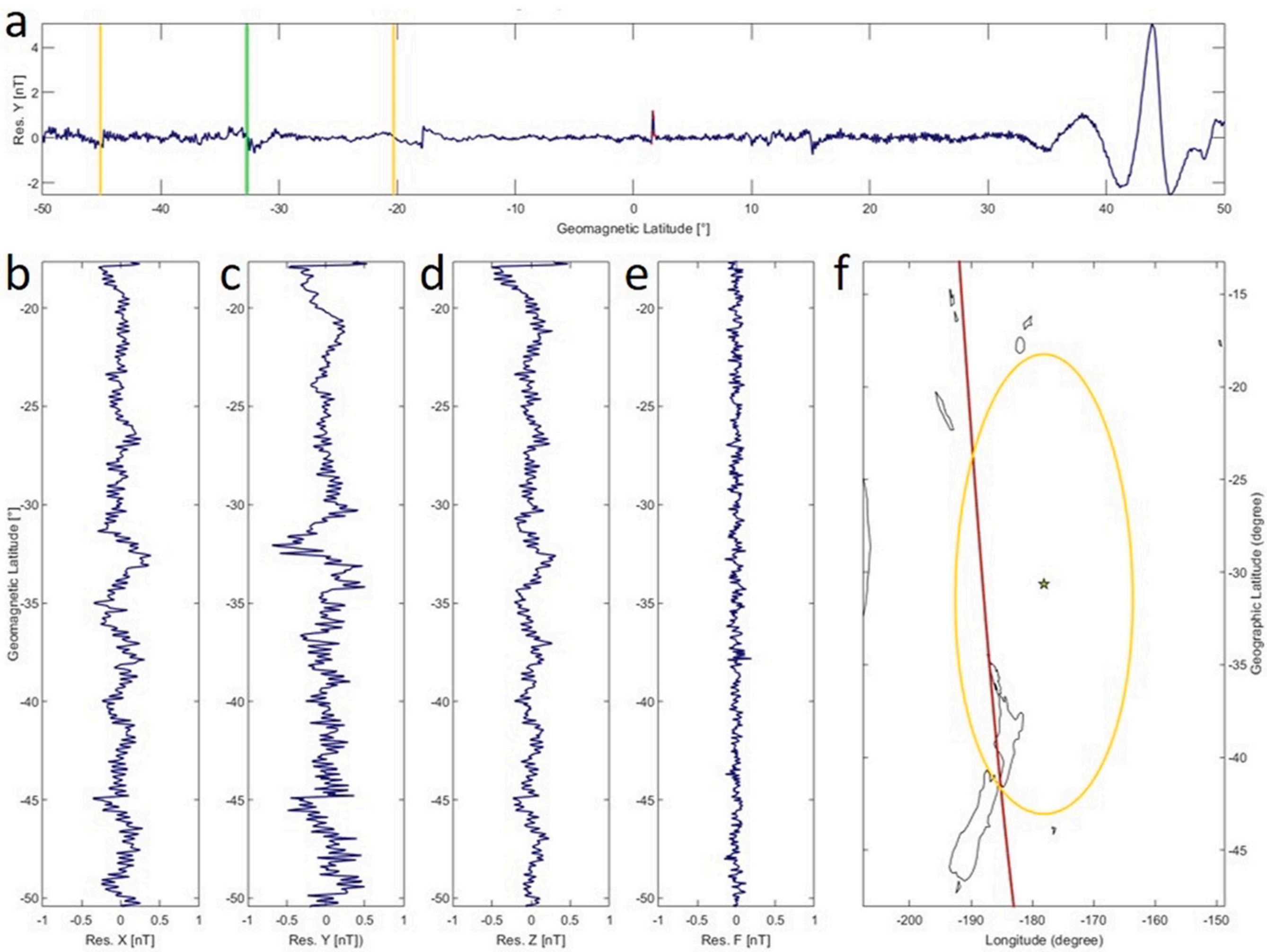

Fig. 8. As Fig. 7 but on 30 April 2019 analysed by method 3. In (a), the vertical lines represent epicentral latitude (green) and limits of the Dobrovolsky area (yellow). In (f), the green star represents the epicentre location while the yellow circle is the corresponding Dobrovolsky area. (For interpretation of the references to colour in this figure legend, the reader is referred to the web version of this article.)

in Ciraolo et al. (2007) and Cesaroni et al. (2015) to RINEX data recorded from 4 months preceding up to 1 month after the earthquake occurrence at selected stations of the GeoNet GNSS/GPS network are used for this purpose, i.e. RAUL, GLKZ and PYGR (see Fig. 1b).

Anomalous variations of vTEC are defined following four different approaches, respectively applied to a single station (method **1**, applied to data close to the epicentre), two stations (methods **2** and **3**, consisting of differential analyses between data close to the epicentre and rather distant ones), and three stations (method **4**, differential analysis among data from stations at different distances from the epicentre). For all the methods, geomagnetic conditions are taken into account in order to exclude anomalies of external origin.

Among such approaches, the two-station differential analysis of method **3** seems to be the most promising, and is presented here in detail (for the detailed definitions and analyses by the other methods, see the Supplementary Material). In this method, the vTEC relative deviations (dTEC) between data of a couple of distant receivers is considered, in the specific:

$$dTEC = (vTEC_{RAUL} - vTEC_{PYGR})/vTEC_{PYGR}, \tag{5}$$

being RAUL receiver (29.24° S; 177.93° W) the closest available to the earthquake epicentre, with a distance of 156 km, while PYGR (46.17° S; 166.68° E) is the most distant one among those of the GeoNet network, with a distance of about 2170 km (Fig. 1b). This means that dTEC large values reflect vTEC large values near the epicentre in correspondence to lower values outside the earthquake preparation zone, being then considered possibly affected by pre-earthquake processes.

In method **3**, the anomalies are defined by comparing the dTEC values calculated every 30 s to the mean linear trend m of the linear fit to data within the 4 months prior to the earthquake. In this case, an anomaly is defined as a set of dTEC values continuously exceeding m + 2 TECU (corresponding to about m + 3.5σ in case of a Gaussian distribution of the residuals) for at least 5 min. The anomalies occurred under disturbed geomagnetic conditions are discarded, where $|Dst| > 20nT$ or $AE > 200$ nT conditions are applied to the instantaneous and daily maxima of the corresponding geomagnetic indices as a proxy of disturbed conditions. Fig. 12 shows the application of this method to the earthquake under analysis. In the same figure also the EQ occurrences are shown together with their range of magnitudes (when more than one EQ occurred on the same day and in the Dobrovolsky area).

This analysis revealed three possible precursory anomalies, some of which were detected also using different approaches. In particular, the 18 March anomaly is recognized also by method **2** (Fig. S16 in the Supplementary Material), and the one of 5 June by both methods **1** applied to RAUL data (Fig. S15) and method **2**, despite the latter confirming the anomaly only with respect to the first background (Fig. S16a). It should be noted here that the application of method **4** for the three-station differential analysis revealed only an anomaly on 18 March, detected also by both the methods for the two-station differential

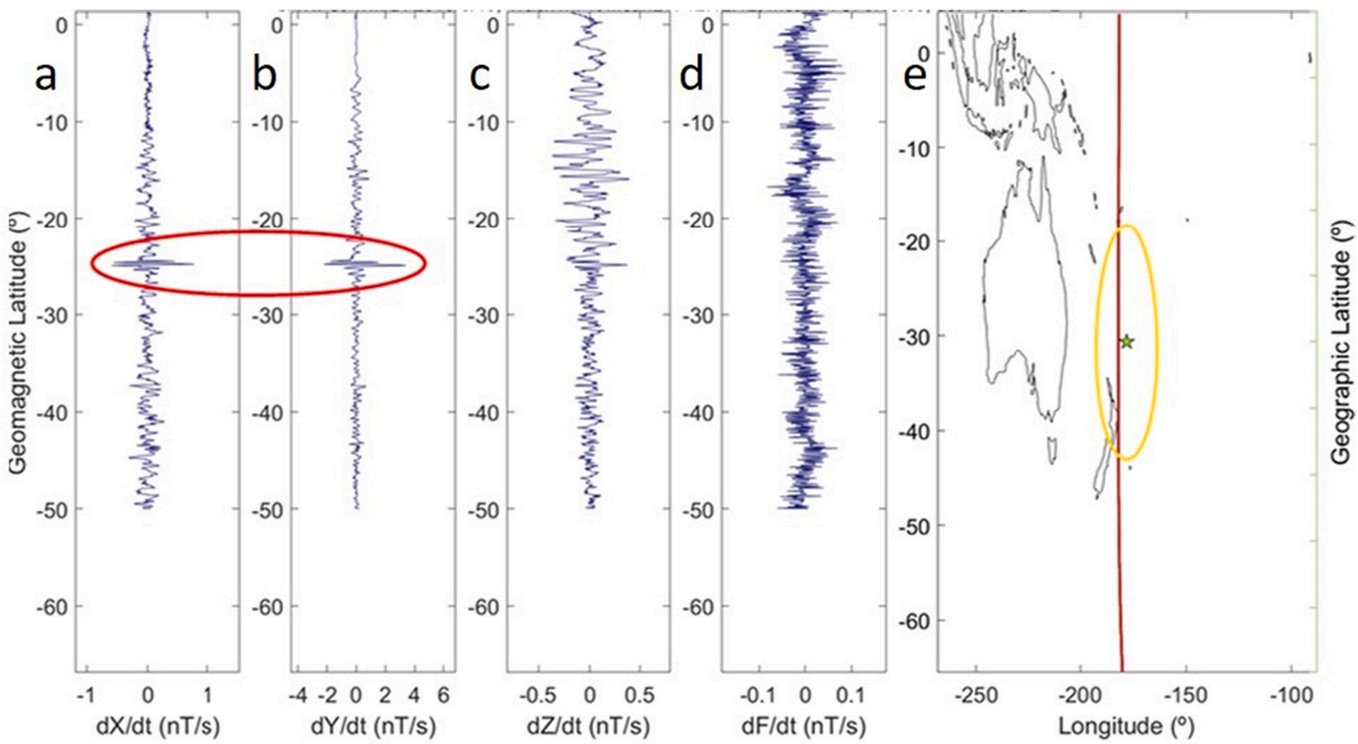

Fig. 9. Anomalous magnetic track of Swarm Charlie on 15 June 2019 (the day of the earthquake) analysed by method 1 (MASS), showing the first differences of a) X, b) Y, c) Z magnetic field components and d) total intensity; e) geographical map with Dobrovolsky area (yellow), satellite orbit (red) and epicentre (green star). (For interpretation of the references to colour in this figure legend, the reader is referred to the web version of this article.)

analysis, as possibly related to the impending earthquake. Of course, we cannot exclude that some anomaly could be associated to a closer EQ with lower magnitude (indicated by a vertical green arrow in Fig. 12), but since the discrimination is impossible, we attribute all found anomalies to the preparation of the largest magnitude M7.2 EQ of interest.

The Supplementary Material also presents the same analysis but applied to the same 4-month period of the 2018 year as confutation analysis. Please note that this tectonic area is very active seismically so it is almost impossible to find periods without significant seismicity: we chose 2018 because only two M5.7+ EQs (actually one outside but close to the period of interest) occurred in this period (while in the investigated 2019 year there were 9 EQs). Also in 2018 there are some anomalies, but many less than in 2019, and those occurred could be precursors of the few EQs occurred in this period of 2018.

3.5. CSES-01 Search Coil Magnetometer and Electric Field Detector spectral analysis

Spectral analysis of magnetic and electric signals acquired by Search Coil Magnetometer (SCM) and Electric Field Detector (EFD), working on board CSES-01 satellite (Wang et al., 2018), were also considered in the period 1 June - 13 July 2019. In particular, we analysed magnetic and electric field variations in the Extremely Low Frequency band (ELF, 200–2200 Hz, with 10.24 kHz and 5.12 KHz sampling rate, respectively). Our aim is to detect anomalies preceding large earthquakes, by means of the evaluation of the spectral information content emerging in some frequency band, in similar way as applied in previous case studies (e.g. Carbone et al., 2021; Piersanti et al., 2020; Wang et al., 2018). Fig. 13 shows the CSES-01 orbit 74,991 (day 10 June 2019), passing through the Dobrovolsky area (green circle) of the Kermadec Islands (New Zealand) EQ, while Fig. 14 illustrates the spectrograms of both SCM (a) and EFD (b) in the ELF band.

Observing the spectrograms of the magnetic field (all three components) and the electric field (mainly Y and Z components), we can see the presence of a possible anomaly within the Dobrovolsky area at frequencies lower than around 500 Hz (see Fig. 14).

To better study this anomaly, we resorted to the concept of Shannon Entropy (Shannon, 1948). A spectrogram represents the temporal variation of the power spectral density; starting from this, at any moment the entropy H(S) associated with the spectrum S is calculated as defined by Shannon (1948):

$$H(S) = -\sum_{i=1}^{N} p(s_i)\cdot log_{10}p(s_i) \tag{6}$$

where S is a discrete random variable that can assume N distinct values $s_1, \ldots, s_N$ and the probability function $p(s_i)$ represents its statistical distribution. The results are shown in the Fig. 15, which represents the trends of the normalised entropy $H(S)/log_{10}N$ as time varies, for the magnetic and the electric fields. Entropy is higher if there is decorrelation between samples, while it is lower when values $s_1, \ldots, s_N$ are correlated.

As you can see, in the area near the epicentre there seems to show a clear correlation between the samples of the spectrum of magnetic and electric fields, while elsewhere these seem to be less correlated with each other.

The main feature that emerges from both the magnetic and electric field spectrograms (Fig. 14) is the power concentration around the Dobrovolsky area (green vertical lines) in a limited region of the spectrum (below and close to 500 Hz). A similar anomaly frequency was detected for 2009 L'Aquila EQ (in that case it was 330 Hz; Bertello et al., 2018). The energy concentration in a limited range of frequencies reflects in the evident concave behaviour in the entropy (Fig. 15). A deeper inspection reveals the same power concentration in the equivalent spectral band ($f \leq 500$ Hz) in both magnetic and electric field spectra, in a portion of the orbit (latitude interval) which is the symmetrical counterpart with respect to the magnetic equator (see Fig. 13). Although less energetic (and so less clear), of course this similar feature emerges,

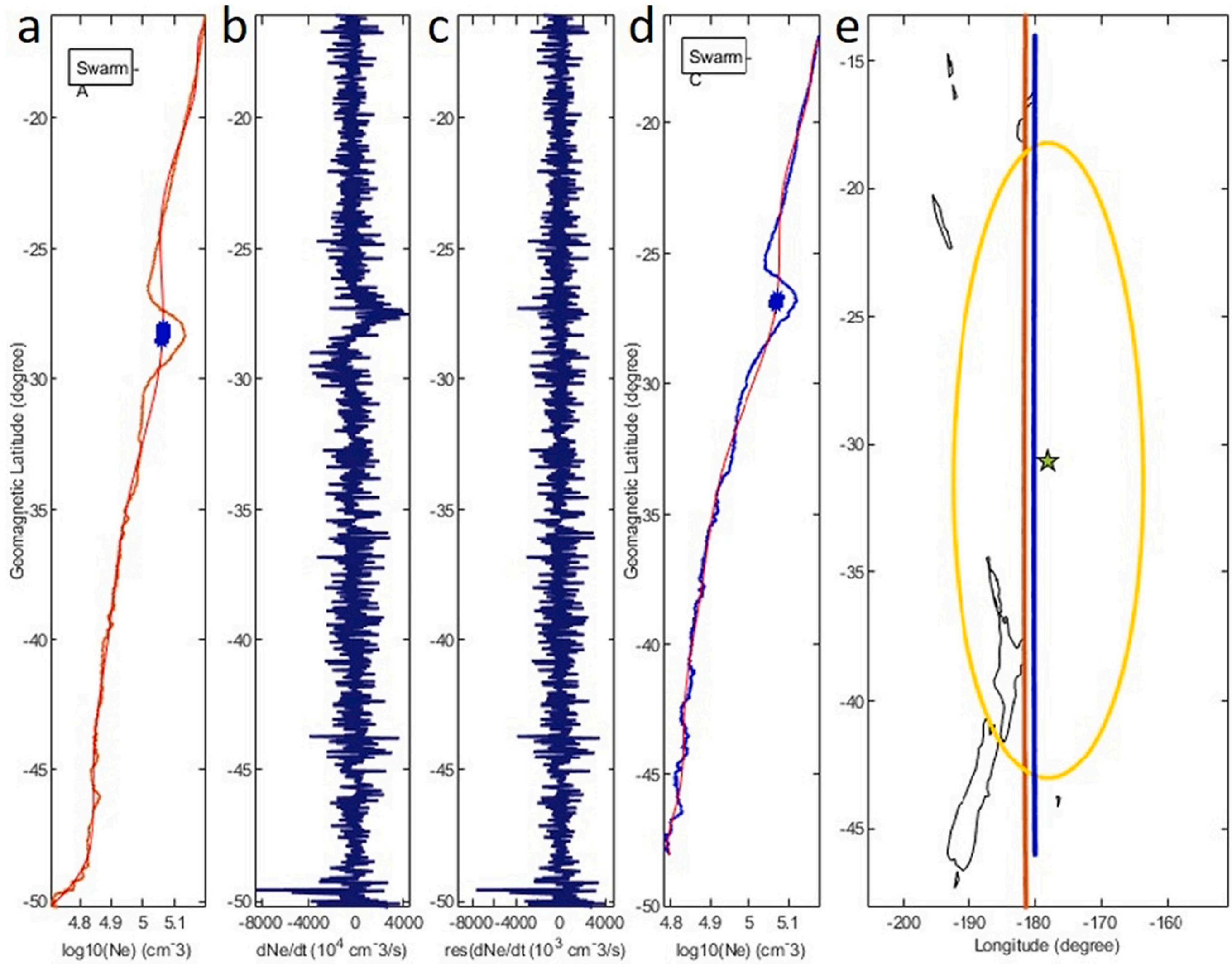

Fig. 10. Anomalous electron density Ne track of Swarm Alpha on 16 February 2019 (~119 days before the mainshock) elaborated by NeLOG with $k_t = 2.5$. From left the figure shows: a) the log Ne, b) the first differences of Ne and c) residual with respect to the mean polynomial trend for satellite Alpha; then it shows d) the log Ne for Swarm Charlie. The two orbits are shown in the geographic map in e): red for Alpha and blue for Charlie. (For interpretation of the references to colour in this figure legend, the reader is referred to the web version of this article.)

correspondingly, in their entropies, where the evident depression around the Dobrovolsky area replicates to a lesser extent in the symmetric area, delimited by the magenta vertical lines (Fig. 15). A clear and founded explanation requires a deeper and focused inspection. Nonetheless, a simple speculation could be that the entropy decreases over the preparation area (represented by the Dobrovolsky region) because of the coupling between the lithosphere under stress and the above ionosphere (through the atmosphere in the between); and that coupling reflects to the symmetric latitudes through the current system along the magnetic field lines (e.g. Sorokin et al., 2019).

4. A comparison with 2019 M7.1 Ridgecrest Earthquake

In this section, the occurrences of the various precursors of the Kermadec Islands EQ with those of Ridgecrest EQ (occurred on 6 July 2019 03:19:53 (UTC) - 35.770°N 117.599° W, 8.0km depth) are compared. The likeness of the pre-earthquake anomalies between the two earthquakes is instructive because the two earthquakes have similar magnitudes, although they occurred in two very different tectonic contexts. Table 1 summarises the occurrences of the anomalies, where the number corresponds to the day with respect to the EQ occurrence, being in bold black those of Kermadec Islands EQ and in light black those of Ridgecrest EQ. The rows of the table are placed from top to bottom almost in altitude order, i.e. from lithosphere, atmosphere to ionosphere. In general, the anomalies tend to occur closer to the earthquake occurrence going up into the atmosphere and ionosphere. As shown by Table 1, the lithospheric anomalies (either in terms of *b*-value decrease and the beginning of the R-AMR acceleration) precede all the atmospheric and ionospheric anomalies. In addition, some atmospheric and ionospheric anomalies appear at almost the same time with respect to the EQ occurrence: impressive almost simultaneous precursors (within a 10-day interval) appear around 90 days before the EQ for aerosol (AOD and AOT), SKT, TCWV and TEC values. Interestingly, the final acceleration (increasing number of anomalies) occurs as the earthquake is approaching (say, in the last two weeks), especially in the ionosphere. Another consideration is speculative, trying to connect atmospheric to ionospheric anomalies: while some of the latter (here called **Case 1** ionospheric anomalies) occur well before the atmospheric anomalies (e.g. Y and Ne at >100 days), others (here called ***Case 2*** ionospheric anomalies) seem to occur with some delay (5–10 days) with respect to the atmospheric anomalies. This delay seems more typical of a diffusion propagation of the atmosphere-ionosphere coupling that requires a

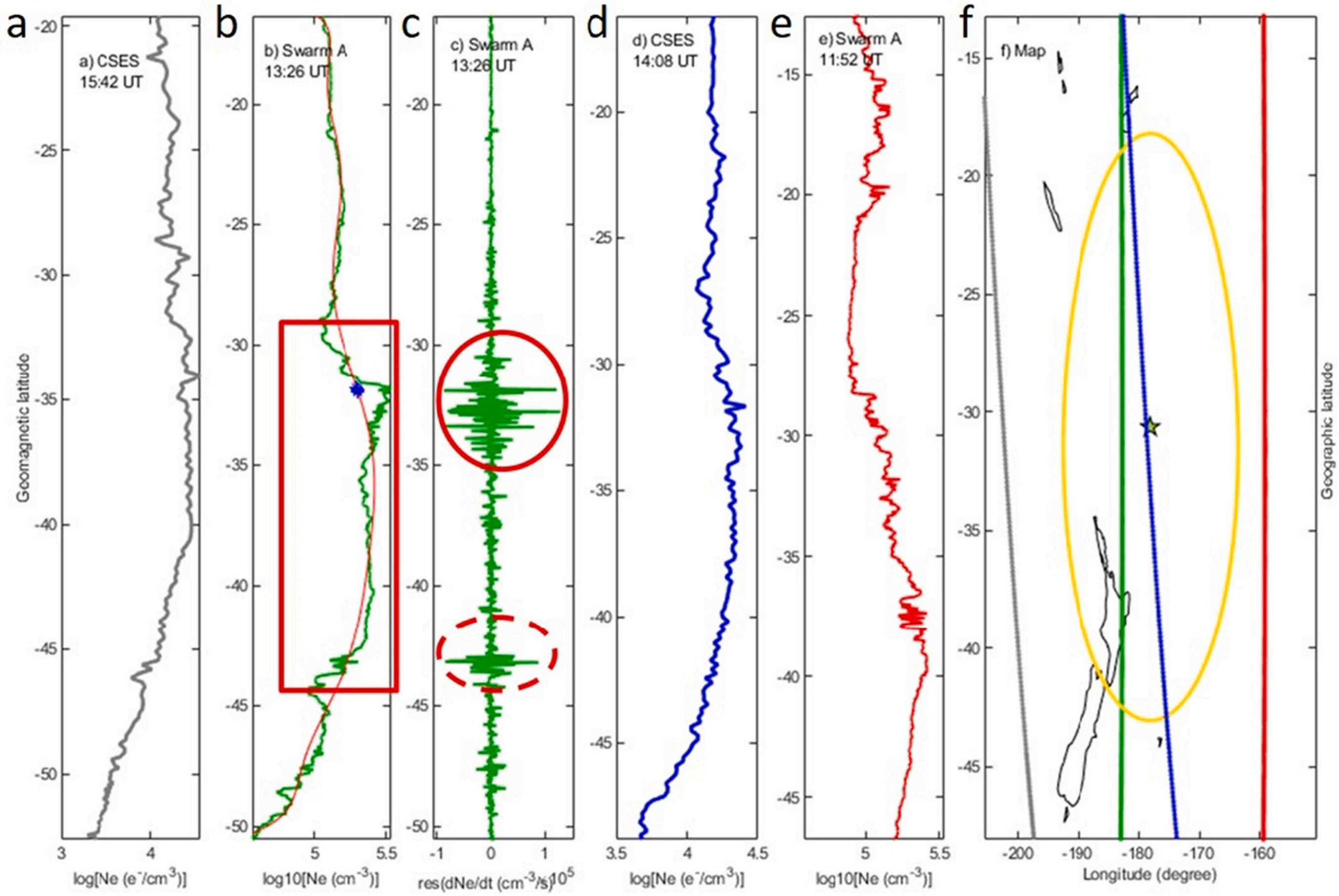

Fig. 11. CSES-01 and Swarm Alpha electron density tracks acquired on 1 June 2019 (~2 weeks before the mainshock). a) CSES-01 acquired at 15:42 UT; b) Swarm Alpha acquired at 13:26 UT; c) residual analysis by NeLog of track shown in b; d) CSES-01 track acquired at 14:08 UT; e) Swarm A acquired at 11:52 UT; f) map with the ground projections of the satellite tracks with the same colour used in the previous panels.

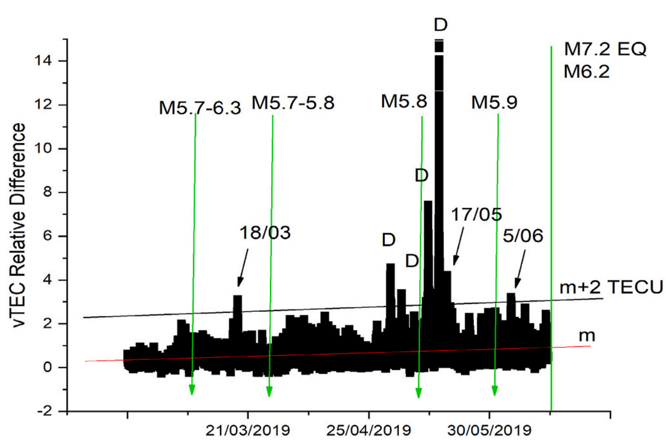

Fig. 12. vTEC two-station differential analysis (method **3**) for the 2019 M7.2 Kermadec Islands EQ. The black arrows indicate three anomalous days, while the vertical green line represents the time of the mainshock occurrence. D stands for disturbed ionosphere. In this figure, m is the mean trend (red line), and m + 2 (black line) is the chosen upper threshold for anomalies identification. The vertical green arrows represent the M5.7+ EQs occurred in the period of investigation (also the range of EQ magnitudes is shown). Please note that, on the same day of the M7.2 mainshock, another EQ occurred with magnitude 6.2.

mean vertical velocity of the order of 50–100 km/day and that produces the Case 2 anomalies in the ionosphere. The Case 1 anomalies in the ionosphere could be generated by a direct electromagnetic coupling between the lithosphere and the ionosphere, e.g. through the p-holes (Freund, 2011).

5. Discussion and conclusions

A full multiparametric and multilayer investigation of the case study of the M7.2 Kermadec Islands (New Zealand) 2019 EQ has been presented here. A chain of processes that start from the lithosphere and propagate through the atmosphere and finally reach the ionosphere is found through Table 1. In particular, we have analysed seismological, atmospheric, satellite and ground electromagnetic data to study the potential LAIC phenomena. The seismological data analysis showed that an acceleration took place during the preparation phase of the earthquake and the R-AMR technique predicted the magnitude of the impending EQ. From atmospheric data, several anomalies before the earthquake have been retrieved: AOD anomaly appears first around 100 days before the EQ, then followed by CH_4, SKT and TCWV around 90–80 days before the EQ. SO_2 anomaly appears around 60 days before the earthquake, almost together with another AOD anomaly. Among all atmospheric quantities, OLR is the last, appearing around 30–40 days before EQ. Finally SKT, TCWV and OLR show other anomalies around 15 days before EQ. Then 6 days before EQ, another AOD anomaly appears. The starting sequence of the anomalies resembles that found for two large Chinese earthquakes, i.e. 2008 M8 Wenchuan EQ and 2013 M7 Lushan EQ (Liu et al., 2020a), where AOD appeared >80 days before

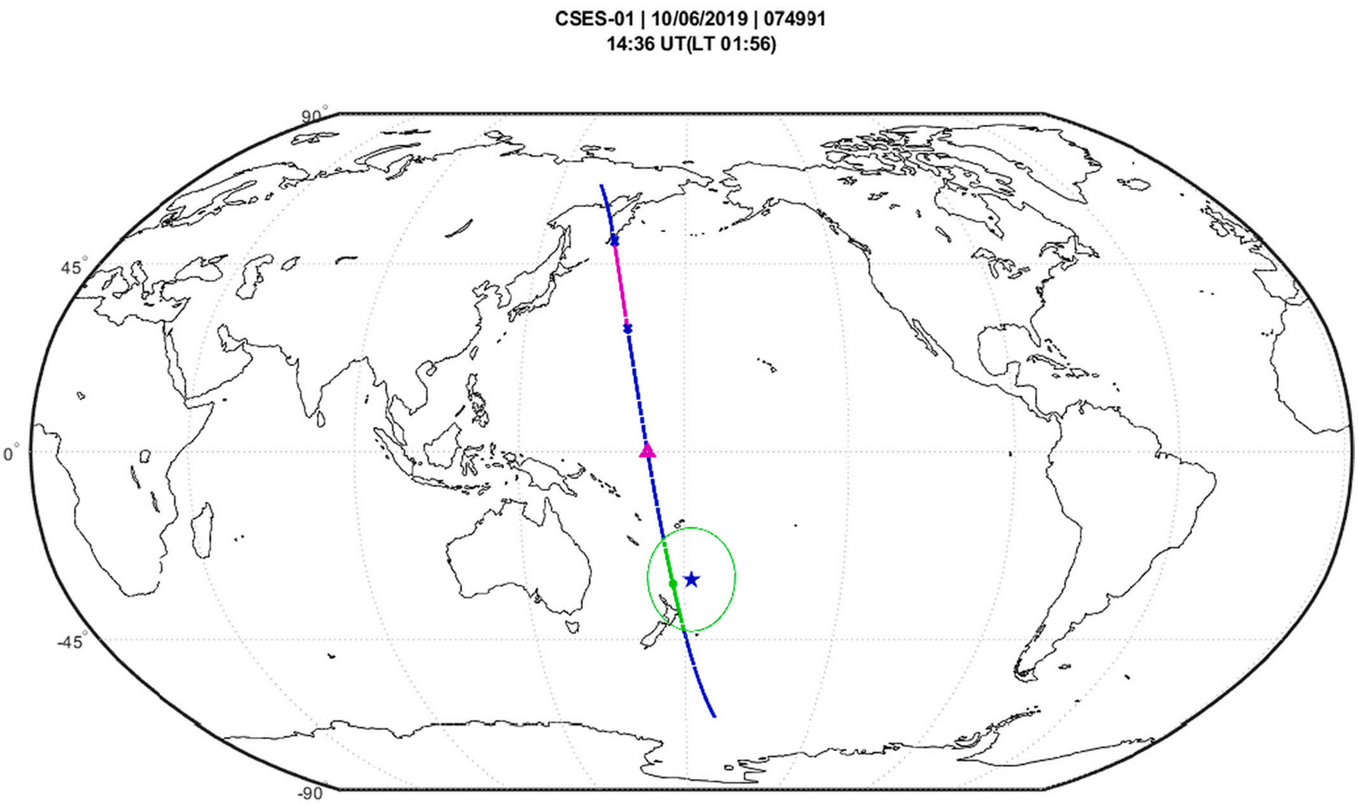

Fig. 13. Map showing the epicentre (blue star) of 2019 Kermadec Islands EQ, the corresponding Dobrovolsky area (green circle) and the track of the orbit number 74991 of CSES-01 (blue line). The green segment of the orbit inside the Dobrovolsky area corresponds to the interval within the solid green vertical lines in the spectrogram (Fig. 14); the magenta section in the upper part is its symmetric (with respect to the magnetic equator) counterpart. The small magenta triangle along the orbit represents the direction of the satellite fly (i.e. it is an ascending orbit). (For interpretation of the references to colour in this figure legend, the reader is referred to the web version of this article.)

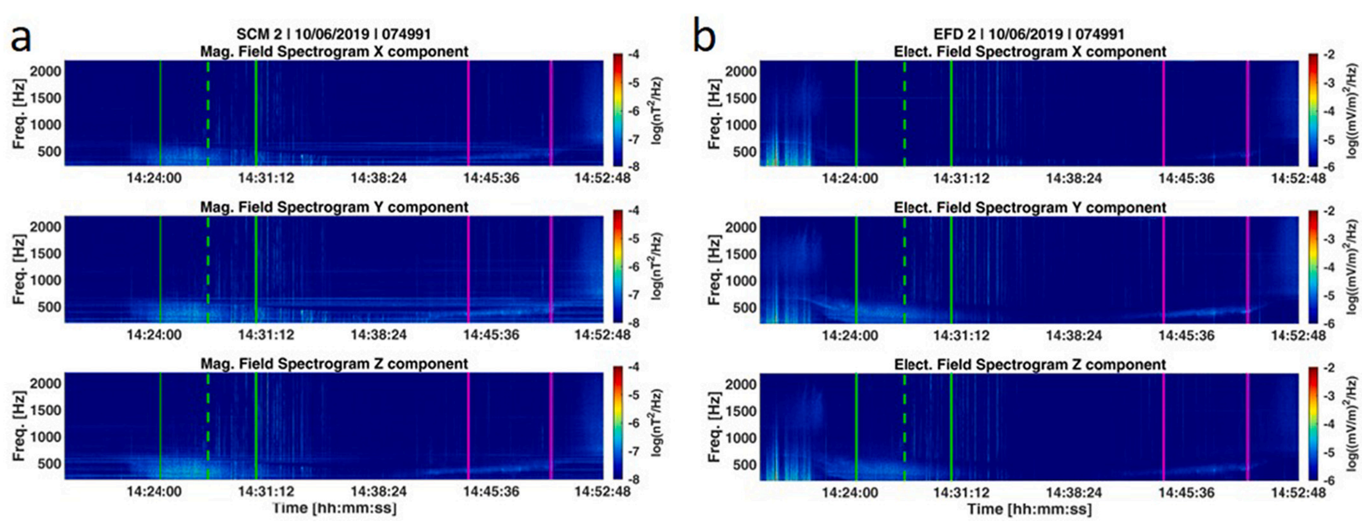

Fig. 14. Spectrograms of magnetic (a) and electric (b) field in the ELF band 5 days before the 2019 Kermadec Islands EQ (orbit number 74991). The solid green vertical lines correspond to the limits of the Dobrovolsky area; the dashed line indicates the time of the minimum distance between the epicentre and the orbit, while the area delimited by the magenta vertical lines represents the symmetric counterpart with respect to the magnetic equator. The intermittent noise of EFD at lower latitudes (well before 14:24:00) is very different from that within the Dobrovolsky region and probably due to some geomagnetic activity at the Auroral region. (For interpretation of the references to colour in this figure legend, the reader is referred to the web version of this article.)

EQ, preceding TCWV and SKT. The increase of aerosols before large earthquakes was already recognized >40 years ago (Tributsch, 1978) and confirmed in many subsequent works (e.g. Liperovsky et al., 2005; Liu et al., 2020a, 2020b). The appearance of a thermal anomaly at 90, 72, 25 and 15 days before the earthquakes of Ridgecrest or Kermadec Islands, shows that temperature is another important atmospheric precursor. Qin et al. (2012) analysed the temperature changes (in terms of air surface temperature and surface latent heat flux, SLHF) on occasion of two important 2010–2011 earthquakes in New Zealand (therefore in a region just a little more southern than the area of the present studied

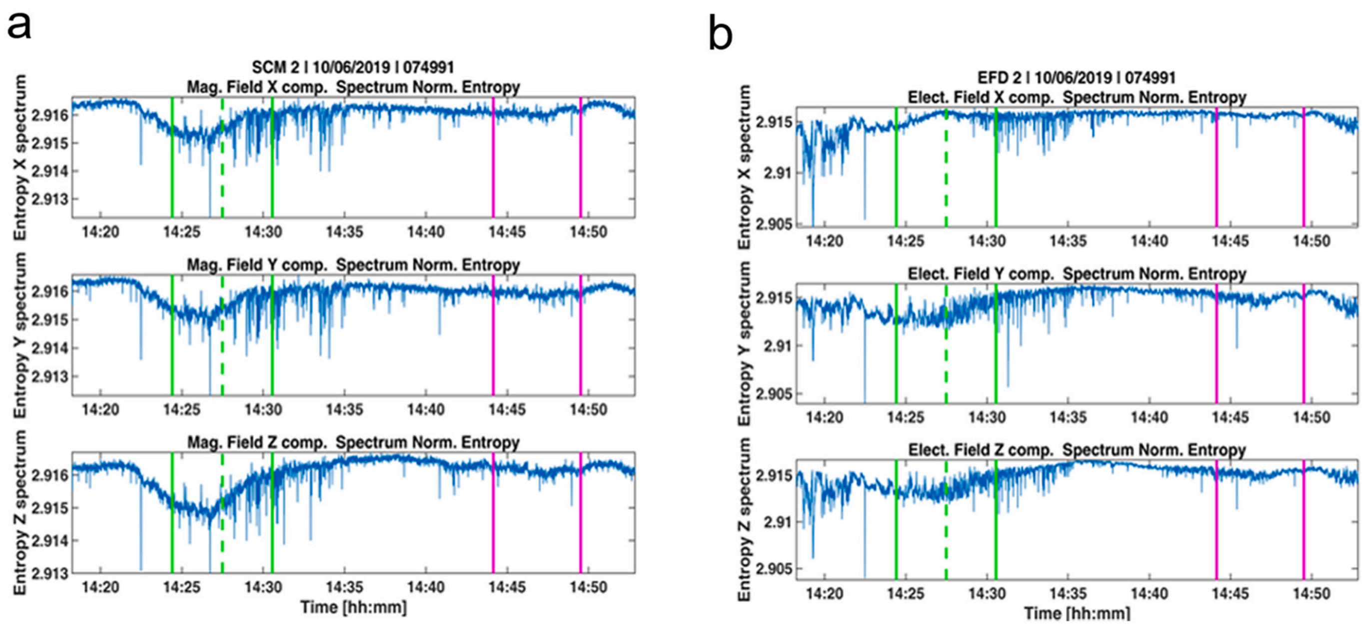

Fig. 15. Normalised entropy of power spectral densities of X,Y,and Z components of magnetic (a) and electric field (b) in the ELF band 5 days before the 2019 Kermadec Islands EQ (orbit number 74991). The solid green vertical lines correspond to the limits of the Dobrovolsky area; the dashed line indicates the time of the minimum distance between the epicentre and the orbit, while the area delimited by the magenta vertical lines represents the symmetric counterpart with respect to the magnetic equator. The large variability at the beginning of the electric field signal corresponds to perturbation at higher latitudes, so it is not related to pre-earthquake phenomena. (For interpretation of the references to colour in this figure legend, the reader is referred to the web version of this article.)

Table 1
Multi-precursor anomalies and their occurrence in terms of the day to the earthquake (Kermadec Islands EQ anomalies in bold black, Ridgecrest EQ anomalies in light black).

	Days to EQ from - to	> 120	120 - 100	99 - 90	89 - 80	79 - 70	69 - 60	59 - 50	49 - 40	39 - 30	29 - 20	19 - 10	9 - 0
	b-value	**290**											
Lithosphere	R-AMR	**180**											
	D			90		75	65,60						
	AOD		**100–103**				**59**						**6**
	AOT						60						
	SKT			**93** 90		75					25	**15**	
Atmosphere	TCWV			**92**	85	**75**						**15**	
	CH_4			**99**		70					**20–22**		
	SO_2						**66**					**12**	
	OLR									**36, 30**		**15**	
	Ionosonde									34			
	IONO1												7
Ionosphere	TEC				**89**						**29**	**10**	
	ELF												**5**
	Y		**110**				65–70						**1**
	Ne		**109–119**										

Bold Black: Kermadec Islands (NZ) M7.2 EQ (this article).
Light Black: Ridgecrest (USA) M7.1 EQ.
D > 0 strength parameter Ridgecrest EQ – incremental part of the stresses (Bondur et al., 2020).
SKT, TCWV, CH_4, AOT, Ionosonde, Swarm Y mag. field (De Santis et al., 2020).
IONO1 - Ionospheric variability – Ridgecrest EQ (Pulinets et al., 2021).

earthquake) and noticed that there were some series of thermal anomalies at about 30 days before the mainshock (3 Sept. 2010 M7.1) and 60 and 3–4 days before the largest aftershock (21 February 2011 M6.3). Qin et al. (2012) also proposed four possible different mechanisms of Lithosphere- (Coversphere)-Atmosphere coupling: magmatic-hydrothermal fluids upwelling, soil moisture increasing, underground pore gases leaking, and positive holes activating and recombining.

Magnetic field and electron density data analyses from Swarm and CSES-01 satellites detected some interesting anomalies. In particular, a magnetic anomaly has been detected on 25 February 2019 during nighttime: comparing the different satellites (Swarm and CSES-01) that crossed the same region at different times, it was possible to follow the temporal evolution of the anomaly. In addition, not shown here, a clear increase of electron density was identified on the night of 26 February 2019, noticing that the maximum Ne value was very close to the future epicentre of the earthquake, and the solar conditions were relatively quiet (see Supplementary Material). Thanks to the orbital sun-synchronous configuration of CSES-01 (precisely at the same nighttime or daytime), it was possible to confirm that Ne was incremented during deep nighttime, by reducing the chances that it could be just a residual of the daily activity. Furthermore, it was possible to confirm the consistency of Ne latitudinal profiles between CSES-01 and Swarm satellite missions. Another satellite payload analysed here was the Electric Field Detector on board CSES-01 satellite. An anomaly within the Dobrovolsky area, more evident in Y and Z components and similar to what was already detected in the spectrograms of the magnetic field from Search Coil Magnetometer was observed. Finally, from ground GNSS data analysis we have considered TEC data and identified three possible precursory anomalies, some of which were detected also using different approaches, from around 90, 30 and 10 days before the earthquake.

Preliminary conclusions show the necessity of integrating multiple datasets to better understand the preparation phase of medium-large earthquakes. Furthermore, the importance of the CSES-01 satellite, in conjunction with the Swarm satellites, has been shown in several contexts, not only useful to better constrain the state of the ionosphere, but also to find several disturbances possibly related to the earthquake occurrence. It has been seen that some of these characteristics have also been detected by the Swarm three-satellite constellation, proving the good integration between both satellite datasets and the potential of the methodology applied.

From the obtained results, summarised by Table 1, two kinds of LAIC can be found: one is practically direct, so its nature should be electromagnetic, as due to the release of p-holes and their propagation up to the ionosphere. The other is more typical of a thermodynamic diffusion process, probably due to a change of temperature and humidity that starts at the ground-atmosphere interface and slowly propagates through the atmosphere up to the ionosphere. A comprehensive way to collect all data anomalies is plotting the cumulative number of all anomalies for Kermadec Islands EQ with time (Fig. 16). A power law as given by eq. (1) fits very well the data pointing to the time of EQ occurrence. This agrees with the analogous power law behaviour of the cumulative number of anomalies for Ridgecrest EQ (De Santis et al., 2020), as approaching to the EQ occurrence. We point out that a power-law behaviour in time is typical of critical systems approaching a critical point where there is a significant change of the system properties (e.g. De Santis et al., 2019c). In this scenario, the EQ is a critical point of the lithosphere, and its imminent occurrence leaves some clues also in the atmosphere and ionosphere, because of their coupling with the lithosphere during the EQ preparation phase.

The results we found in this work were not obtained by chance: the Supplementary Material shows also a confutation analysis, either considering a random simulation or another year (i.e. 2018) without significant seismicity. In the former case, as expected the cumulative number of anomalies does not resemble a power law but a linear trend; in the latter case, when applied to the atmospheric and TEC data analyses, the anomalies are almost absent or just a few, i.e. many less than those found in the year of the earthquake.

The present results confirm those of previous case studies, such as the 2015 Mw7.8 Nepal EQ (De Santis et al., 2017), the 2016 Mw7.8 Ecuador EQ (Akhoondzadeh et al., 2018), the 2017 Mw7.3 Iran-Iraq border EQ (Akhoondzadeh et al., 2019), the 2018 Mw7.5 Indonesia EQ (Marchetti et al., 2019) and the 2019 Mw7.1 Ridgecrest California EQ (De Santis et al., 2020).

In the future perspective, we would like to extend this multi-parametric and multi-layer approach to new case studies, especially occurring during the Swarm and CSES-01 data simultaneous availability. We plan to present full multiparametric and multilayer investigations also of other large earthquakes with comparable magnitude. For instance, we could also extend the analysis to more recent cases, such as M7.1 Japan and the two concomitant events of 21 May 2021 in China (Madou Mw7.3 and Yangbi Mw6.1). Moreover, the intercomparison of all new and old results will allow us to confirm the chain of anomaly occurrences of different parameters and then validate the best LAIC model.

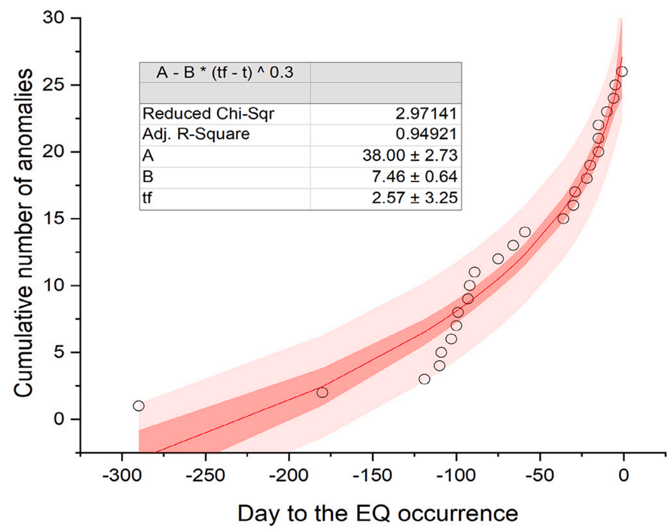

Fig. 16. Cumulative number of the anomalies found for Kermadec Islands EQ vs. time: the best fit (bold red curve) is a power law similar to eq. (1) that points to the EQ occurrence. The red band around the best fit is the 95% confidence interval, while the pink band is the 95% prediction band. (For interpretation of the references to colour in this figure legend, the reader is referred to the web version of this article.)

CRediT authorship contribution statement

A. De Santis: Funding acquisition, Conceptualization, Supervision, Methodology, Writing – original draft, Writing – review & editing. **L. Perrone:** Funding acquisition, Methodology, Writing – review & editing. **M. Calcara:** Investigation, Writing – review & editing. **S.A. Campuzano:** Methodology, Software, Validation, Writing – review & editing. **G. Cianchini:** Methodology, Software, Validation, Writing – review & editing. **S. D'Arcangelo:** Visualization, Investigation, Writing – review & editing. **D. Di Mauro:** Investigation, Writing – review & editing. **D. Marchetti:** Software, Validation, Visualization, Writing – review & editing. **A. Nardi:** Investigation, Writing – review & editing. **M. Orlando:** Software, Validation, Visualization, Writing – review & editing. **A. Piscini:** Software, Validation, Visualization, Writing – review & editing. **D. Sabbagh:** Software, Validation, Visualization, Writing – review & editing. **M. Soldani:** Software, Validation, Visualization, Writing – review & editing.

Declaration of Competing Interest

We, authors of the present paper, declare that there is no conflict of interest.

Data availability

data are available at weblink given in the manuscript

Acknowledgements

This work was undertaken in the framework of Limadou-Science+ funded by ASI (Italian Space Agency). Part of the funds were also given by Working Earth (Pianeta Dinamico) Project. We thank GeoNet (NZ) for providing TEC data (we also thank Claudio Cesaroni and Luca Spogli for giving suggestions on TEC data analyses) and the Kyoto World Data Center for Geomagnetism (http://wdc.kugi.kyoto-u.ac.jp/) for providing geomagnetic data indices. ESA is thanked for providing the Swarm satellite data and the CNSA (Chinese National Space

Administration) for providing CSES-01 satellite data.

Appendix A. Supplementary data

Supplementary data to this article can be found online at https://doi.org/10.1016/j.rse.2022.113325.

References

Akhoondzadeh, M., De Santis, A., Marchetti, D., Piscini, A., Cianchini, G., 2018. Multi precursors analysis associated with the powerful Ecuador (MW = 7.8) earthquake of 16 april 2016 using swarm satellites data in conjunction with other multi-platform satellite and ground data. Adv. Space Res. 61, 1, 248–263. https://doi.org/10.1016/j.asr.2017.07.014.

Akhoondzadeh, M., De Santis, A., Marchetti, D., Piscini, A., Jin, S., 2019. Anomalous seismo-LAI variations potentially associated with the 2017 Mw=7.3 Sarpol-e Zahab (Iran) earthquake from Swarm satellites, GPS-TEC and climatological data. Adv. Space Res. 64, 1, 143–158. https://doi.org/10.1016/j.asr.2019.03.020.

Benioff, H., 1949. Seismic evidence for the fault origin of oceanic deeps. GSA Bull. 60 (12), 1837–1856. https://doi.org/10.1130/0016-7606(1949)60[1837:SEFTFO]2.0.CO;2.

Bertello, I., Piersanti, M., Candidi, M., Diego, P., Ubertini, P., 2018. Electromagnetic field observations by the DEMETER satellite in connection with the 2009 L'Aquila earthquake. Ann. Geophys. 36, 1483–1493. https://doi.org/10.5194/angeo-36-1483-2018.

Bondur, V.G., Gokhberg, M.B., Garagash, I.A., Alekseev, D.A., 2020. Revealing short-term precursors of the strong M > 7 earthquakes in Southern California from the simulated stress-strain state patterns exploiting geomechanical model and seismic catalog data. Front. Earth Sci. 8, 571700 https://doi.org/10.3389/feart.2020.571700.

Bowman, D.D., Ouillon, G., Sammis, C.G., Sornette, A., Sornette, D., 1998. An observational test of the critical earthquake concept. J. Geophys. Res. 103 (B10), 24. https://doi.org/10.1029/98JB00792.

Bufe, C.G., Varnes, D.J., 1993. Predictive modelling of the seismic cycle of the greater San Francisco Bay region. J. Geophys. Res. 98, 9871–9883.

Carbone, V., Piersanti, M., Materassi, M., Battiston, R., Lepreti, F., Ubertini, P., 2021. A mathematical model of lithosphere-atmosphere coupling for seismic events. Sci. Rep. 11, 8682. https://doi.org/10.1038/s41598-021-88125-7.

Cesaroni, C., Spogli, L., Alfonsi, L., De Franceschi, G., Ciraolo, L., Monico, J.F.G., Scotto, C., Romano, V., Aquino, M., Bougard, B., 2015. L-band scintillations and calibrated total electron content gradients over Brazil during the last solar maximum. J. Space Weather Space Clim. 5, A36. https://doi.org/10.1051/swsc/2015038.

Chiodini, G., Cardellini, C., Amato, A., Boschi, E., Caliro, S., Frondini, F., Ventura, G., 2004. Carbon dioxide earth degassing and seismogenesis in central and southern Italy. Geophys. Res. Lett. 31 (L07615), 1–4. https://doi.org/10.1029/2004GL019480.

Chiodini, G., Cardellini, C., Di Luccio, F., Selva, J., Frondini, F., Caliro, S., Rosiello, A., Beddini, G., Ventura, G., 2020. Correlation between tectonic CO2 earth degassing and seismicity is revealed by a 10-year record in the apennines, Italy. Sci. Adv. 6 (35), eabc2938. https://doi.org/10.1126/sciadv.abc2938.

Cianchini, G., De Santis, A., Di Giovambattista, R., et al., 2020. Revised accelerated moment release under test: fourteen worldwide real case studies in 2014–2018 and simulations. Pure Appl. Geophys. 177, 4057–4087. https://doi.org/10.1007/s00024-020-02461-9.

Ciraolo, L., Azpilicueta, F., Brunini, C., Meza, A., Radicella, S.M., 2007. Calibration errors on experimental slant total electron content (TEC) determined with GPS. J. Geod. 81 (2), 111–120.

Cussac, T., Clair, M.-A., Ultré-Guerard, P., Buisson, F., Lassalle-Balier, G., Ledu, M., Elisabelar, C., Passot, X., Rey, N., 2006. The Demeter microsatellite and ground segment, planetary and space science 413–427 (5), 0032–0633. https://doi.org/10.1016/j.pss.2005.10.013.

D'Arcangelo, S., Bonforte, A., De Santis, A., Maugeri, S.R., Perrone, L., Soldani, M., Arena, G., Brogi, F., Calcara, M., Campuzano, S.A., Cianchini, G., Del Corpo, A., Di Mauro, D., Fidani, C., Ippolito, A., Lepidi, S., Marchetti, D., Nardi, A., Orlando, M., Piscini, A., Regi, M., Sabbagh, D., Zhima, Z., Yan, R., 2022. A Multi-Parametric and Multi-Layer Study to Investigate the Largest 2022 Hunga Tonga–Hunga Ha'apai Eruptions. Remote Sensing. 14 (15), 3649. https://doi.org/10.3390/rs14153649.

Dascher-Cousineau, K., Lay, T., Brodsky, E.E., 2020. Two foreshock sequences post gulia and wiemer (2019). Seismol. Res. Lett. 91, 2843–2850.

De Santis, A., Cianchini, G., Di Giovambattista, R., 2015. Accelerating moment release revisited: examples of application to italian seismic sequences. Tectonophysics 639, 82–98. https://doi.org/10.1016/j.tecto.2014.11.015.

De Santis, A., Balasis, G., Pavón-Carrasco, F.J., Cianchini, G., Mandea, M., 2017. Potential earthquake precursory pattern from space: the 2015 Nepal event as seen by magnetic swarm satellites. Earth Planet. Sci. Lett. 461, 119–126.

De Santis, A., Marchetti, D., Spogli, L., Cianchini, G., Pavón-Carrasco, F.J., De Franceschi, G., Di Giovambattista, R., Perrone, L., Qamili, E., Cesaroni, C., et al., 2019a. Magnetic field and electron density data analysis from swarm satellites searching for ionospheric effects by great earthquakes: 12 case studies from 2014 to 2016. Atmosphere 10, 371. https://doi.org/10.3390/atmos10070371.

De Santis, A., Cianchini, G., Qamili, E., Frepoli, A., 2010. The 2009 L'Aquila (Central Italy) seismic sequence as a chaotic process. Tectonophysics 496 (1–4), 44–52. https://doi.org/10.1016/j.tecto.2010.10.005.

De Santis, A., Marchetti, D., Pavón-Carrasco, F.J., Cianchini, G., Perrone, L., Abbattista, C., Alfonsi, L., Amoruso, L., Campuzano, S.A., Carbone, M., Cesaroni, C., De Franceschi, G., De Santis, A., Di Giovambattista, R., Ippolito, A., Piscini, A., Sabbagh, D., Soldani, M., Santoro, F., Spogli, L., Haagmans, R., 2019b. Precursory worldwide signatures of earthquake occurrences on swarm satellite data. Sci. Rep. 9, 20287. https://doi.org/10.1038/s41598-019-56599-1.

De Santis, A., Abbattista, C., Alfonsi, L., Amoruso, L., Campuzano, S.A., Carbone, M., Cesaroni, C., Cianchini, G., De Franceschi, G., De Santis, A., Di Giovambattista, R., Marchetti, D., Martino, L., Perrone, L., Piscini, A., Rainone, M.L., Soldani, M., Spogli, L., Santoro, F., 2019c. Geosystemics view of earthquakes. Entropy 21 (4), 412. https://doi.org/10.3390/e21040412.

De Santis, A., Cianchini, G., Marchetti, D., Piscini, A., Sabbagh, D., Perrone, L., Campuzano, S.A., Inan, S., 2020. A multiparametric approach to study the preparation phase of the 2019 M7.1 Ridgecrest (California, USA) Earthquake. Front. Earth Sci. 8, 478. https://doi.org/10.3389/feart.2020.540398.

De Santis, A., Marchetti, D., Perrone, L., Campuzano, S.A., Cianchini, G., Cesaroni, C., Di Mauro, D., Orlando, M., Piscini, A., Sabbagh, D., Soldani, M., Spogli, L., Zhima, Z., Shen, X., 2021. Statistical correlation analysis of strong earthquakes and ionospheric electron density anomalies as observed by CSES-01. Nuovo Cimento C 2021, 4–5. https://doi.org/10.1393/ncc/i2021-21119-1.

Dobrovolsky, I.P., Zubkov, S.I., Miachkin, V.I., 1979. Estimation of the size of earthquake preparation zones. PAGeoph. 117, 1025. https://doi.org/10.1007/BF00876083.

Felzer, K.R., Abercrombie, R.E., Ekström, G., 2004. A common origin for aftershocks, foreshocks, and multiplets. Bull. Seismol. Soc. Am. 94 (1), 88–98.

Finlay, C.C., Kloss, C., Olsen, N., et al., 2020. The CHAOS-7 geomagnetic field model and observed changes in the South Atlantic anomaly. Earth Planets Space 72, 156. https://doi.org/10.1186/s40623-020-01252-9.

Freund, F., 2011. Pre-earthquake signals: underlying physical processes. J. Asian Earth Sci. 383–400.

Gelaro, R., McCarty, W., Suárez, M.J., Todling, R., Molod, A., Takacs, L., Randles, C.A., Darmenov, A., Bosilovich, M.G., Reichle, R., Wargan, K., Coy, L., Cullather, R., Draper, C., Akella, S., Buchard, V., Conaty, A., da Silva, A.M., Gu, W., Kim, G.-K., Koster, R., Lucchesi, R., Merkova, D., Nielsen, J.E., Partyka, G., Pawson, S., Putman, W., Rienecker, M., Schubert, S.D.C., Sienkiewicz, M., Zhao, B., 2017. The Modern-Era Retrospective Analysis for Research and Applications, Version 2 (MERRA-2). Journal of Climate 30 (14), 5419–5454. https://doi.org/10.1175/JCLI-D-16-0758.1.

Gulia, L., Wiemer, S., 2019. Real-time discrimination of earthquake foreshocks and aftershocks. Nature 574, 193–199. https://doi.org/10.1038/s41586-019-1606-4.

Hayakawa, M., Molchanov, O.A., 2002. Seismo Electromagnetics Lithosphere-Atmosphere-Ionosphere Coupling (ed. TERRAPUB) 477 pages, Tokyo.

Herrmann, M., Piegari, E., Marzocchi, W., 2022. Revealing the spatiotemporal complexity of the magnitude distribution and b-value during an earthquake sequence. Nat. Commun. 13, 5087. https://doi.org/10.1038/s41467-022-32755-6.

Liperovsky, V.A., Meister, C.-V., Liperovskaya, E.V., Davidov, V.F., Bogdanov, V.V., 2005. On the possible influence of radon and aerosol injection on the atmosphere and ionosphere before earthquakes. Natural Hazards and Earth System Sciences 5 (6), 783–789. https://doi.org/10.5194/nhess-5-783-2005.

Liu, Q., De Santis, A., Piscini, A., Cianchini, G., Ventura, G., Shen, X., 2020a. Multi-parametric climatological analysis reveals the involvement of fluids in the preparation phase of the 2008 ms 8.0 wenchuan and 2013 ms 7.0 lushan earthquakes. Remote Sens. 12, 1663. https://doi.org/10.3390/rs12101663.

Liu, Q., Shen, X., Zhang, J., Cui, J., Tan, Q., Zhao, S., Li, M., 2020b. Aerosol anomalies associated with occurrence of recent strong earthquakes (> M 8.0). Terr. Atmos. Ocean. Sci. 31, 677–689. https://doi.org/10.3319/TAO.2020.05.22.01.

Marchetti, D., De Santis, A., Shen, X., Campuzano, S.A., Perrone, L., Piscini, A., Di Giovambattista, R., Jin, S., Ippolito, A., Cianchini, G., Cesaroni, C., Sabbagh, D., Spogli, L., Zhima, Z., Huang, J., 2019. Possible lithosphere-atmosphere-ionosphere coupling effects prior to the 2018 Mw=7.5 Indonesia earthquake from seismic, atmospheric and ionospheric data. J. Asian Earth Sci. https://doi.org/10.1016/j.jseaes.2019.104097.

Marchetti, D., De Santis, A., Campuzano, S.A., Soldani, M., Piscini, A., Sabbagh, D., Cianchini, G., Perrone, L., Orlando, M., 2020. Swarm Satellite Magnetic Field Data Analysis Prior to 2019 Mw = 7.1 Ridgecrest (California, USA) Earthquake 12, 502. https://doi.org/10.3390/geosciences10120502.

McGuire, J.J., Boettcher, M.S., Jordan, T.H., 2005. Foreshock sequences and short-term earthquake predictability on East Pacific rise transform faults. Nature 434, 457–461. https://doi.org/10.1038/nature03377.

Mignan, A., 2011. Retrospective on the Accelerating Seismic Release (ASR) hypothesis: Controversy and new horizons. Tectonophysics 505 (1–4), 1–16. https://doi.org/10.1016/j.tecto.2011.03.010.

Mogi, K., 1963. Some discussions on aftershocks, foreshocks and earthquake swarms – the fracture of a semi-infinite body caused by inner stress origin and its relation to the earthquake phenomena (3). Bull. Earthquake Res. Inst. Univ. Tokyo 41, 615–658.

Mueller, S.C., 2019. Earthquake Catalogs for the USGS National Seismic Hazard Maps. Seismological Research Letters 90 (1), 251–261. https://doi.org/10.1785/0220170108.

Nanjo, K.Z., Yoshida, A., 2021. Changes in the b value in and around the focal areas of the M6.9 and M6.8 earthquakes off the coast of Miyagi prefecture, Japan, in 2021. Earth Planets Space 73, 176. https://doi.org/10.1186/s40623-021-01511-3.

Okal, E.A., 2019. Energy and magnitude: a historical perspective. Pure Appl. Geophys. 176, 3815–3849. https://doi.org/10.1007/s00024-018-1994-7.

Parrot, M., 2002. The micro-satellite DEMETER. J. Geodynam. 33 (4–5), 535–541. https://doi.org/10.1016/S0264-3707(02)00014-5.

Parrot, M., 2012. Statistical analysis of automatically detected ion density variations recorded by DEMETER and their relation to seismic activity. Ann. Geophys. 55 (1). https://www.annalsofgeophysics.eu/index.php/annals/article/view/5270.

Picozza, P., Conti, L., Sotgiu, A., 2021. Looking for earthquake precursors from space: a critical review. Front. Earth Sci. 14 https://doi.org/10.3389/feart.2021.676775.

Piersanti, M., Materassi, M., Battiston, R., Carbone, V., Cicone, A., D'Angelo, G., Diego, P., Ubertini, P., 2020. Magnetospheric–Ionospheric–Lithospheric coupling model. 1: observations during the 5 august 2018 bayan earthquake. Magnetospheric-ionospheric-lithospheric coupling model 1. Remote Sens. 12 (20), 3299. https://doi.org/10.3390/rs12203299.

Pinheiro, K.J., Jackson, A., Finlay, C.C., 2011. Measurements and uncertainties of the occurrence time of the 1969, 1978, 1991, and 1999 geomagnetic jerks. Geochem. Geophys. Geosyst. 12, Q10015.

Piscini, A., De Santis, A., Marchetti, D., Cianchini, G., 2017. A multi-parametric climatological approach to study the 2016 amatrice-norcia (Central Italy) earthquake preparatory phase. Pure Appl. Geophys. 174 (10), 3673–3688.

Piscini, A., Marchetti, D., De Santis, A., 2019. Multi-parametric climatological analysis associated with global significant volcanic eruptions during 2002–2017. Pure and Appl. Geoph. 176 (8), 3629–3647. (https://link.springer.com/article/10.1007%2Fs00024-019-02147-x).

Pulinets, S., Ouzounov, D., 2011. Lithosphere–atmosphere–ionosphere coupling (LAIC) model-an unified concept for earthquake precursors validation. J. Asian Earth Sci. 41 (4–5), 371–382. https://doi.org/10.1016/j.jseaes.2010.03.005.

Pulinets, S., Tsidilina, M., Ouzounov, D., Davidenko, D., 2021. From Hector mine M7.1 to ridgecrest M7.1 earthquake. A look from a 20-year perspective. Atmosphere 12, 262. https://doi.org/10.3390/atmos12020262.

Qin, K., Wu, L.X., De Santis, A., Meng, J., Ma, W.Y., Cianchini, G., 2012. Quasi-synchronous multi-parameter anomalies associated with the 2010–2011 New Zealand earthquake sequence. Nat. Hazards Earth Syst. Sci. 12, 1059–1072. https://doi.org/10.5194/nhess-12-1059-2012.

Scholz, C.H., 2015. On the stress dependence of the earthquake b value. Geophys. Res. Lett. 42 (5), 1399–1402. https://doi.org/10.1002/2014GL062863.

Shannon, C.E., 1948. A mathematical theory of communication. Bell Syst. Tech. J. 27, 379–423.

Shen, X., Zhang, X., Yuan, S., et al., 2018. The state-of-the-art of the China seismo-electromagnetic satellite mission. Sci. China Technol. Sci. 61, 634–642. https://doi.org/10.1007/s11431-018-9242-0.

Smith, E.M.I., Price, R.C., 2006. The Tonga-kermadec arc and Havre-lau back-arc system: their role in the development of tectonic and magmatic models for the western Pacific, J. Volcanol. Geothermal Res. 156. 3–4, 315–331. https://doi.org/10.1016/j.jvolgeores.2006.03.006.

Sorokin, V.M., Yashchenko, A.K., Surkov, V.V., 2019. Generation of geomagnetic disturbances in the ionosphere by a tsunami wave. Geomagn. Aeron. 59, 221–233. https://doi.org/10.1134/S0016793219020130.

Tributsch, H., 1978. Do aerosol anomalies precede earthquakes? Nature 276, 606–608. https://doi.org/10.1038/276606a0.

Wang, Q., Huang, J.P., Zhang, X.M., Shen, X.H., Yuan, S.G., Zeng, L., Cao, J.B., 2018. China seismo-electromagnetic satellite search coil magnetometer data and initial results. Earth and Planetary Physics 2 (6), 462–468. https://doi.org/10.26464/epp2018044.

Wiemer, S., 2000. Minimum magnitude of completeness in earthquake catalogs: examples from Alaska, the Western United States, and Japan. Bull. Seismol. Soc. Am. 90 (4), 859–869. https://doi.org/10.1785/0119990114.

Zhima, Z., Huang, J., Shen, X., Chen, L., Piersanti, M., Yang, Y., Wang, Q., Zeng, L., Lei, J., Chu, W., Zhao, S., Hu, Y., Guo, F., 2020. Simultaneous observations of ELF/VLF rising-tone quasiperiodic waves and energetic electron precipitations in the high-latitude upper ionosphere. J. Geophys. Res. Space. Physics Volume 125, Issue 5. https://doi.org/10.1029/2019JA027574.

Zhu, F., Jiang, Y., 2020. Investigation of GIM-TEC disturbances before $M \geq 6.0$ inland earthquakes during 2003–2017. Sci. Rep. 10, 18038. https://doi.org/10.1038/s41598-020-74995-w.